Structured Beams as Quantum Probes

by

Dusan Sarenac

A thesis
presented to the University of Waterloo
in fulfillment of the
thesis requirement for the degree of
Doctor of Philosophy
in
Physics (Quantum Information)

Waterloo, Ontario, Canada, 2018

Examining Committee Membership

The following served on the Examining Committee for this thesis. The decision of the Examining Committee is by majority vote.

External Examiner:	Dr. Geoffrey Greene Professor, University of Tennessee
Supervisor:	Dr. David Cory Professor, University of Waterloo
Internal Member:	Dr. Jan Kycia Professor, University of Waterloo
Internal-External Member:	Dr. Jonathan Baugh Associate Professor, University of Waterloo
Other Member(s):	Dr. Stefan Kycia Associate Professor, University of Guelph

Author's Declaration

I hereby declare that I am the sole author of this thesis. This is a true copy of the thesis, including any required final revisions, as accepted by my examiners.

I understand that my thesis may be made electronically available to the public.

Dusan Sarenac

Abstract

This thesis describes several projects under the common theme of generating and manipulating the spatial quantum phase structure of matter and electromagnetic waves. Experiments dealing with the following topics are addressed: perfect crystal neutron interferometry, far-field phase-grating moiré interferometry, orbital angular momentum (OAM), spin-orbit states, and lattices of spin-orbit states.

The first focus of the thesis is describing the work related to the construction of a new beamline dedicated to quantum information related neutron interferometry experiments at the National Institute of Standards and Technology's Center for Neutron Research. This includes the development of the necessary environmental isolation, phase stability, and temperature isolation mechanisms; and the installation and optimization of spin polarization elements. The new beamline is now operational and it is currently one of only three neutron interferometry facilities in the world.

The second focus of the thesis is to describe the development and characterization of far-field phase-grating moiré neutron interferometry. This technique enables studies that are complimentary to those of perfect crystal neutron interferometry experiments. It may be used to probe structured materials and characterize neutron interactions with potential gradients. A two phase-grating moiré neutron interferometer was developed, characterized, and optimized. This setup was then employed to probe the microstructure of a monodisperse suspension of $\sim$2 μm diameter polystyrene spheres. Furthermore, a three phase-grating moiré neutron interferometer was developed and characterized. This unique setup promises a wide range of impactful experiments from far-field imaging of material substructure to fundamental physics.

The third focus of the thesis is to describe neutron OAM. These experiments revolve around the preparation and characterization of an azimuthally varying phase profile. The demonstration of neutron OAM using a perfect crystal neutron interferometer is described, where a spiral phase plate was used to induce OAM in one of the paths of the interferometer. Furthermore, a modified setup was used to perform neutron holography of a macroscopic object which induces an azimuthally varying phase profile. These methods provide a new tool for interferometric testing of neutron optics and the characterization of coherence of neutron beams.

The last focus of the thesis is to describe matter wave and optical spin correlated OAM (spin-orbit) states. Methods to prepare neutron spin-orbit states via special geometries of magnetic fields are proposed. The preparation, entanglement characterization, and proposed experimental verification of such states are described in detail. Furthermore, a method which is capable of preparing lattices of optical and neutron spin-orbit states is introduced and described. This method utilizes novel optical and neutron devices and it is based on coherent averaging and spatial control methods borrowed from nuclear magnetic resonance. The experimental preparation and characterization of optical lattices of spin-orbit states is described in detail.

Acknowledgements

First and foremost, I would like to thank my supervisor professor David Cory for providing me with an in-depth knowledge of physics, his perseverance in demanding that I do things properly without taking shortcuts, and for steering my career path in a positive direction. I would also like to thank professor Dmitry Pushin with whom I worked closely throughout my graduate studies. I was fortunate to have him as a close friend, and his numerous lessons on experimental physics are very much appreciated. Furthermore, I would like to thank my University of Waterloo colleagues Joachim Nsofini, Ian Hincks, Kamyar Ghofrani, Paulo Miguel and Connor Kapahi with whom I have worked on several neutron related projects, Ivar Taminiau and Alex Mitrovic for their work on our machine shop related tasks, and Carly Turnbull for her help with administrative related tasks. I would also like to thank my colleagues at the National Institute of Standards and Technology (NIST) Benjamin Heacock, Chandra Shahi, Taisiya Mineeva, Charles Clark, Daniel Hussey, and Wangchun Chen with whom I worked with during my stay at NIST, and Martha Neviaser for administrative related tasks. A very special thanks goes to my NIST colleagues Michael Huber and Muhammad Arif who have put in a considerable effort in ensuring that my stay at NIST was beneficial and making me feel like family. I would also like to thank our National Institute of Health colleague Wen Han who has guided us through the phase-grating moiré interferometry experiments. I am thankful to my brother Nedjo Sarenac for his vast support during my studies. Lastly, I would like to thank my mom, Mirjana Sarenac, for constantly assessing my every graduate move and pushing me to succeed.

Dedicated to my mom, Mirjana Sarenac

Table of Contents

List of Figures ix

1 Introduction and Formalism 1
- 1.1 Thesis Outline and Main Results . . . 1
- 1.2 Electromagnetic Waves and Matter Waves . . . 2
- 1.3 Quantum Phase . . . 5
  - 1.3.1 Optical Potential and the Quantum Phase . . . 5
  - 1.3.2 Quantum Spin and Magnetic Potentials . . . 9
- 1.4 Neutron Interferometry . . . 11
  - 1.4.1 Neutrons . . . 11
  - 1.4.2 Perfect Crystal Neutron Interferometer . . . 12
  - 1.4.3 Neutron Interferometry Beamlines at the NCNR . . . 16
  - 1.4.4 Neutron Interferometry in Vacuum . . . 18
- 1.5 Two-level Quantum Systems and Coherent Superpositions . . . 21

2 Phase-Grating Moiré Interferometry 24
- 2.1 Introduction and Historical Background . . . 24
- 2.2 Characterization and Optimization of Neutron Phase-Gratings . . . 26
  - 2.2.1 Theory . . . 27
  - 2.2.2 Experimental Methods . . . 30
  - 2.2.3 Rotational Effects on the Resulting Momentum Distribution . . . 31
- 2.3 Two Phase-Grating Moiré Interferometer . . . 36
  - 2.3.1 Theory . . . 36
  - 2.3.2 Experimental Methods . . . 40
  - 2.3.3 Results and Discussion . . . 42
- 2.4 Measuring the Microstructure of Samples with the Far-Field Interferometer . . . 45
  - 2.4.1 Experimental Methods . . . 47
  - 2.4.2 Results and Discussion . . . 49
- 2.5 Three Phase-Grating Moiré Interferometer . . . 51
  - 2.5.1 Potential Applications . . . 56
- 2.6 Conclusion . . . 57

3 Neutron Orbital Angular Momentum and Applications to Holography 59
- 3.1 Overview of $e^{i\ell\phi}$ . . . 59
- 3.2 Basis States of Orbital Angular Momentum . . . 60

3.3 Intrinsic and Extrinsic Orbital Angular Momentum . . . 62
3.4 Demonstration of Neutron Orbital Angular Momentum . . . 64
3.5 Holography with a Neutron Interferometer . . . 65
3.5.1 Introduction . . . 65
3.5.2 Schematic of Neutron Holography . . . 67
3.5.3 Experimental Method . . . 68
3.5.4 Results . . . 69

4 Preparation of Spin-Coupled Orbital Angular Momentum States 71
4.1 Introduction . . . 71
4.2 Spin Polarization Geometries of Spin-Orbit States . . . 72
4.3 Methods to Prepare Neutron Spin-Orbit States . . . 75
4.3.1 Magnetic Spiral Phase Plate . . . 75
4.3.2 Quadrupole Magnetic Field . . . 75
4.3.3 Spin-Orbit States with Higher Order OAM Values . . . 77
4.3.4 BB1 Sequence . . . 78
4.3.5 Lattices of Spin-Orbit States . . . 80
4.4 Characterization of Neutron Spin-Orbit States . . . 82
4.4.1 Entanglement in the Spin-Orbit States . . . 82
4.4.2 Spin-Orbit Ramsey Experiment . . . 83
4.4.3 Intensity Correlations . . . 85
4.4.4 Momentum Correlations . . . 86
4.5 Lattices of Optical Spin-Orbit states . . . 90
4.5.1 Optical OAM . . . 90
4.5.2 Preparation of Optical LOV Beams . . . 91
4.5.3 Experimental Methods . . . 94
4.5.4 Characterization of Optical LOV Beams . . . 94
4.5.5 Characterizing Materials with Optical LOV Beams . . . 95
4.5.6 Conclusion . . . 97

5 Conclusion and Future Prospects 98
5.1 Future Work . . . 99

Bibliography 100

List of Figures

1.1 Snell's law of refraction for neutrons . . . 5
1.2 Bloch sphere representation of the neutron spin state . . . 10
1.3 NCNR research reactor . . . 12
1.4 Neutron interferometers . . . 15
1.5 Neutron interferometry beamline NIOF . . . 16
1.6 Neutron interferometry beamline NIOFa . . . 17
1.7 Vacuum enclosure for temperature isolation at NIOFa . . . 19
1.8 Temperature and contrast data for the NI in a vacuum . . . 20
1.9 Isomorphism between the two-level quantum systems . . . 22

2.1 Near-field vs far-field . . . 26
2.2 Phase-grating induced momentum distributions . . . 27
2.3 Setup for phase-grating characterization . . . 28
2.4 Momentum distributions as a function of grating rotation about the y-axis . . . 29
2.5 Diffraction peak areas . . . 30
2.6 Grating-2 measured momentum distribution . . . 31
2.7 Diffraction peaks as grating-2 is rotated about the z-axis . . . 33
2.8 Double grating momentum distribution . . . 34
2.9 Double grating momentum distribution with grating rotation . . . 35
2.10 Far-field phase-grating moiré NI . . . 36
2.11 Schematic of the two phase-grating interferometer setup . . . 37
2.12 Contrast optimization . . . 39
2.13 Measured far-field intensity of the two PGMI . . . 40
2.14 Contrast and frequency of the two PGMI . . . 41
2.15 Phase stepping with the two PGMI . . . 42
2.16 Contrast vs wavelength of the two PGMI . . . 43
2.17 Phase-contrast imaging with the two PGMI . . . 44
2.18 Two PGMI contrast at polychromatic beamline . . . 47
2.19 Scattering data obtained via the two PGMI . . . 48
2.20 Polystyrene sphere solution . . . 50
2.21 Three PGMI setup . . . 52
2.22 Contrast optimization of the three PGMI . . . 53
2.23 Contrast vs three PGMI length . . . 54
2.24 Phase stepping with the three PGMI . . . 55
2.25 Sample imaging with the three PGMI . . . 56

3.1 State probabilities after an SPP . . . 62
3.2 Intrinsic vs extrinsic OAM . . . 63
3.3 Phase-imaging of an OAM beam . . . 64
3.4 Neutron holography . . . 66
3.5 Intensity profiles obtained with OAM beams and holography . . . 68
3.6 Measured and simulated interferograms . . . 69
3.7 Computed far-field intensity of the neutron OAM beam . . . 70

4.1 Spin orientations of spin-orbit beams . . . 73
4.2 Methods of producing neutron spin-orbit states . . . 74
4.3 Quadrupole spin-orbit state . . . 76
4.4 Coefficients of spin-orbit states . . . 78
4.5 Overlap of spin-orbit states . . . 79
4.6 Generating lattice of spin-orbit states with magnetic gradients . . . 80
4.7 Concurrence of the quadrupole spin-orbit state . . . 82
4.8 Normalized concurrence of the quadrupole spin-orbit state . . . 83
4.9 Setup for the spin-orbit Ramsey fringe experiment . . . 84
4.10 Spin dependent intensity and momentum distributions . . . 85
4.11 Spin dependent momentum distributions of the quadrupole spin-orbit state . . . 86
4.12 Spin dependent momentum distributions of the LOV beams . . . 87
4.13 Proposed experiment to map out the 2D momentum distribution of a neutron spin-orbit state . . . 88
4.14 Optical Michelson interferometer . . . 89
4.15 Far-field intensity and phase profile of $\ell = 420$ optical OAM beam . . . 90
4.16 Generating optical LOV beams . . . 91
4.17 Polarization dependent intensity of the optical LOV beam . . . 92
4.18 Measured intensities of optical LOV beams . . . 93
4.19 Optical phase imaging of the LOV beams . . . 94
4.20 Polarization dependent intensities of optical LOV beams . . . 95
4.21 Mapping of the 2D linear and circular birefringence with optical LOV beams 96

Chapter 1

Introduction and Formalism

1.1 Thesis Outline and Main Results

The focus of this thesis is the description of several projects under the common theme of generating and manipulating the spatial quantum phase structure of matter waves and electromagnetic waves. The thesis builds upon the work of previous students and colleagues. Most closely related are: Dmitry Pushin's thesis describing the work on a decoherence free subspace perfect crystal neutron interferometer (NI) [1]; Joachim Nsofini's thesis describing the work on a quantum information model of dynamical diffraction [2]; and Chandra Shahi's thesis describing the construction of the new neutron interferometry beamline at National Institute of Standards and Technology's (NIST) Center for Neutron Research (NCNR) [3]. In this thesis, experiments dealing with the following topics are addressed: perfect crystal neutron interferometry, far-field phase-grating moiré interferometry, orbital angular momentum (OAM), spin-orbit states, and lattices of spin-orbit states. The chapters are structured as follows:

- Chapter 1 contains the theoretical framework needed for this thesis. In addition, it describes the neutron interferometry beamlines at the NCNR [4, 5], and the development and characterization of a vacuum chamber which was employed for NI temperature isolation [6]. A brief reference is made to modeling the neutron propagation through a perfect crystal [7], a proposal for a new five blade NI geometry [8], the effects of annealing on neutron interferometry [9], and an experimental test of the chameleon theory of dark energy [10].

- Chapter 2 describes the development and characterization of far-field phase-grating moiré neutron interferometry. This includes the characterization of neutron diffraction from phase-gratings using Bragg diffraction crystals [11], demonstration of a two phase-grating moiré neutron interferometer [12] and its application to measuring the microstructure of samples [13], and the demonstration of a three phase-grating moiré neutron interferometer for large interferometer area applications [14].

- Chapter 3 reviews the fundamentals of OAM and the demonstration of neutron OAM [15]. The chapter then focus on the experiment demonstrating neutron holography of a macroscopic object which induces OAM [16].

- Chapter 4 presents and describes the methods for preparing and characterizing neutron spin-orbit states [17], and the extensions to lattices of neutron spin-orbit states [18]. The preparation, entanglement characterization, and proposed experimental verifications of such states are described in detail. Lastly, the chapter introduces and describes the analogous methods to prepare and characterize optical lattices of spin-orbit states [19].

1.2 Electromagnetic Waves and Matter Waves

Max Planck proposed in 1900 that energy is quantized and introduced what is now known as the "Planck's constant" with a value of $h = 6.62607 \times 10^{-34}$ J·s [20, 21]. In 1905 Albert Einstein proposed that light is also propagated and absorbed in quanta, which are now called "photons" [22]. The energy, E, and momentum, p, of a photon are given by:

$$E = hf = \frac{hc}{\lambda} = \hbar kc, \qquad p = \frac{E}{c} = \frac{h}{\lambda} = \hbar k \tag{1.1}$$

where $\hbar = h/2\pi$ is the reduced Planck's constant, and $f,\ \lambda,\ k = 2\pi/\lambda$, and $c \approx 3 \times 10^8$ m/s are the frequency, wavelength, wavevector, and speed of light respectively. Note that for the momentum relation the mass-energy equivalence formula $E = mc^2$ was used.

Electromagnetic waves are described by a wave function, $\Psi(r,t)$, which is governed by the wave equation:

$$\nabla^2\Psi(r,t) = \frac{1}{c^2}\frac{\partial^2\Psi(r,t)}{\partial t^2} \tag{1.2}$$

where ∇^2 is the Laplacian, r is an arbitrary direction in (x,y,z), and t is time. In 1924 Louis de Broglie proposed that the wave-particle duality captured by $p = h/\lambda$ was applicable to particles as well [23]. It follows then that the energy and the momentum of a particle, or a matter wave, are given by:

$$E = \frac{p^2}{2m} = \frac{h^2}{2m\lambda^2} = \frac{\hbar^2k^2}{2m}, \qquad p = mv = \frac{h}{\lambda} = \hbar k \tag{1.3}$$

where $m,\ v,\ \lambda$, and k are the mass, velocity, de Broglie wavelength, and wavevector of the particle respectively.

In 1926 Erwin Schrodinger determined a wave equation for matter waves [24], now known as the Schrodinger Equation (SE):

$$\left(-\frac{\hbar^2}{2m}\nabla^2 + V(r,t)\right)\Psi(r,t) = H\Psi(r,t) = i\hbar\frac{\partial\Psi(r,t)}{\partial t} \tag{1.4}$$

where H is the Hamiltonian, $V(r,t)$ is the external potential, and $\Psi(r,t)$ is the wave function

which contains a complete description of what can be learned about a quantum system. The probability of finding a particle at a location r_0 at time t_0 is given by the Born rule [25]:

$$I(r_0, t_0) = \Psi^*(r_0, t_0)\Psi(r_0, t_0) = |\Psi(r_0, t_0)|^2 \tag{1.5}$$

where $\Psi^*(r_0, t_0)$ is the complex conjugate of $\Psi(r_0, t_0)$. The normalization constraint is that:

$$\int_{-\infty}^{\infty} |\Psi(r, t)|^2 dr = 1. \tag{1.6}$$

Conservation of momentum results from the fact that if $\Psi(r, t)$ satisfies the SE, then so does $\Psi(r + r_0, t)$ for any constant r_0. Superposition comes naturally from the fact that $\Psi_3(r, t) = \alpha\Psi_1(r, t) + \beta\Psi_2(r, t)$ satisfies the SE for any scalars α, β provided that $\Psi_1(r, t)$ and $\Psi_2(r, t)$ are already solutions. Superposition is a central feature of waves in general which states that waves pass through each other and continue unaffected, while at points of overlap the net result is the sum of the individual amplitudes.

Diffraction, reflection, refraction, and interference are a consequence of the stationary equations, and therefore the complete set of wave phenomena of light occur for matter wave as well because the time-independent forms of Eq. 1.2 and Eq. 1.4 have the same mathematical structure.

In free space where $V(r, t) = 0$, a possible solution to the SE is in the form of plane waves:

$$\Psi(r, t) = e^{i(\vec{k}\cdot\vec{r} - \omega t)} \tag{1.7}$$

where $\omega = E/\hbar$. Plane waves are a good basis, but physical solutions are often described by wave packets, which are a normalizable distribution of plane waves. From Eq. 1.7 it follows that the wavevector and the angular frequency of a plane wave can be obtained as follows:

$$\vec{k} = \vec{\nabla}\phi \qquad \omega = -\frac{\partial\phi}{\partial t} \tag{1.8}$$

where $\phi = \vec{k} \cdot \vec{r} - \omega t$ denotes the phase of the plane wave.

From here the focus will solely be on neutrons as far as matter waves are concerned. The neutron can be described by a three dimensional wave packet, which is defined by the momenta distributions in all three spatial directions. If the potential is separable in (x, y, z) then the momentum distribution is also separable. The distribution is typically assumed to be Gaussian with mean wavevectors $k_{x0,y0,z0}$ and variances σ_{k_x,k_y,k_z}. It follows that the spatial coherence volume of the wave packet is given by the product of the coherence lengths $\sigma_{x,y,z} = 1/(2\sigma_{k_x,k_y,k_z})$. The neutron wave function in momentum space along the propagation

direction (conventionally the $\hat{z}$ direction) may then be expressed as:

$$\Phi(k_z) = \left(\frac{1}{2\pi\sigma_{k_z}^2}\right)^{\frac{1}{4}} e^{-\frac{(k_z-k_{z0})^2}{4\sigma_{k_z}^2}}, \tag{1.9}$$

and

$$P(k_z) = \Phi^*(k_z)\Phi(k_z) = |\Phi(k_z)|^2 \tag{1.10}$$

is the corresponding neutron momentum distribution. The normalization constant was chosen so that $\int_{-\infty}^{\infty} P(k_z)dk_z = 1$. The neutron wave function in position space is given by the inverse Fourier Transform of the neutron wave function in momentum space:

$$\Psi(z) = \mathcal{F}\{\Phi(k_z)\} = \frac{1}{\sqrt{2\pi}}\int_{-\infty}^{\infty}\Phi(k_z)e^{ik_z z}dk_z = \left(\frac{1}{2\pi\sigma_z^2}\right)^{\frac{1}{4}} e^{-\frac{z^2}{4\sigma_z^2}}e^{ik_{z0}z} \tag{1.11}$$

and

$$I(z) = \Psi^*(z)\Psi(z) = |\Psi(z)|^2 \tag{1.12}$$

is the probability of neutron's position along the z−direction. It follows that $\int_{-\infty}^{\infty} I(z)dz = 1$. In the separable case the total neutron wave function in momentum space is $\Phi(k) = \Phi(k_x)\Phi(k_y)\Phi(k_z)$ or in position space $\Psi(r) = \Psi(x)\Psi(y)\Psi(z)$.

In the absence of a potential, the momentum variance is time independent, that is $\sigma_k(t) = \sigma_k(0)$ for all t. This states that the divergence of a beam in free space remains constant in time. For a Gaussian wave packet the time dependent position variance (spatial coherence length) has the form:

$$[\sigma_z(t)]^2 = [\sigma_z(0)]^2 + \left(\frac{\hbar t}{2m\sigma_z(0)}\right)^2 \tag{1.13}$$

The spreading of matter waves does not occur for electromagnetic waves because for matter waves each wavelength corresponds to a unique velocity $v = h/(m\lambda)$ whereas for light all wavelengths travel at the same velocity. This is one of the most well-known time-dependent diffraction difference between matter waves and electromagnetic-waves [26].

For $\sigma_z(t) \gg \sigma_z(0)$, or equivalently $t \gg \frac{2m\sigma_z(0)}{\hbar}$ or $L \gg \frac{4\pi\sigma^2(0)}{\lambda}$ where $L = vt$ is the distance traveled in time t, Eq.1.13 simplifies to:

$$\sigma_z(t) \sim \frac{\hbar t}{2m\sigma_z(0)} = \frac{\lambda_{z0}L}{4\pi\sigma_z(0)}. \tag{1.14}$$

For a majority of the work presented in this thesis, a fast neutron produced in a reactor

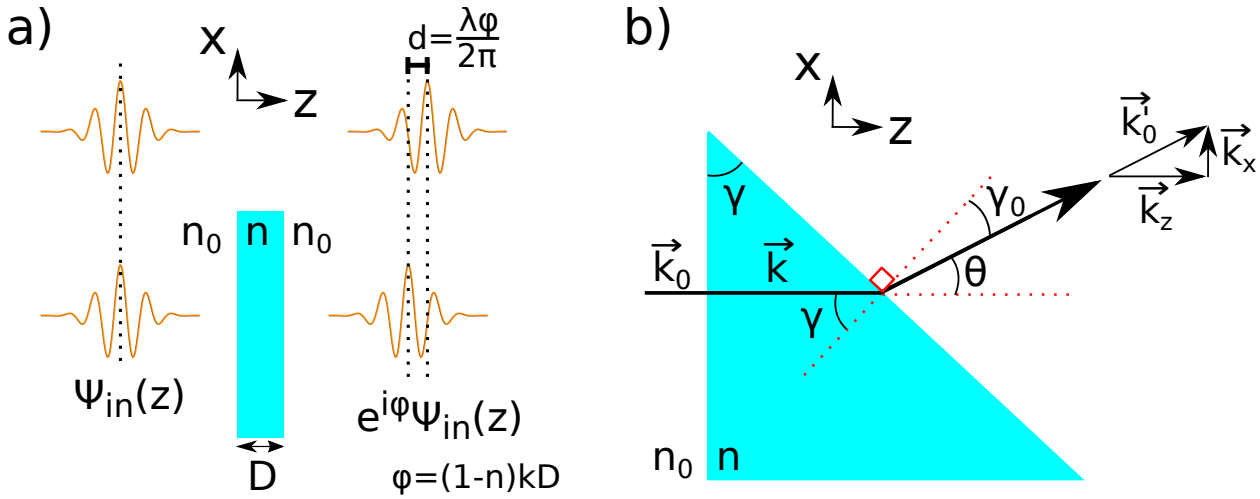

Figure 1.1: a) A wave packet going through a uniform slab of material with an index of refraction "n" acquires a phase shift of ϕ. This phase shift corresponds to a delay of the neutron wave packet relative to the position that it would possess if there was no material. b) Neutron refraction through a prism. The angle of deviation can be derived via Snell's law or by noting that the prism induces a spatially dependent phase shift onto the neutron wave function.

core traverses a neutron guide, the end of which is a slit. After exiting the slit and propagating in free space, the neutron acquires a transverse coherence length of

$$\sigma_{\perp}(L) \sim \frac{\lambda_{z0} L}{s_w} \tag{1.15}$$

where s_w is the width of the slit and L is the distance between the slit and the point of interest. This equation holds because the source of the neutrons, the reactor core, is far away from the slit.

1.3 Quantum Phase

1.3.1 Optical Potential and the Quantum Phase

This thesis only considers time independent potentials. The SE, Eq. 1.4, can then be solved by the method of separation of variables. Assuming that $\Psi(r,t) = \psi_r(r)\psi_t(t)$ the time evolution is given by

$$\psi_t(t) = e^{-iHt/\hbar}. \tag{1.16}$$

Inside of a material neutrons experience an "optical potential". The elastic interaction of a neutron with a sample containing many nuclei at positions R_j can be written as a sum of delta functions. A delta function is denoted by "δ(r)" and has the following two properties:

$$\delta(r-r_0)=\begin{cases}\infty & \text{if } r=r_0\\ 0 & \text{if } r\neq r_0\end{cases}\qquad\text{and}\qquad\int_{-\infty}^{\infty}\delta(r-r_0)dr=1 \tag{1.17}$$

The mean interaction potential, or optical potential for a material is given by [27]:

$$V=\langle V(r)\rangle=\langle\frac{2\pi\hbar^2}{m}\sum_j b_j\delta(r-R_j)\rangle=\frac{2\pi\hbar^2}{m}Nb_c \tag{1.18}$$

where N and b_c are the number density and the coherent scattering length of the material respectively. $N=\rho A_v/M$ where ρ and M are the density and molar mass of the material respectively, and $A_v=6.02214\times10^{23}$ is the Avogadro's number.

After passing through the material (see Fig. 1.1a) the accumulated phase is the integral over the Lagrangian [28]:

$$\phi=\frac{1}{\hbar}\int_{t_0}^{t}\mathscr{L}dt'=\frac{1}{\hbar}\int_{t_0}^{t}(p\cdot v-H)dt'=\int_{x_0}^{x}k\cdot ds-\int_{t_0}^{t}\omega dt' \tag{1.19}$$

Here only energy conserving potentials will be considered, and hence one may ignore the second term which always results in a global phase. For small perturbations:

$$\frac{(p+\delta p)^2}{2m}+V=E\qquad\rightarrow\qquad v\cdot\delta p\approx -V \tag{1.20}$$

We are always interested in the relative phase, $\Delta\phi$, which is the induced phase shift relative to the phase shift in free space:

$$\Delta\phi=\frac{1}{\hbar}\int_{t_0}^{t}\delta p\cdot v dt'\approx-\frac{1}{\hbar}\int_{t_0}^{t}Vdt'=-\frac{1}{\hbar v}\int_{x_0}^{x}Vdx \tag{1.21}$$

As per convention we shall use ϕ to denote $\Delta\phi$. Therefore, when a neutron traveling along the $\hat{z}$ direction passes through a material (Fig. 1.1a), the neutron wave function is integrated over the potential to obtain:

$$\Psi_{out}(z)=\Psi_{in}(z)\int_{-\infty}^{\infty}e^{-\frac{i}{\hbar}\int_{t_0}^{t}Vdt}dk_z=\Psi_{in}(z)\int_{-\infty}^{\infty}e^{-i\frac{Nb_cD2\pi}{k_z}}dk_z\approx\Psi_{in}(z)e^{-i\frac{Nb_cD2\pi}{k_{z0}}}=\Psi_{in}(z)e^{i\phi} \tag{1.22}$$

where V is the optical potential experienced by the neutron inside the material, and D is

the thickness of the material. The phase shift

$$\phi = -Nb_c\lambda_{z0}D \tag{1.23}$$

in a physical sense represents the delay of the neutron wave packet relative to the position that it would possess if there was no material. Or when dealing with spatially dependent optical potentials, it is the relative spatial phase shift. Typical neutron experiments are done with $k_{z0} >> \sigma_{k_z}$ and therefore only k_{z0} may be considered when calculating ϕ. The delay corresponding to the phase shift (see Fig. 1.1a) is given by:

$$d = \frac{\lambda_{z0}}{2\pi}\phi \tag{1.24}$$

Using Eq. 1.21, the neutron transverse wave function after a prism (see Fig. 1.1b) is:

$$\Psi_{out}(x) = \Psi_{in}(x)e^{-i/\hbar\int_{t_0}^{t}Vdt} \approx \Psi_{in}(x)e^{-iNb_c2\pi x\tan(\gamma)/k_{z0}} = \Psi_{in}(x)e^{iqx} \tag{1.25}$$

where γ is the prism incline angle, and $q = -Nb_c2\pi\tan(\gamma)/k_{z0}$. To quantify refraction one needs to analyze the wave function in momentum space which is given by the inverse Fourier transform of the wave function in position space:

$$\Psi_{out}(k_x) = \mathcal{F}^{-1}\{\Psi_{out}(x)\} = \frac{1}{\sqrt{2\pi}}\int_{-\infty}^{\infty}\Psi_{in}(x)e^{iqx}e^{-ik_xx}dx = \left(\frac{1}{2\pi\sigma_{k_x}^2}\right)^{\frac{1}{4}}e^{-\frac{(k_x-q)^2}{4\sigma_{k_x}^2}} \tag{1.26}$$

where a Gaussian form for $\Psi_{in}(x)$ was assumed. Therefore, in this example $k_{x0} = 0$ before the prism and $k_{x0} = q$ after the prism. The refraction angle is:

$$\theta = \sin^{-1}\left(\frac{q}{k_{z0}}\right) = \sin^{-1}\left(\frac{\lambda_{z0}^2Nb_c}{2\pi}\tan\gamma\right) \approx \frac{\lambda_{z0}^2Nb_c}{2\pi}\tan\gamma \tag{1.27}$$

The small angle approximation in the last step is valid for standard materials and thermal neutrons where $\lambda^2Nb_c/\pi \approx 10^{-6}$. Eq. 1.27 describes neutron refraction across a potential boundary, and it is in accordance with the well known Snell's law. In 1621 Willebrord Snellius (Snell) discovered for electromagnetic waves a relationship between the angle of incidence and angle of refraction at the interface between two different isotropic media [29]. This relation is now known as "Snell's law":

$$\frac{n}{n_0} = \frac{k}{k_0} = \frac{\lambda_0}{\lambda} = \frac{v_0}{v} = \frac{c}{v} = \frac{\sin\gamma_0}{\sin\gamma} \tag{1.28}$$

where n is called the index of refraction. The speed and wavelength of light inside a medium are $v = c/n$ and $\lambda = \lambda_0/n$. Hence the frequency $f = v/\lambda$ remains the same (or rather energy $E = hf$ is conserved). In general, the index of refraction is a function of light's frequency

$n = n(f)$, or alternatively wavelength $n = n(\lambda)$. For visible light and common transparent materials n typically decreases with increasing wavelength $\frac{dn}{d\lambda} < 0$. A consequence of this dispersion relation is that white light separates into its component colors after passing through a prism. The typically quoted refractive index of materials are for yellow light ($\lambda = 589$ nm).

"Fermat's Principle" states that light always takes the shortest optical path, or in other words light travels in paths which can be transversed in the least time. In 1662 Pierre de Fermat introduced the idea that the optical path length between two points in space is the geometrical path length times the index of refraction of the material [30]. The optical path length is thus given by the integral of the index of refraction over the geometrical path length:

$$s = \int n dl \tag{1.29}$$

Snell's law (Eq. 1.28) can be derived through Fermat's principle, and vice versa.

It follows that an index of refraction can be defined for neutrons [27]:

$$\frac{n}{n_0} = \frac{k}{k_0} = \frac{\lambda_0}{\lambda} = \frac{v}{v_0} = \frac{\sin\gamma_0}{\sin\gamma} \tag{1.30}$$

In terms of the material properties the index of refraction may be expressed as

$$\frac{n}{n_0} = \sqrt{1 - \frac{V}{E}} = \sqrt{1 - \frac{\lambda^2 N b_c}{\pi}} \approx 1 - \frac{\lambda^2 N b_c}{2\pi} \tag{1.31}$$

One notes that the ratio of velocities for matter waves is inverse to that of light. Also, another difference that arises is that for neutrons the transverse component of velocity is preserved when entering a medium, $v \sin\gamma = v_0 \sin\gamma_0$.

Using Eq. 1.30 the diffraction angle due to a prism (see Fig. 1.1b) is given by:

$$\theta = \gamma - \gamma_0 = \gamma - \sin^{-1}\left(\sqrt{1 - \frac{\lambda_{z0}^2 N b_c}{\pi}}\sin\gamma\right) \tag{1.32}$$

In the small angle approximation where $\lambda^2 N b_c/\pi << 1$, both Eq. 1.27 and Eq. 1.32 approximate to:

$$\theta \approx (1 - n)\tan\gamma \tag{1.33}$$

In a similar fashion diffraction phenomena can also be analyzed using Eq. 1.22. The conceptual difference between the two is that for diffraction the coherence length plays a role, whereas in refraction it does not; for diffraction the coherence length needs to be the size of the features while for refraction it can be infinitesimally small. This approach

to determining diffraction by analyzing the spatially dependent phase profile of the wave function will be used by all subsequent chapters of the thesis.

1.3.2 Quantum Spin and Magnetic Potentials

Neutron's are spin$-1/2$ particles with the following properties:

- they obey the Pauli exclusion principle. Hence, no two neutrons can posses the same quantum numbers. However, given the typical parameters at the neutron interferometry beamlines at the NCNR: flux $\sim 10^{10}$ s^{-1}m^{-2}, neutron speed ~ 1800 m/s, coherence volume ~ 1 nm^3, and beam diameter of ~ 10 mm^3, the probability of two neutrons sharing a phase volume is negligible.
- their distribution over energy levels follow Fermi-Dirac statistics. Given the low flux density and the high temperatures of interest (~ 290 K), the neutron energy spectrum is well described by a Maxwell-Boltzmann distribution.
- they have a quantized intrinsic spin angular momentum of $S = \pm\hbar/2$. The spin state can thus be described by a two-component complex-valued vector called a spinor.

Neutrons have a permanent magnetic moment along the anti-parallel direction of their spin. An external magnetic field defines the spin quantization axis, which is taken to be the $\hat{z}$ axis by convention. The spin state can then be expressed as a linear combination of two eigenstates: the state aligned with the magnetic field called "spin-up" which is represented by $|\uparrow_z\rangle$, and the anti-aligned state "spin-down" represented by $|\downarrow_z\rangle$. It is convenient to use the "bra-ket" notation, where the ket $|\Psi\rangle$ represents the spin wave function and the bra $\langle\Psi|$ represents its conjugate transpose. The two spin states are orthogonal, that is, $\langle\uparrow_z \mid \uparrow_z\rangle = \langle\downarrow_z \mid \downarrow_z\rangle = 1$, and $\langle\uparrow_z \mid \downarrow_z\rangle = \langle\downarrow_z \mid \uparrow_z\rangle = 0$.

Given the normalization constraint of $\langle\Psi|\Psi\rangle = |\Psi|^2 = 1$, an arbitrary spin state is given by:

$$|\Psi\rangle = \cos(\alpha/2)\,|\uparrow_z\rangle + e^{i\beta}\sin(\alpha/2)\,|\downarrow_z\rangle\,. \tag{1.34}$$

The two angles, α and β, can be used to construct a sphere representing the possible states of spin$-1/2$ particles. This Bloch sphere, shown in Fig. 1.2a, is the geometrical representation of a two-level quantum system. The probability that one measures the spin to be in a certain eigenstate is:

$$|\,\langle\uparrow_z\,|\Psi\rangle\,|^2 = \cos^2(\alpha/2) \qquad |\,\langle\downarrow_z\,|\Psi\rangle\,|^2 = \sin^2(\alpha/2) \tag{1.35}$$

It is convenient to use the representation where eigenvectors are assigned to the spin states and the corresponding eigenvalues are the probabilities of occurrence. Setting $|\uparrow_z\rangle = \begin{pmatrix}1\\0\end{pmatrix}$ and $|\downarrow_z\rangle = \begin{pmatrix}0\\1\end{pmatrix}$, the spin wave function can then be expressed as:

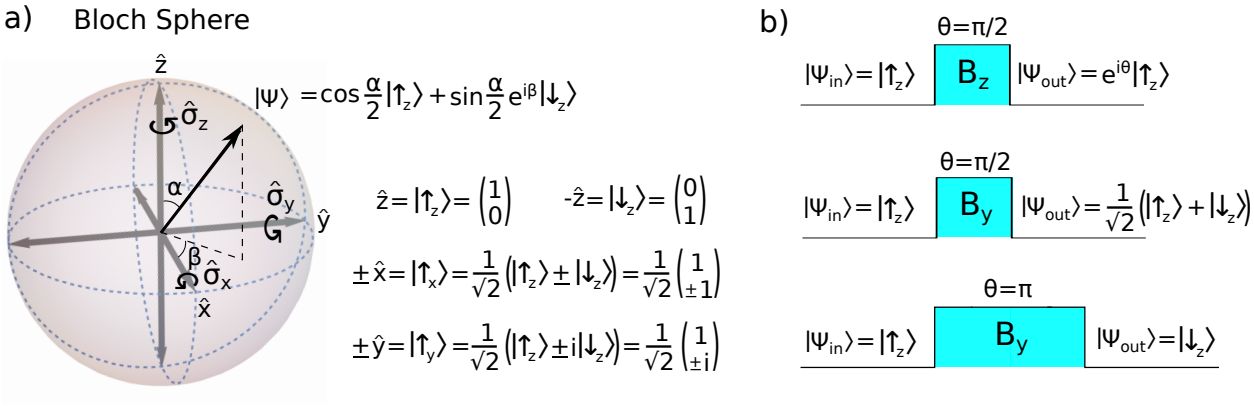

Figure 1.2: a) The neutron spin state can be geometrically represented on the Bloch sphere. b) A magnetic field which is parallel to the spin direction may be used to induce a spin dependent phase shift onto the incoming wave function, while a magnetic field which is perpendicular to the spin direction may be used to rotate the spin vector about the magnetic field axis.

$$|\Psi\rangle = \cos(\alpha/2)\begin{pmatrix}1\\0\end{pmatrix} + e^{i\beta}\sin(\alpha/2)\begin{pmatrix}0\\1\end{pmatrix} = \begin{pmatrix}\cos(\alpha/2)\\ e^{i\beta}\sin(\alpha/2)\end{pmatrix} \tag{1.36}$$

The potential experienced by a neutron inside of a magnetic field is:

$$V_m = -\vec{\mu}\cdot\vec{B} = -|\mu|\vec{\sigma}\cdot\vec{B} = -\frac{\hbar\gamma}{2}(\hat{\sigma}_x B_x + \hat{\sigma}_y B_y + \hat{\sigma}_z B_z) \tag{1.37}$$

where $\vec{\mu}$ is the neutron magnetic moment, $\gamma = 1.832\times10^8$ $\mathrm{T^{-1}s^{-1}}$ is the neutron gyromagnetic ratio, and

$$\hat{\sigma}_x = \begin{pmatrix}0 & 1\\ 1 & 0\end{pmatrix} \qquad \hat{\sigma}_y = \begin{pmatrix}0 & -i\\ i & 0\end{pmatrix} \qquad \hat{\sigma}_z = \begin{pmatrix}1 & 0\\ 0 & -1\end{pmatrix} \tag{1.38}$$

are the Pauli matrices which possess the following commutation relations:

$$[\hat{\sigma}_x, \hat{\sigma}_y] = 2i\hat{\sigma}_z \qquad [\hat{\sigma}_y, \hat{\sigma}_z] = 2i\hat{\sigma}_x \qquad [\hat{\sigma}_z, \hat{\sigma}_x] = 2i\hat{\sigma}_y \tag{1.39}$$

where $[A, B] = AB - BA$ is the commutation operator.

The magnetic field operator, $\hat{U}_m$, is given by Eq. 1.21 with Eq. 1.37. The spin evolution in an external magnetic field is given by:

$$\hat{U}_m|\Psi\rangle = e^{-\frac{i}{\hbar}\int_{t_0}^{t} V_m dt'}|\Psi\rangle = e^{i\frac{\gamma}{2}\int_{t_0}^{t}\vec{\sigma}\cdot\vec{B}dt}|\Psi\rangle \tag{1.40}$$

In the case of time independent magnetic fields the expression for $\hat{U}_m$ simplifies to:

$$\hat{U}_m = e^{i\frac{\gamma t}{2}\vec{\sigma}\cdot\vec{B}} = \mathbb{1}\cos\theta + i(\vec{\sigma}\cdot\vec{n})\sin\theta \tag{1.41}$$

where $\vec{n}$ is the magnetic field unit vector, $\mathbb{1}$ is the identity matrix, and

$$\theta = \frac{\gamma|B|t}{2} \tag{1.42}$$

is the precession angle. It follows from Eq. 1.41 that a magnetic field that is parallel to the spin direction may be used to induce a phase shift similar to Eq. 1.22. Whereas a magnetic field that is perpendicular to the spin direction may be used to obtain an equal superposition of the two spin eigenstates or a complete spin flip. These scenarios are depicted on Fig. 1.2b.

The action of a magnetic field gradient is analogous to the optical potential gradient, and Eq. 1.22 may be used. The calculated dynamics agree with the classical description where in an inhomogeneous magnetic field the force on a magnetic dipole is given by:

$$\vec{F} = m\vec{a} = -\vec{\nabla}U = \vec{\nabla}(\vec{\mu}\cdot\vec{B}) = \pm\frac{\gamma\hbar}{2}\vec{\nabla}|\vec{B}| \tag{1.43}$$

The induced velocity and wavevector are then given by:

$$\vec{v} = \vec{a}t = \pm\frac{\gamma\hbar}{2m}\vec{\nabla}|\vec{B}|t, \qquad \vec{k} = \frac{m\vec{v}}{\hbar} = \pm\frac{\gamma}{2}\vec{\nabla}|\vec{B}|t \tag{1.44}$$

1.4 Neutron Interferometry[1]

1.4.1 Neutrons

In 1931 Walther Bothe and Herbert Becker observed uncharged highly penetrating radiation when they collided alpha particles with beryllium, boron, or lithium [31]. They postulated that this was gamma radiation. In 1932 James Chadwick showed that this radiation consisted of uncharged particles whose mass was similar to that of a proton [32]. For discovering the neutrons Chadwick was awarded the 1935 Nobel Prize in Physics.

Neutrons are subatomic particles with the following properties:

- neutrons are matter waves and are described by a wave function. Their propagation and interaction with potentials is described in section 1.2.
- neutrons experience interactions via all four forces of nature: strong, electromagnetic, weak, and gravitational. The relative strength of the four forces is $1 : 10^{-2} : 10^{-7} : 10^{-39}$ respectively [33].
- the mean radius squared of the neutron is 0.8 fm.

[1] This section is largely taken from Ref. [4–6]

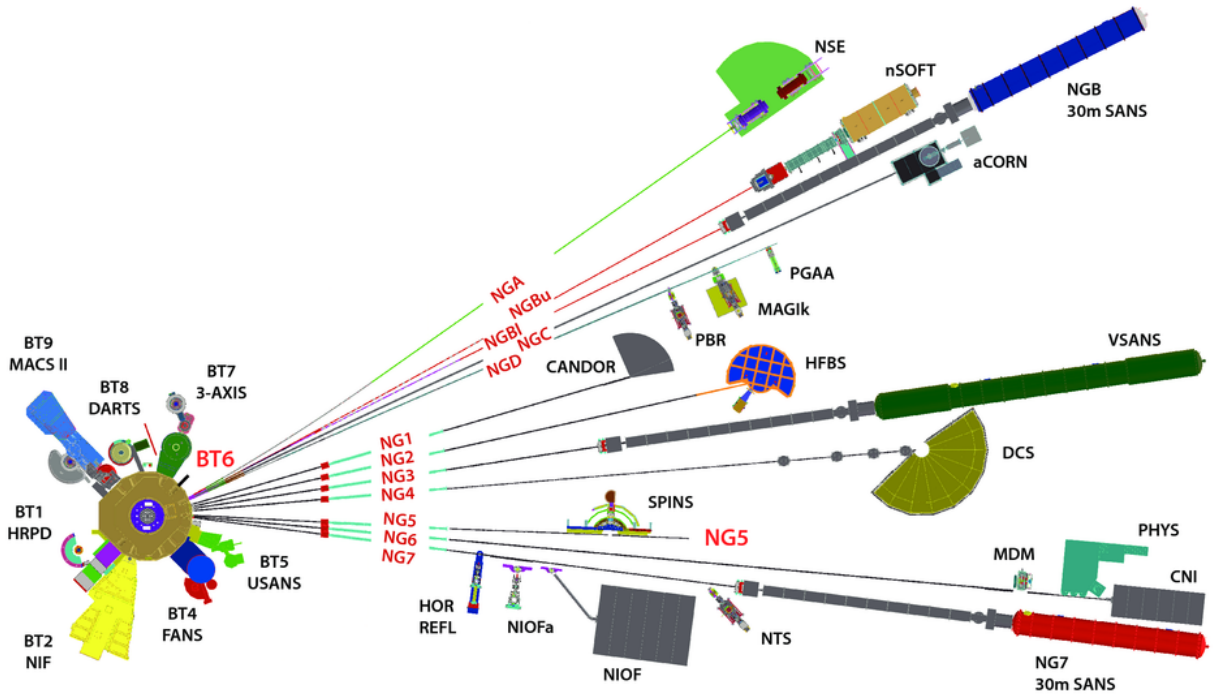

Figure 1.3: 20 MW research reactor at the NCNR. A fast neutron produced in a reactor core is first moderated using heavy water to thermal energies and then further cooled using a liquid hydrogen cold source before traversing a neutron guide. This thesis deals with experiments done at NIOFa, NIOF and the CNI beamlines (located on the bottom two guides). At the NIOFa the neutron beam is extracted by a pyrolytic graphite (PG) monochromator with $\lambda = 0.44$ nm and $\lambda = 0.22$ nm components with an approximate ratio of 3.2:1 in intensity. At the NIOF beamline a PG monochromator extracts $\lambda = 0.271$ nm neutrons. The CNI is located on the NG6 end-station and has a neutron spectrum approximately given by a Maxwell-Boltzmann distribution with $T_c = 40$ K or $\lambda_c = 0.5$ nm. Figure courtesy of NCNR.

- whereas the bound neutrons in an atoms are stable, the lifetime of an unbound neutron (such as the free neutrons produced in nuclear reactors) is around 15 min [34].

The discovery of nuclear fission in 1938 [35] initiated the construction of nuclear reactors for various applications such as power sources of electricity. The category of interest to this thesis is Research Reactors that serve primarily as neutron sources. One such reactor is at the National Institute of Standards and Technology's (NIST) Center for Neutron Research (NCNR), where a 20 MW reactor provides a steady flux of thermal and cold neutrons for a variety of instruments, see Fig. 1.3.

1.4.2 Perfect Crystal Neutron Interferometer

Interferometers employing particle self-interference have proven to be an extremely sensitive measuring tool, allowing for the precise characterization of material properties as well as measurements of fundamental constants. Numerous neutron interferometers (NI) have been

demonstrated: wave front division NI based on single slit diffraction, spin echo NI, amplitude and phase-grating NI, Jamin-type NI, perfect crystal NI, and others [33]. The perfect crystal NI, based on amplitude division, has achieved the most success due to its size and path separation of a few centimeters. Numerous perfect crystal NI experiments have been performed which explore the nature of the neutron and its interactions. For example, the probing of local gravitational fields [36], observing the 4π symmetry of spinor rotation [37], observing orbital angular momentum [15, 16], putting a limit on the strongly-coupled chameleon field [10, 38], implementing quantum information algorithms [39], observing non-classical correlations [40], observing the quantum Cheshire Cat [41], observing the GHZ correlations of a triple-entangled neutron state [42], and the precision measurements of coherent and incoherent scattering lengths [43].

The perfect crystal NI is a macroscopic device whose length is on the order of centimeters. Several perfect crystal NIs that are available at NIST are shown in Fig. 1.4a. A perfect crystal NI is cut from a float-zone grown silicon ingot so that a series of Bragg-diffracting "blades" protrude from a common base. The typical cross section of the incoming neutron beam is $\sim$8 mm by 2 mm. Treating the path degree of freedom as a two-level quantum system we can label the path with the positive momentum in the $\hat{y}$ direction as $|0\rangle = \begin{pmatrix} 1 \\ 0 \end{pmatrix}$ and the path with the negative momentum in the $\hat{y}$ as $|1\rangle = \begin{pmatrix} 0 \\ 1 \end{pmatrix}$, see Fig. 1.4b. Due to the narrow momentum acceptance of the NI, the wave function of incoming neutrons is taken to be a pure state:

$$|\Psi_0\rangle = |0\rangle \tag{1.45}$$

The incoming beam is Bragg diffracted by the first blade into a superposition of two coherent paths. The absorption due to the silicon blades is negligible and hence the blade operator can be expressed as a unitary operator:

$$\hat{U}_B = \begin{pmatrix} t & -r^* \\ r & t^* \end{pmatrix} \tag{1.46}$$

where t and r are the transmission and reflection coefficients. The wave function after the first blade (see Fig. 1.4b) is:

$$|\Psi_1\rangle = \hat{U}_B\,|\Psi_0\rangle = t\,|0\rangle + r\,|1\rangle \tag{1.47}$$

The intensities of the transmitted and reflected beams after a NI blade typically converge to $|t|^2 = .65$ and $|r|^2 = .35$ [7]. Dynamical diffraction theory describes the interaction of photons and matter waves satisfying Bragg and near Bragg diffraction condition in perfect periodic crystal lattices. While the dynamical diffraction theory has been very successful for explaining many diffraction phenomena, the mathematics can be quite cumbersome. We introduced a quantum information model based on a neutron random walk through a perfect

crystal [7,8]. The model greatly simplifies the problem, while accurately predicting dynamical diffraction effects. To verify this quantum information model, we used it to reproduce features of dynamical diffraction that have been studied before such as the intensities in the Borrmann triangle and Pendellösung oscillations. Furthermore, with this new model we proposed and analyzed a novel five blade NI geometry which is both a decoherence free subspace to low frequency vibrations and a refocusing to the dynamical diffraction related phase [8]. A full description of this model can be found in Joachim Nsofini's thesis [2].

Considering the most common three blade Mach-Zehnder (MZ) geometry, the action of the second blade is identical to the first. Since we post-select on the paths which end up at the detector the operator of the second blade can be expressed as:

$$\hat{U}_M = \begin{pmatrix} 0 & -r^* \\ r & 0 \end{pmatrix} \tag{1.48}$$

The wave function after the second blade (see Fig. 1.4b) is:

$$|\Psi_2\rangle = \hat{U}_M |\Psi_1\rangle = -r^* r |0\rangle + rt |1\rangle \tag{1.49}$$

A phase flag is placed inside the interferometer to induce and vary the phase shift between the two paths. The phase flag is typically a uniform slab of material such as quartz, and its action is described by Eq. 1.22. The induced phase shift onto $\lambda = 0.271$ nm neutrons from a 1 mm thick piece of quartz is $\sim 5000°$, which would result in a large loss of contrast as the wave packets in the two paths would be significantly displaced w.r.t. each other (see Fig. 1.1a). In order to compensate for this displacement the phase flag is typically placed across both paths. For small angles of phase flag rotation δ the induced phase difference ϕ_{flag} is approximately linear with δ. As ϕ_{flag} is the relative phase shift between the two paths, the operator of the phase flag can be expressed as:

$$\hat{U}_{flag} = \begin{pmatrix} 1 & 0 \\ 0 & e^{i\phi_{flag}} \end{pmatrix} \tag{1.50}$$

The wave function after the phase flag (see Fig. 1.4b) is:

$$|\Psi_3\rangle = \hat{U}_{flag} |\Psi_2\rangle = -r^* r |0\rangle + rte^{i\phi_{flag}} |1\rangle \tag{1.51}$$

The action of the third blade is identical to the first. This blade acts to recombine and mix the two paths of the interferometer. The wave function after the third blade (see Fig. 1.4b) is:

$$|\Psi_f\rangle = \hat{U}_B |\Psi_3\rangle = \left[-tr^* r - r^* rte^{i\phi_{flag}}\right] |0\rangle + \left[-rr^* r + t^* rte^{i\phi_{flag}}\right] |1\rangle \tag{1.52}$$

The two outgoing beams are called the "O-beam" and the "H-beam". The O-beam is the

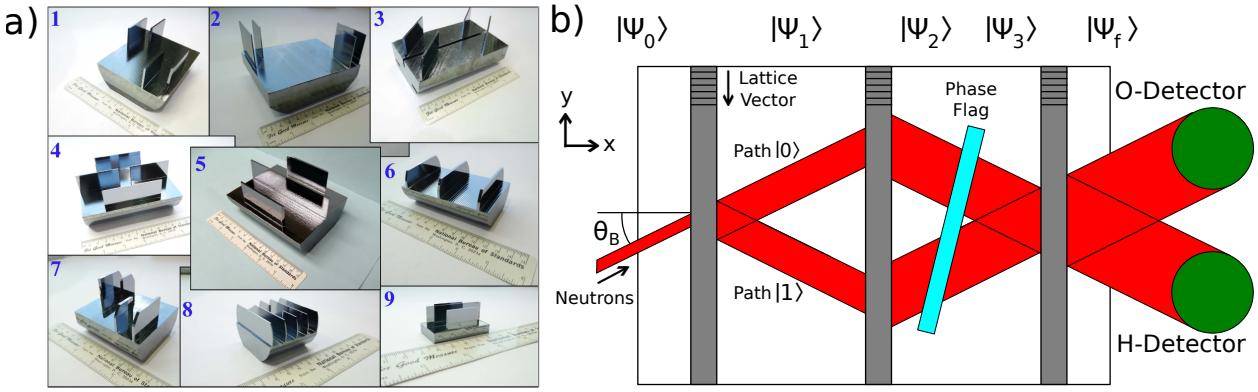

Figure 1.4: a) Examples of perfect crystal silicon neutron interferometers (NIs) at the NCNR. Interferometers 1, 2, 3, and 7 are called "skew symmetric" and they possess a larger space to accommodate samples. Interferometer 5 is the commonly used three blade Mach-Zehnder NI which possess the highest contrast ($\sim$ 90%). Interferometer 8 is the decoherence free subspace NI used in Ref. [39]. Figure taken from Ref. [4]. b) A schematic of the three blade Mach-Zehnder perfect crystal silicon NI. The first blade creates a coherent superposition of two paths inside the interferometer, which are then refocused by the second blade, and interfered on the third blade. The phase shift between the two paths can be varied by rotating the phase flag, typically a precise flat of quartz.

outgoing path which parallel to the direct beam, as per Fig. 1.4b. The intensity at the detectors is given by:

$$I_O = |\langle 0|\Psi_f\rangle|^2 = |r|^4|t|^2(1+\cos[\phi_{flag}]) \tag{1.53}$$

$$I_H = |\langle 1|\Psi_f\rangle|^2 = (|t|^4|r|^2+|r|^6) - |r|^4|t|^2\cos[\phi_{flag}] \tag{1.54}$$

The intensities at the detectors in an experiment deviate from the ideal values and have to be fit to a cosine function:

$$I_O = \mathrm{A} + \mathrm{B}\,\cos[\phi_{flag}+\phi_0] \tag{1.55}$$

where A and B are fit parameters, ϕ_{flag} is the action of the phase flag, and ϕ_0 is an intrinsic phase shift. The intrinsic phase shift is the experiment-dependent, relative phase difference between the two neutron paths and is typically a parameter of interest in a neutron interferometry experiment.

The neutron count rate at the detector follows a Poisson distribution, so that $\Delta N = \sqrt{N}$, where ΔN is the standard deviation of the total counting rate N. This statistical uncertainty is typically the main contributor to the uncertainty in neutron interferometry measurements.

The contrast is a measure of the degree of coherence between the two paths inside the interferometer. Contrast at the detectors is determined from the ratio of the fit parameters (Eq. 1.55) and reflects the depth of the intensity modulations:

$$\mathcal{C} = \frac{\max\{I\}-\min\{I\}}{\max\{I\}+\min\{I\}} = \frac{B}{A}. \tag{1.56}$$

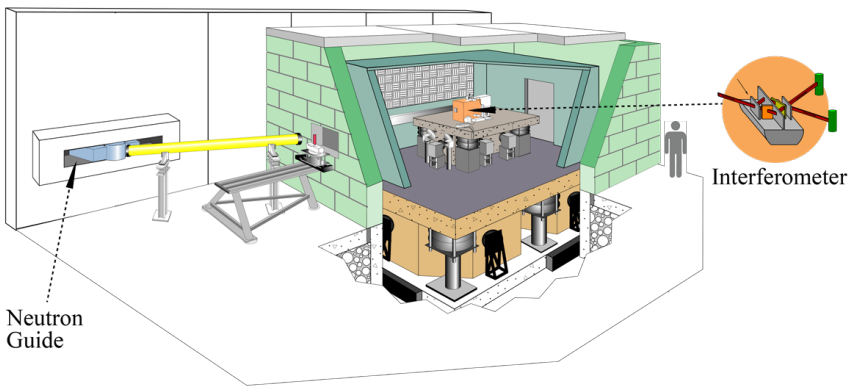

Figure 1.5: The original facility dedicated to neutron interferometry experiments: neutron interferometry optics facility (NIOF). It is a massive enclosure that uses a box within a box within a box approach. The beamline is located on the NG7 guide at the NCNR, see Fig. 1.3. Figure taken from Ref. [4].

The typical contrast at the NCNR is $\mathcal{C} \sim 85\%$. Some of the contrast loss mechanisms come from surface and crystallographic imperfections of the phase flag and the NI blades and are therefore associated with the interferometer itself and not the environment [9]. Machining of interferometers is done with a diamond coated wheel, ensuring that the surfaces of the blades are parallel within a tolerance of a few μm. This is typically followed by chemical etching to remove any residual strain in the crystal lattice. The presence of impurity in the silicon crystal may introduce distortions that spoil the parallelism of the lattice planes. In the case of a wide neutron beam that interacts with a larger section of the interferometer blade, contrast is reduced compared to the optimally located narrow focused beam. Other contrast loss mechanisms originate from changes in the external environment such as acoustic waves, vibrations, temperature gradients, and the humidity of the air, all of which can couple to the NI crystal geometry and internal conditions. In a typical NI with blade separations of $\sim$ 5 cm a neutron with wavelength $\lambda = 0.44$ nm takes $\sim$ 100 μs to pass through the interferometer. The nm sized-wavelength combined with the relatively large NI path length require extreme forms of environmental isolation.

1.4.3 Neutron Interferometry Beamlines at the NCNR

Currently, there are two neutron interferometry facilities at the National Institute of Standards and Technology (NIST) Center for Neutron Research (NCNR) in Gaithersburg, MD, and their layout is depicted on Fig. 1.5 and Fig. 1.6. The original facility, Neutron Interferometry Optical Facility "NIOF", depicted on Fig. 1.5, was built to preserve long-term phase stability [44]. It is a massive enclosure that uses a box within a box within a box approach. The outermost enclosure is a concrete blockhouse that provides environmental and vibrational isolation. It encompasses another massive enclosure that provides passive thermal and acoustic isolation. Finally, the innermost enclosure is a cadmium lined aluminum box that houses the interferometer and detectors. Aluminum and silicon have small neutron absorption cross sections (σ_{a}) and incoherent scattering cross sections (σ_{inc}), while cadmium has a very large absorption cross section. Al: $\sigma_{\mathrm{a}} = 0.231 \times 10^{-24}$ cm^2 and $\sigma_{\mathrm{inc}} = 0.0082 \times 10^{-24}$

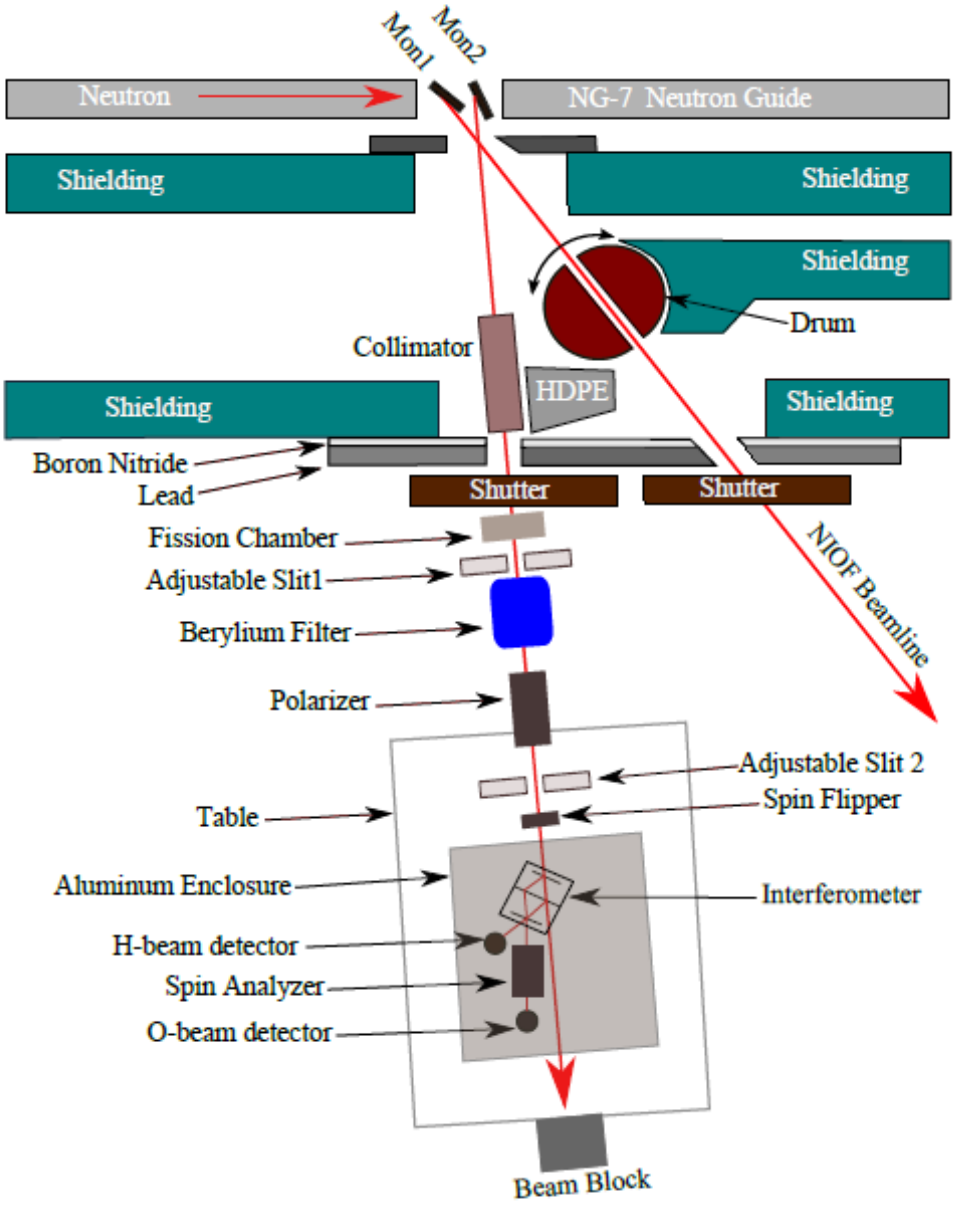

Figure 1.6: The newly constructed beamline dedicated to quantum information enabled neutron interferometry experiments, NIOFa. It is a compact facility with increased accessibility that delivers a higher neutron flux. The beamline is located on the NG7 guide at the NCNR, see Fig. 1.3. Figure taken from Ref. [4].

cm^2; Si: $\sigma_a = 0.171 \times 10^{-24}$ cm^2 and $\sigma_{inc} = 0.004 \times 10^{-24}$ cm^2; Cd: $\sigma_a = 2520 \times 10^{-24}$ cm^2 and $\sigma_{inc} = 3.46 \times 10^{-24}$ cm^2 [45]. These values are for $\lambda = 0.18$ nm neutrons. The neutron transmittance through a material slab of thickness D is given by Lambert's law of beam attenuation:

$$\frac{I}{I_0} = e^{-(\sigma_a + \sigma_{inc})ND}. \tag{1.57}$$

where N is the number density, $N_{Al} = 6.03 \times 10^{22}$ cm^{-3}, $N_{Si} = 5.01 \times 10^{22}$ cm^{-3}, $N_{Cd} = 4.63 \times 10^{22}$ cm^{-3}. Thus, it would take a (Si, Al, Cd) block of thickness (~ 77 cm, ~ 49 cm, ~ 60 μm) to reduce the intensity by 50% of a $\lambda = 0.18$ nm neutron beam.

The enclosure that houses the interferometer is temperature controlled through a set of heaters and is able to maintain a constant internal temperature to within 5 mK. Furthermore, the NIOF is constructed on its own foundation separate from the rest of the building and incorporates a vibration isolation system. With its ability to stabilize the temperature and damp vibrations, the original facility provides exceptional phase stability and high contrast for interferometry experiments.

The new beamline dedicated for quantum information enabled experiments (NIOFa) was built alongside the existing facility on the cold guide NG7, see Fig. 1.6. It is a compact facility with increased accessibility that delivers a higher neutron flux. The motivation for the construction of this beamline was a novel design of a decoherence free subspace NI which was shown to be robust against vibrational frequencies up to 22 Hz [39], therefore diminishing the necessity for traditional massive vibrational isolation enclosures. The neutron beam is extracted from a cold neutron guide by a pyrolytic graphite (PG) monochromator with $\lambda = 0.44$ nm and $\lambda = 0.22$ nm components with an approximate ratio of 3.2:1 in intensity. To change from bichromatic to monochromatic configuration, i.e. filter out the $\lambda = 0.22$ nm component, a liquid nitrogen cooled Be-filter with nearly 100% filter efficiency [4] was installed downstream of the NIOFa entrance slit.

The environmental shielding at NIOFa largely differs from the design of the original facility. Its main wall consists of tall paraffin wax and steel shot-filled-steel walls surrounding the neutron guide. The interferometer's only enclosure is a cubic aluminum box with a length of 76.2 cm per side. The box is similarly lined with cadmium to decrease neutron background and sits on a 3 mm thick fiberglass base that isolates it thermally from the optical table.

1.4.4 Neutron Interferometry in Vacuum[2]

The compactness of the NIOFa facility comes at the expense of long-term phase stability and requires novel methods of environmental isolation. Thermal isolation of the neutron interferometer was achieved by using a vacuum chamber, which shields the interferometer from temperature fluctuations inside the guide hall.

We demonstrated the functionality of a neutron interferometer in vacuum and characterize the use of a compact vacuum chamber enclosure as a means to isolate the interferometer from spatial temperature gradients and time-dependent temperature fluctuations [6]. The

[2]This section is largely taken from Ref. [6]. The lead authors were Parminder Saggu and Taisiya Mineeva.

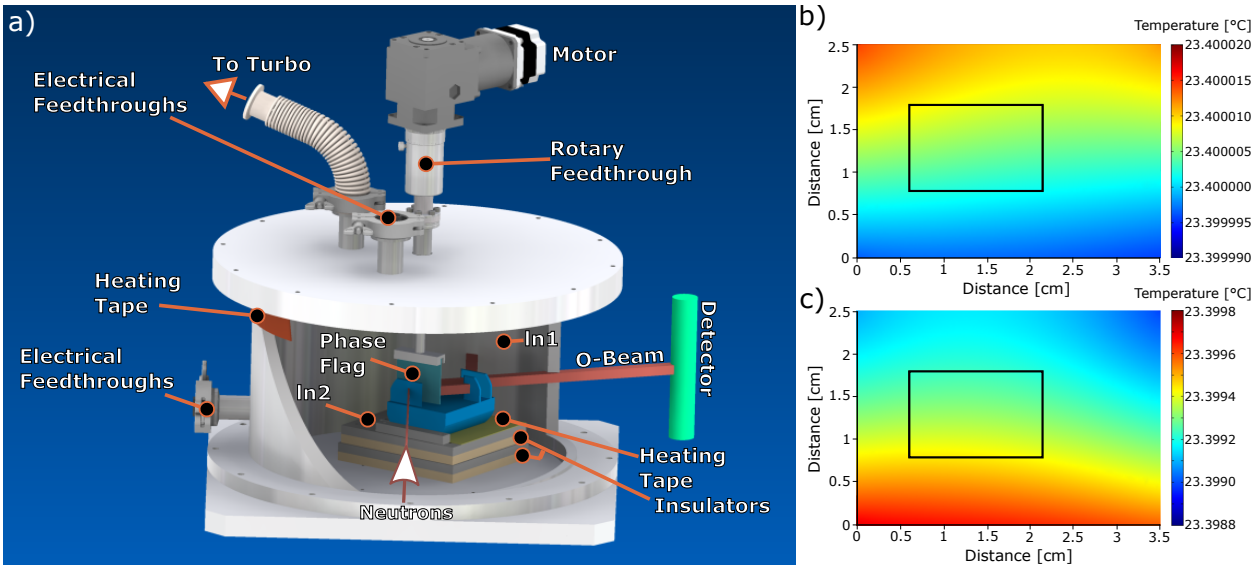

Figure 1.7: a) Cross-sectional sketch of the vacuum chamber with the interferometer inside. b-c) Simulated temperature across the last NI blade given the setup in the chamber with the heating element on the wall of the vacuum chamber set to 23.5 °C and the heating element at the base of interferometer set to 23.4 °C. The black rectangle depicts the expected neutron beam size. b) The temperature variance across the blade given an ambient temperature of 23 °C and c) given an ambient temperature of 19 °C. The simulated temperature variances are 0.00003 °C and 0.001 °C respectively. Figures taken from Ref. [6].

vacuum chamber is found to have no depreciable effect on the performance of the interferometer (contrast) while improving system stability, thereby showing that it is feasible to replace large temperature isolation and control systems with a compact vacuum enclosure for perfect crystal neutron interferometry.

The vacuum chamber was constructed from aluminum 6061-T6 because of its low neutron scattering and absorption cross-sections. The body of the vacuum chamber is an aluminum tube with an inner diameter of 30.5 cm, an outer diameter of 32.5 cm, and an inner height of 20.3 cm giving a total enclosed volume of roughly 14830 cm^3. The top and bottom plates along with flanges were designed with grooves appropriate for Fluoropolymer O-rings. Flanges were welded onto the aluminum tube and were then screwed into upper and lower aluminum plates to close the chamber.

The vacuum chamber (Figure 1.7a) was placed inside of a cubic, cadmium-lined aluminum box. The chamber itself was supported by the rotation, translation and height stages for optical alignment of the NI with the neutron beam. The interferometer was placed inside the chamber on a specially machined aluminum cradle. A polyoxymethylene plate was sandwiched between the base of the cradle and the vacuum chamber, secured using screws made from the organic thermoplastic polymer, polyether ether ketone (PEEK). Both Polyoxymethylene and PEEK were selected as insulators to prevent heat transfer between the vacuum chamber and the interferometer because of their good mechanical properties. To minimize temperature gradients inside the chamber two heating elements were installed: an internal one located below the interferometer base (denoted as "In2" on Fig. 1.7a) and an

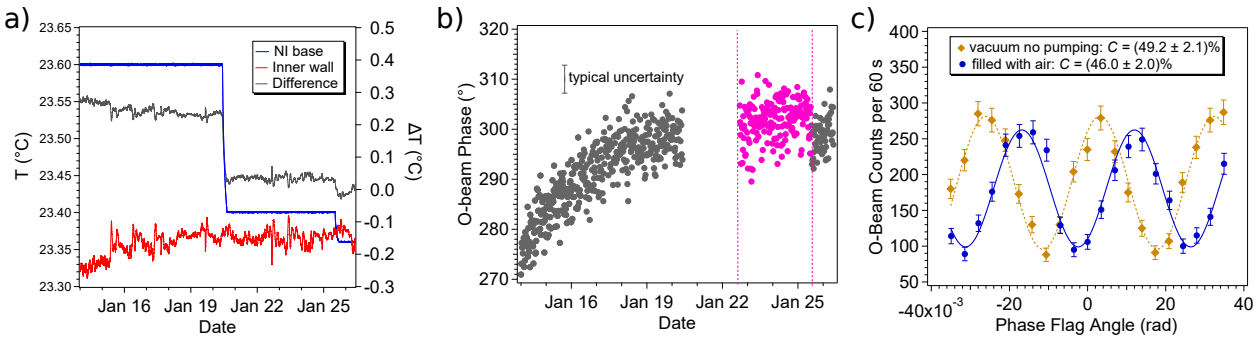

Figure 1.8: a) Temperature measurements at the inner chamber wall using ln1 (red, scale on left), interferometer base using ln2 (blue, scale on left), and their difference (grey, scale on right). b) Corresponding phase measurements. The gap in the phase measurements between January 20$^{\text{th}}$ and 22$^{\text{nd}}$ stems from the reactor shutdown. A typical phase uncertainty is shown. This uncertainty is purely statistical and at the 68% confidence level. c) Contrast measurements taken at ambient pressures (no vacuum or 760 Torr) (blue curve) and at 10^{-4} Torr with the turbo pump turned off (yellow curve). Phase uncertainties are purely statistical at the 68% confidence level. Figures taken from Ref. [6].

external one that was wrapped around the outside of the vacuum chamber walls (denoted as "In1" Fig. 1.7a).

There are a number of vacuum compatible feedthroughs on the vacuum chamber. The first one is a rotary feedthrough to hold and rotate the phase flag. The second provides a connection to a vacuum pump while the third and fourth provide electrical connections for thermistors taped to the inner wall of the vacuum chamber and to the heater on the interferometer cradle. All electrical leads are twisted pairs to minimize stray magnetic fields. The two probes inside the vacuum chamber monitor the temperature difference between the wall of the chamber and the interferometer. A third probe, a Pt 100 resistor, was taped to the outside of the vacuum chamber to gauge the overall temperature insulation provided by the chamber.

3D numerical simulations of the setup were done using finite element analysis to gain insight into the temperature variation across the interferometer. The simulation geometry closely resembles the setup shown in Figure 1.7a, and consists of the vacuum chamber, heating elements, skew symmetric NI, and the depicted cradle under the NI. Actual dimensions and material properties of those elements were used. Since the NI sits in the middle of vacuum chamber with two heating elements, one around the outside of the chamber walls and one directly under the interferometer base, both radiating and conducting heat transfer mechanisms were considered in our simulations. Initial simulations show that in order to maintain a stable temperature at the interferometer, it needs to be in contact with the heating element via a good thermal conductor. For that reason, we removed the insulating felt that has been historically placed under the NI base.

Figures 1.7b and 1.7c depict the simulated temperature within the central cross section of the analyzer blade when the heating elements for the wall of the vacuum chamber and the base of interferometer were set to fixed temperatures of 23.5 °C and 23.4 °C respectively. The choice of the set temperatures of the heating elements in the simulations reflects

experimentally determined temperature combinations for which phase stability was achieved.

Figure 1.7b shows that for an external ambient temperature of 23 °C in such a configuration, the temperature across the last blade of the NI varies by 30 °μC; while Figure 1.7c shows that for an external ambient temperature of 19 °C the temperature varies by 1 °mC. This is a factor of 100 more variation caused by a shift of only 4 °C external. The black rectangle specifies the expected neutron beam size at the last NI blade, while the external temperature range reflects the typical temperature variance in the guide hall throughout the year.

The vacuum system was tested at the new beam line (NIOFa) using a four blade skew-symmetric NI and $\lambda = 0.22$ nm neutrons. Data for phase stability was collected over a period of several months. From Jan 15^{th} to Jan 20^{th} the heating element at the wall of the vacuum chamber was set to 23.5 °C and the heating element at the base of interferometer was set to 23.6 °C. The temperatures were measured using two thermistors, placed near the NI base and on the inner chamber wall. Figs. 1.8a and 1.8b show the temperature and phase measurements for a subset of our data. The temperature difference between the base of the NI and the inner wall of the chamber was around 0.4 °C and the phase drifted by approximately 30 ° over a span of 5 days.

We achieved higher phase stability as we reduced the set point of the heating tape at the base of the NI to 23.4 °C so that the temperature difference between the inner vacuum chamber walls and the NI base was minimized. The temperature at the base of the interferometer was well stabilized between 23.400 ℃ and 23.401 ℃. During a 3 day period, we observed high phase stability, with no appreciable drift. A linear fit of the data depicted in Fig. 1.8b obtains a slope of only (0.003 ± 0.03) deg/hr at the 68% confidence level.

We further examined the effect of the vacuum enclosure on the contrast of the NI by taking $\sim$ 30 min interferogram scans. The question being investigated was whether the vacuum would induce contrast-destroying strain on the NI crystal and whether the vacuum enclosure is compatible with the rest of the NI setup. The contrast scan without the vacuum chamber was around 54% while the contrast in an air-filled vacuum chamber was around 46%; a change in contrast most likely due to difference in the position of the interferometer before and after installation of the chamber. When comparing contrast with the vacuum chamber in place, contrast increases at lower pressures (Fig. 1.8c).

Using the turbo pump, the chamber was pumped down to its lowest achievable pressure of $4 \cdot 10^{-4}$ Torr. While the pump was operating, the contrast dropped to 37% due to mechanical vibrations caused by the pump. After the pump was turned off, with an initial pressure of 10^{-4} Torr the contrast increased to approximately 49%.

We therefore conclude that one can operate a perfect crystal neutron interferometer with high contrast and phase stability inside a vacuum chamber.

1.5 Two-level Quantum Systems and Coherent Superpositions

Here we will consider two-level quantum systems, also known as “qubits”, which are quantum analogues of classical bits. A classical bit is a basic unit of information which can have only

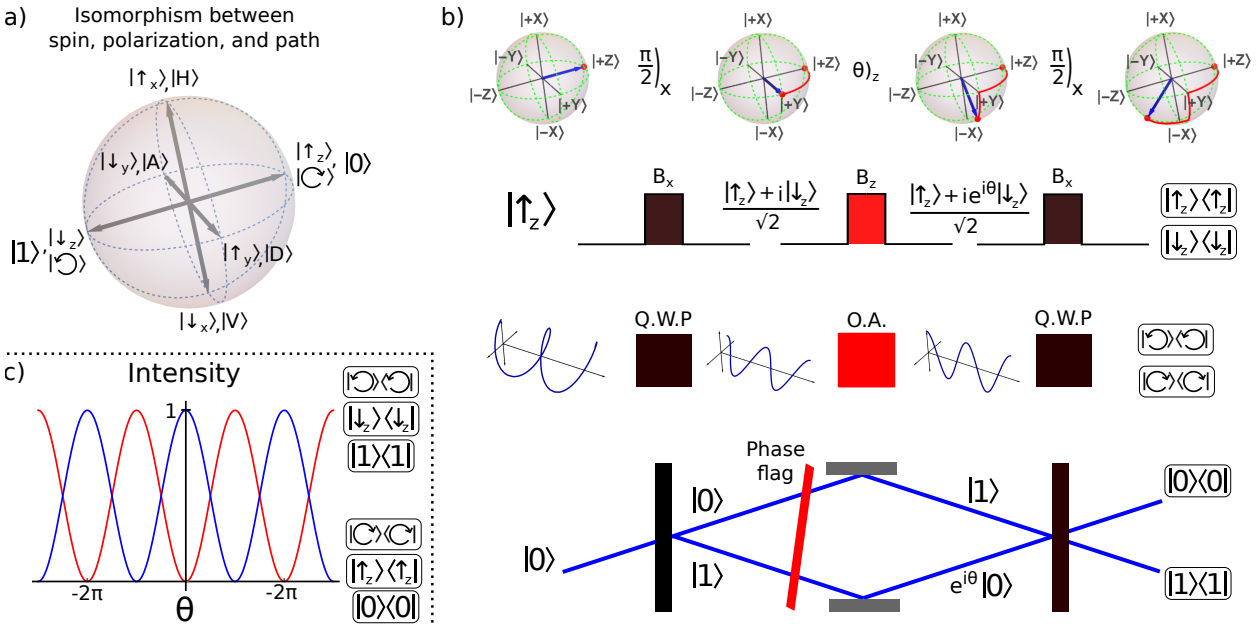

Figure 1.9: a) Isomorphism between the two-level quantum systems: spin state of fermions, polarization state of light, and the path inside of an interferometer. b) An analogous Ramsey fringe sequence with spin, polarization, and interferometer path. For the {spin, polarization, path}: the system starts in a {spin state along the $\hat{z}$ direction, circularly polarized light, path 0}; then a {magnetic field pulse along the $\hat{x}$ direction, quarter wave plate (Q.W.P), first crystal blade} creates a superposition of the two eigenstates; then a {magnetic field pulse along the $\hat{z}$ direction, material with optical activity (O.A.), phase flag} induces a phase shift between the two eigenstates; and finally a {magnetic field pulse along the $\hat{x}$ direction, Q.W.P, last crystal blade} mixes the two eigenstates. c) Post-selecting on one eigenstate results in Ramsey fringes which are sinusoidal oscillations as a function of the phase shift.

one of two outcomes, usually represented by 0 and 1. The qubit on the other hand can be in a state of superposition of both outcomes. Therefore the quantum superposition allows for interference effects which correlate the probabilities of the outcomes.

Two-level quantum systems are described by Eq. 1.36, and they are geometrically represented by the Bloch sphere (see section 1.3.2). This common description is due to the fact that there is an isomorphism between all two-level systems. In this thesis we consider three different two-level quantum systems: the quantum spin of a neutron, the polarization state of light, and the two paths of an interferometer.

The spin eigenstates are denoted by $s \in \{\uparrow_x, \downarrow_x, \uparrow_y, \downarrow_y, \uparrow_z, \downarrow_z\}$, the polarization states of light are denoted by $p \in \{H, V, D, A, \circlearrowleft, \circlearrowright\}$, the two paths of the interferometer are denoted by $path \in \{0, 1\}$. We may put these on a Bloch sphere (see Fig. 1.9a), where by convention the propagation axis is the $\hat{z}$ axis. A phase shift may be induced along any axis for any degree of freedom (DOF). In the case of spin, a magnetic field along $\{\hat{x}, \hat{y}, \hat{z}\}$ direction induces a phase shift on the spin DOF along $\{\hat{\sigma}_x, \hat{\sigma}_y, \hat{\sigma}_z\}$. For the polarization DOF a birefringent material with its optics axis along the $\{\hat{x}, \hat{x} - \hat{y}\}$ direction provides a phase shift along the $\{\hat{\sigma}_x, \hat{\sigma}_y\}$. A material with optical activity provides a phase along $\hat{\sigma}_z$. Inside of an interferometer a phase flag provides a $\hat{\sigma}_z$ phase shift for the path DOF. Note that the operator differences between polarization and spin come from the fact that on the Poincaré sphere that describes optical polarization, any two antipodal points refer to orthogonal polarization directions; while on the Bloch sphere that describes the spin-1/2 state, any two antipodal points refer to anti-parallel spin directions.

Coherence in two-level quantum systems may be illustrated by a Ramsey fringe sequence, which we can demonstrate via any system (see Fig. 1.9b):

$$|\Psi_R\rangle = e^{i\frac{\pi}{2}\hat{\sigma}_x} e^{i\frac{\theta}{2}\hat{\sigma}_z} e^{i\frac{\pi}{2}\hat{\sigma}_x} \begin{pmatrix} 1 \\ 0 \end{pmatrix} \tag{1.58}$$

The first $\pi/2)_x$ term creates a superposition of the two eigenstates. For convenience here we have considered the operator which creates an equal superposition. The second term adds a phase shift of θ. The last $\pi/2)_x$ term mixes the two eigenstates. The probability of post-selecting onto a specific eigenstate at the output is:

$$|\langle \hat{z}|\Psi_R\rangle|^2 = \cos^2\left(\frac{\theta}{2}\right) \qquad |\langle -\hat{z}|\Psi_R\rangle|^2 = \sin^2\left(\frac{\theta}{2}\right) \tag{1.59}$$

These θ dependent oscillations are depicted in Fig. 1.9c, and they are known as Ramsey fringes. In a spin Ramsey fringe the probabilities of $\{\uparrow_z, \downarrow_z\}$ at the output are varied by the magnetic field pulse between the $\pi/2$ spin pulses. In a polarization Ramsey fringe the probabilities of $\{\circlearrowleft, \circlearrowright\}$ at the output are varied by the material with optical activity which is between the quarter wave plates. In an interferometer the probabilities of path $\{0, 1\}$ at the output are varied by the phase flag between the interferometer blades.

Chapter 2

Phase-Grating Moiré Interferometry[1]

2.1 Introduction and Historical Background

The discovery of the neutron led to the construction of a variety of phase sensitive neutron interferometers. Neutrons in particular are a convenient probe due to their relatively large mass, electric neutrality, and sub-nanometer-sized wavelengths. The earliest neutron interferometer (NI) was formed via a biprism, and through wavefront division achieved Fresnel interference effects with up to 60 μm path separations [46]. Amplitude division created by Bragg diffraction off of crystal lattice planes was later used to make perfect crystal NIs with MZ path separations of several centimeters [47], see section 1.4. This relatively large path separation along with the macroscopic size of the interferometer contributed to its success in exploring the nature of the neutron and its interactions. However, perfect crystal NIs posses a very narrow wavelength acceptance, are difficult to fabricate, and operate only under stringent forms of vibration isolation and beam collimation [4–6, 44, 48]. This limits their wide spread adaption at many neutron sources.

Advances in micro- and nano-fabrication of periodic structures with high aspect ratios and features ranging between 1 μm to 100 μm enabled employing absorption and phase-gratings as practical optical components for neutron beams. The first demonstration of a Mach-Zehnder based grating NI in 1985 [49] used 21 μm periodic reflection gratings as beam splitters for monochromatic (λ = 0.315 nm) neutrons. A few years later, a three transmission phase-grating Mach-Zehnder NI was demonstrated for cold neutrons (0.2 nm $< \lambda <$ 50 nm) [50–53]. The need for cold- or very cold- neutrons with a high degree of collimation limits the use of such interferometers in material science and condensed matter research.

An alternative approach was the Talbot-Lau interferometer (TLI) proposed by Clauser and Li for cold potassium ions and x-ray interferometry [54], and implemented by Pfeiffer *et al.* for neutrons [55]. The TLI is based on the near-field Talbot effect [56] and uses a combination of absorption and phase-gratings. The Talbot effect or self imaging phenomena occurs for beams with periodic spatial phase profiles, and it dictates that a self image of the periodic profile will be reproduced at the Talbot distances in the near-field region, see Fig. 2.1. In the TLI setup the sample, introduced in front of the phase-grating, modifies

[1]The material in this chapter is largely taken from Refs. [11–14].

the phase and amplitude of the Talbot self-image. Since neutron sources are comparatively weak to x-ray sources, a challenge in developing neutron phase imaging is overcoming the low intensity that is an outcome of requiring small apertures to produce quasi-coherence in the transverse directions. The use of a neutron TLI was the first solution to this problem by requiring coherence in only one direction, enabling the use of a source grating which reduced the intensity by about 60% rather than several orders of magnitude as was required for use of the transport of intensity method [57]. A neutron TLI typically uses a monochromatic beam ($\Delta\lambda/\lambda$ ranges from 1% to 25%) and is composed of three gratings: a source grating made of gadolinium with a period of the order of 1 mm; a phase modulating grating with combs etched in silicon with period of order 10 μm and aspect ratios of order 10; and an analyzer grating made of gadolinium with period of the order 5 μm [55, 58, 59]. The period and aspect ratio required for the analyzer grating remains a fabrication challenge. The use of a monochromatic beam is preferred as the Talbot distance where one obtains the self-image is inversely proportional to wavelength and the depth of the combs in the phase modulating grating is chosen to produce a π phase modulation for the working wavelength. Even though chromatic sensitivity of the TLI is reduced, thus leading to a gain in neutron intensity, in this setup the absorption gratings are challenging to manufacture and limit the incident flux reaching the detector; while the neutron wavelength spread will cause contrast loss as the distance to interference fringes (fractional Talbot distance) is inversely proportional to the neutron wavelength.

It has been previously demonstrated for atoms and electromagnetic waves that the two grating TLI setup produces fringes in the far-field [60–63]. This "Lau effect" [64] requires the first grating to be an intensity mask which serves as an array of mutually incoherent sources, and the second grating is either an intensity or a phase mask which through Fresnel diffraction results in the interference pattern on the screen. When the distance between the two gratings is at multiples of half Talbot length, an image of the first grating is produced at the plane at the second grating, and that image beats with the second grating to produce the beat pattern in the far-field downstream.

Both Lau and Talbot effects turned out to be special cases of a more universal moiré effect. Our colleagues from NIH had demonstrated this universal moiré effect for X-Rays [65], and together we have demonstrated it for neutrons. In regards to the Lau and Talbot effects, the conceptual step forward of the neutron phase-grating moiré interferometer (PGMI) is to go to the other end of the moiré effect spectrum for the matter waves, where two pure phase masks produce a beat pattern when both the source and the detector are in the far-field range. This interference would be observed even if the two phase-gratings are in contact, provided that their periods are appropriately different, see Fig. 2.10.

The main differences between the PGMI and the neutron Talbot-Lau grating interferometer are that only phase-gratings are used, a broader wavelength distribution is accepted, and the fringes are observed in the far-field. The phase moiré effect in the far-field produces large period interference fringes that are orders of magnitude larger than the period of the gratings, enabling direct detection with an imaging detector without the need for an absorbing analyzer grating. Thus a greater intensity is transmitted through a PGMI and the PGMI has comparatively relaxed grating fabrication requirements especially at smaller grating periods. In addition, grating alignment for the PGMI is an order of magnitude less stringent compared to the perfect crystal NI whose individual diffracting elements must be aligned

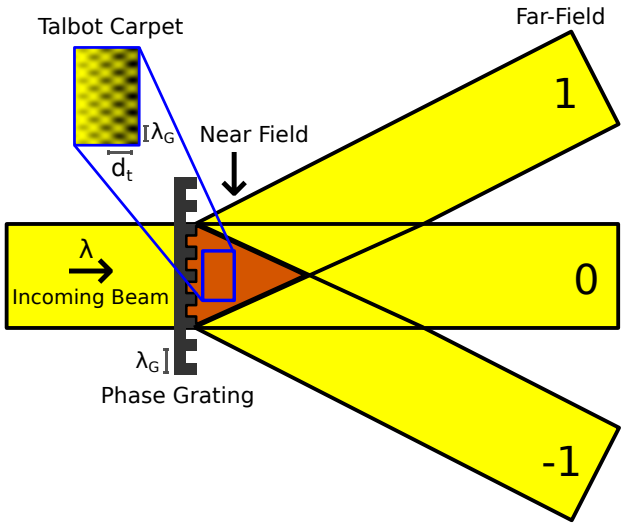

Figure 2.1: Beam diffraction after a phase-grating with period λ_G. The region after the phase-grating where the diffraction orders have not yet been separated is known as the near-field region. Self-imaging phenomena occur in this region and the intensity forms a pattern known as the Talbot carpet. In the Talbot carpet the grating profile is repeated at Talbot distances $d_t = 2\lambda_G^2/\lambda$, where λ is the wavelength of the beam. In the far-field the diffraction orders (-1,0,1) separate and the intensity profile is indicative of the beam's momentum distribution.

relative to each other to within 0.01 arcsec [66]. Other advantages of this setup include the use of widely available thermal and cold neutron beams, large, variable interferometer area, and the broad, simultaneous wavelength acceptance.

This chapter describes the implementation of the PGMIs operating in the far-field regime. Section 2.2 describes the experiments to characterize the action of the phase-gratings onto a neutron beam using momentum projective measurements [11]. Section 2.3 describes the implementation of the two PGMI [12]. Section 2.4 describes the experiment to use the two PGMI to measure the microstructures of samples [13]. Section 2.5 describes the implementation of the three PGMI [14].

2.2 Characterization and Optimization of Neutron Phase-Gratings[2]

This section describes the experiments to characterize the action of the phase-gratings onto a neutron beam using momentum projective measurements. Neutron diffraction from phase-gratings was characterized using Bragg diffraction crystals to resolve individual diffraction orders. Well-defined diffraction peaks are observed and perturbations to the diffraction peaks as a function of grating alignment is explored. This lends itself to directly assessing the grating quality. Furthermore this technique may be able to improve the contrast of the grating interferometers by providing in-situ aides to grating alignment.

[2]This section is largely taken from Ref. [11]. The lead author was Benjamin Heacock.

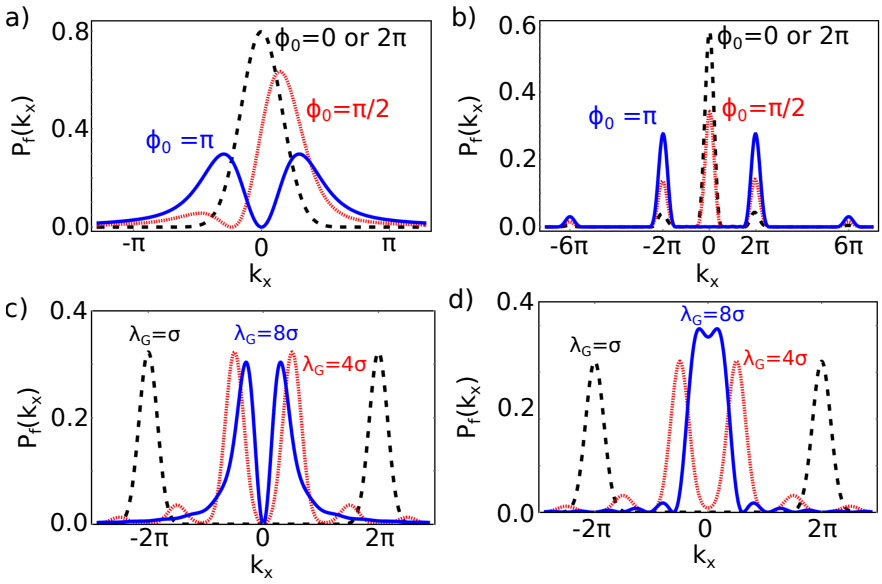

Figure 2.2: Transverse momentum distribution of a Gaussian wave packet with a spatial coherence length of $\sigma = 1$ after passing through (a) a ϕ_0 step potential (b-d) a 50% comb-fraction phase-grating with period λ_G and phase amplitude ϕ_0. In (c,d) the neutron wave packet is on axis with a (phase jump, phase step) of the phase-grating. Therefore, as the period is increased the profile in (c) approaches the profile seen in (a). Figure taken from Ref. [11].

2.2.1 Theory

Neutron optics rely on refraction and diffraction phenomena for beam control and manipulation [67]. Various shapes of materials with unique neutron indices of refraction can be constructed to induce phase shifts, diffraction, beam displacements, and spin-dependent interactions. The action of such components may intuitively be understood by noting that writing a spatially-dependent phase over the neutron wave function modifies its momentum distribution, see section 1.3.

Consider the transverse portion of the spatial wave function $\Psi_i(x)$ of an incoming neutron wave packet which is propagating in the $\hat{z}$ direction. Applying a spatially dependent phase $\phi(x)$ over the incoming wave function results in an outgoing wave function of

$$\Psi_f(x) = e^{-i\phi(x)}\Psi_i(x). \tag{2.1}$$

To analyze diffraction phenomena we look at the neutron wave function in momentum-space:

$$\Phi_f(k_x) = \mathcal{F}\{\Psi_f\} = \mathcal{F}\{e^{-i\phi(x)}\} * \mathcal{F}\{\Psi_i\}, \tag{2.2}$$

where $\mathcal{F}\{...\}$ is a Fourier transform, and $*$ is the convolution operator. In our experiments we measure the outgoing neutron momentum distribution, which is calculated as:

$$P_f(k_x) = \Phi_f^*(k_x)\Phi_f(k_x) \tag{2.3}$$

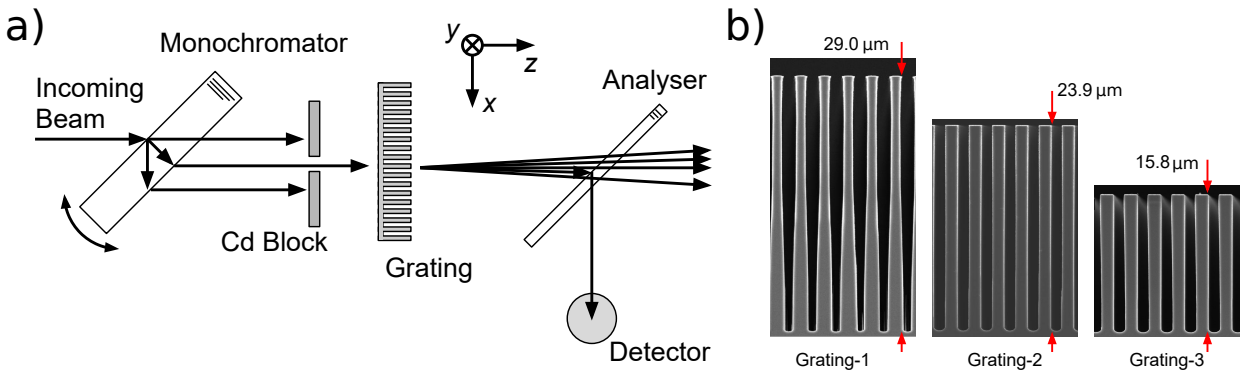

Figure 2.3: (a) Experimental setup. $\lambda = 0.44$ nm neutron beam is spectrally narrowed and collimated by passing through a monochromator crystal and a slit. The resulting beam passes through a grating whose effect is measured by an analyzer crystal and proportional counter. The grating was rotated around all three coordinate directions. (b) SEM micrographs of the three gratings that were used in the experiment. Figure taken from Ref. [11].

where $\Phi_f^*(k_x)$ is the complex conjugate of $\Phi_f(k_x)$.

The action of a spatially dependent phase shift is nicely illustrated by considering a neutron wave packet passing on-axis thorough a phase step potential of magnitude ϕ_0:

$$\Psi_f(x) = e^{-i\frac{\phi_0}{2}\mathrm{sgn}[x]}\Psi_i(x), \tag{2.4}$$

where sgn[...] is the sign function. The outgoing transverse momentum distribution can be calculated via Eq. 2.3. Fig. 2.2a shows outgoing momentum distributions for the case of an incoming Gaussian wave packet and various ϕ_0 amplitudes.

The induced phase onto a neutron wave packet due to the phase-step is directly proportional to the momentum (or wavelength $\lambda_z = 2\pi/k_z$) along the propagation axis:

$$\phi(x) = -Nb_c\lambda_z D(x), \tag{2.5}$$

where Nb_c is the scattering length density of the phase-step material and D(x) is the thickness of the phase-step at location x. Therefore for broad wavelength distributions one must integrate over the wavelength as each λ_z corresponds to a particular ϕ_0.

If a neutron wave packet passes through a phase-grating of period λ_G, then $P_f(k_x)$ will exhibit diffraction peaks with angular separations of

$$\theta = \sin^{-1}\left(\frac{n\lambda}{\lambda_G}\right), \tag{2.6}$$

where n is an integer and represents the diffraction order. The relative amplitudes of the diffraction peaks will depend on the shape and amplitude of the phase profile. For example, the phase profile of a 50% comb-fraction square wave phase-grating is given by

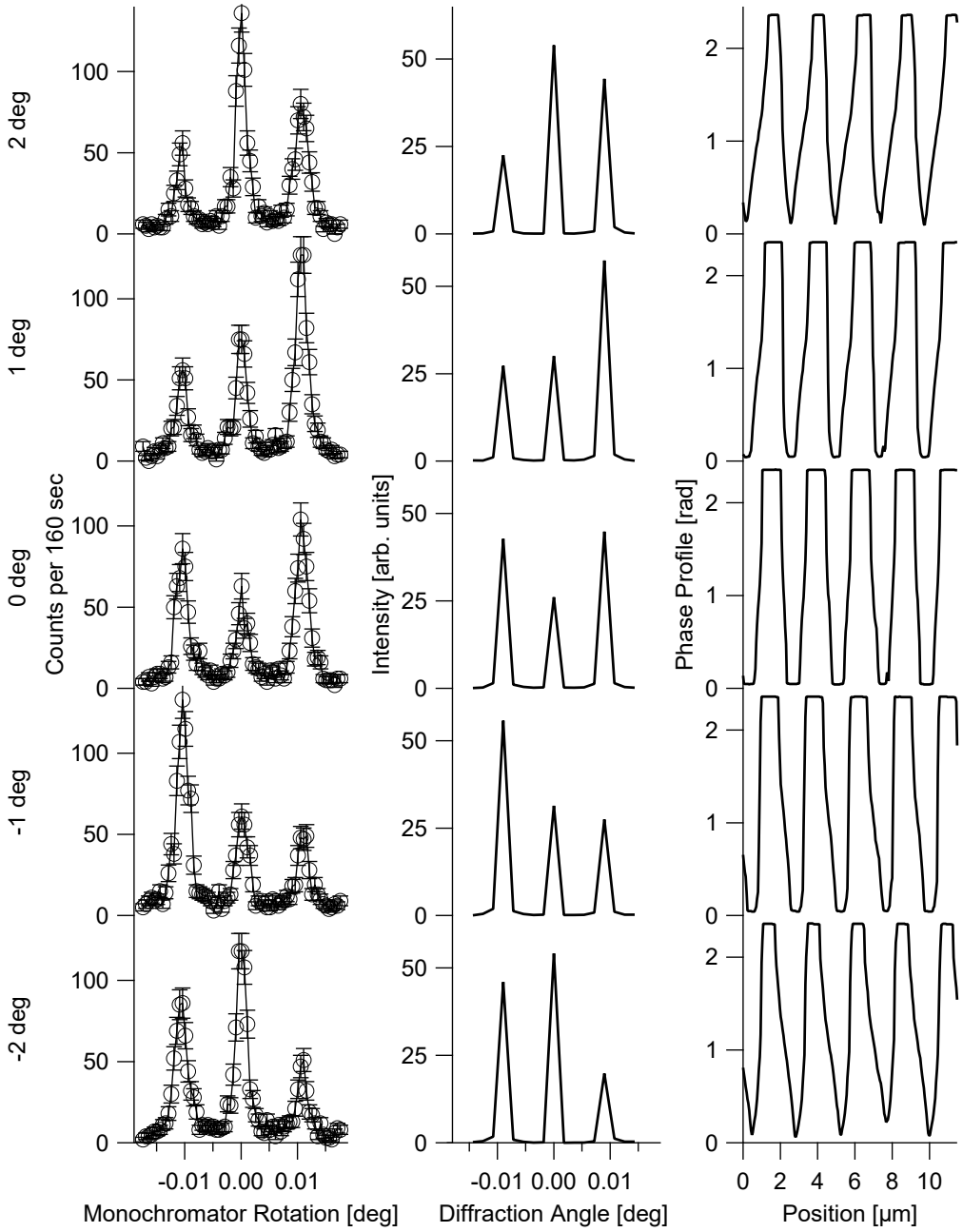

Figure 2.4: The left column of plots is the measured momentum distributions as a function of grating rotation about the y-axis for Grating-1. Grating rotation ranges from -2 degrees to 2 degrees in one degree steps from bottom to top. Uncertainties are purely statistical, and lines connecting data points are shown for clarity. The middle (right) column shows the momentum distributions (phase profiles) computed from the SEM micrographs. Figure taken from Ref. [11].

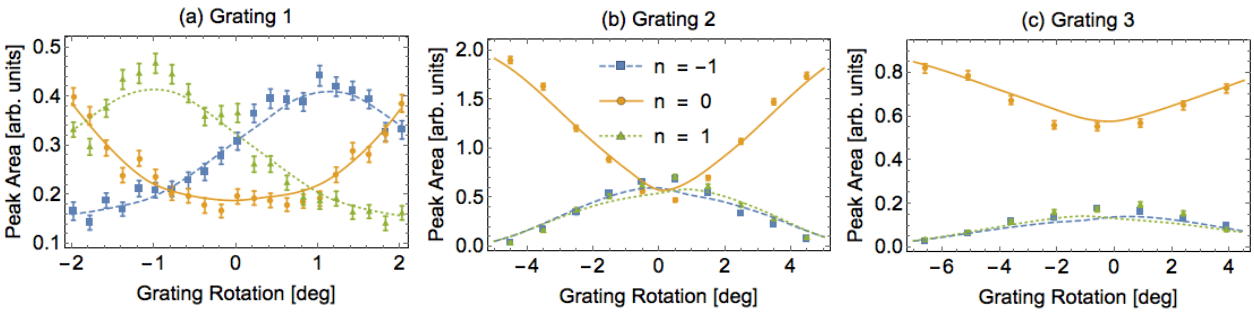

Figure 2.5: Zeroth and first order diffraction peak areas from the measured momentum distributions (data points) and the momentum distributions computed from the SEM transforms (solid lines) as a function of grating rotation about the y-axis for (a) Grating-1, (b) Grating-2, and (c) Grating-3. Uncertainties shown are pure statistical. Figure taken from Ref. [11].

$$\phi(x) = \frac{\phi_0}{2}\mathrm{sgn}\left[\cos\left(\frac{2\pi x}{\lambda_G}\right)\right], \tag{2.7}$$

and the corresponding momentum distributions are shown in Fig. 2.2b for various amplitudes ϕ_0. Note that for a $\phi_0 = \pi$ phase-grating the zeroth diffraction order is suppressed.

To resolve the individual diffraction peaks, the wave packet's coherence length σ must be suitably long compared to the grating period. Figs. 2.2c and 2.2d show $P_f(k_x)$ for various neutron wave packet coherence lengths. (Fig. 2.2c, Fig. 2.2d) shows the case where the neutron wave packet is on axis with a (phase jump, phase step) of the phase-grating. It can be seen that as the coherence lengths of the neutron wave packet becomes much shorter than the period of the grating, the diffraction peaks will no longer be well-defined.

2.2.2 Experimental Methods

The experiment was performed at the NIOFa beamline at the National Institute of Standards and Technology (NIST) Center for Neutron Research (NCNR) in Gaithersburg, MD [4, 5]. See Fig. 1.3 for the beamline's location at the NCNR, and see section 1.4.3 for a description of the NIOFa beamline.

A schematic of the experiment is shown in Fig. 2.3a. A $\lambda = 0.44$ nm neutron beam is extracted from the neutron guide using a pyrolytic graphite (PG) monochromator. The beam is further prepared through Bragg diffraction (Laue geometry) using a perfect-silicon crystal (111) monochromator. To measure the outgoing momentum distribution modified by the phase-grating, we placed a second perfect-silicon crystal (111) analyzer after the grating. The monochromator was rotated relative to the analyzer by a rotation stage with an embedded optical encoder, allowing arcsecond precision motion.

The Bragg diffracted wave packets are Lorentzian in shape in momentum space. Their nominal transverse coherence length is given by the Pendellösung length $\Delta_H = 35$ μm for the (111) reflection from silicon at $\lambda = 0.44$ nm. A cadmium slit is used to collimate the

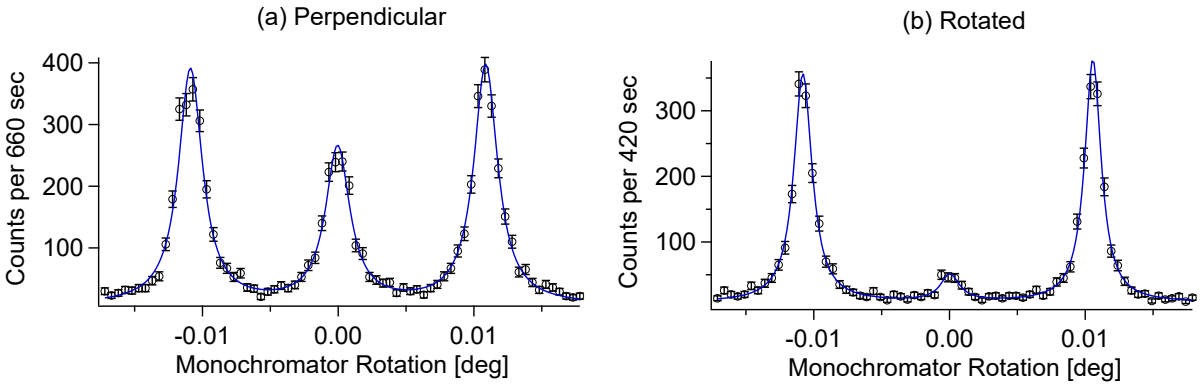

Figure 2.6: Grating-2 measured momentum distributions when (a) perpendicular to the incoming beam and (b) rotated by ~ 40 degrees about the x-axis so that it is approximately a π phase-grating. Uncertainties shown are pure statistical. Lines are fitted Lorentizians. Figure taken from Ref. [11].

transmitted beam. The momentum-space acceptance of the monochromator - analyzer pair add in quadrature; so the observed widths of the measured diffraction peaks constitute an upper bound on the spread in momentum space (and a lower bound on the coherence length) of the incoming wave packet.

Three gratings were analyzed in this experiment. The period of each grating was $\lambda_G = 2.4$ μm. The grating depths were $h = 29.0$ μm, $h = 23.9$ μm, and $h = 15.8$ μm; the corresponding phase amplitudes are (for $\lambda = 0.44$ nm neutrons) 2.6 rad, 2.2 rad, and 1.4 rad, respectively. Scanning Electron Microscope (SEM) micrographs of the three gratings are shown in Fig. 2.3b.

The gratings were first all analyzed separately. Momentum distributions were measured as a function of rotation about three axes (defined in Fig. 2.3a): (1) the axis perpendicular to the neutron propagation and grating diffraction directions ($y-$axis), (2) the axis defined by the grating diffraction direction ($x-$axis), and (3) the propagation beam axis ($z-$axis). In addition, momentum distributions were measured with two gratings separated by 20 cm as a function of rotation about the z-axis.

2.2.3 Rotational Effects on the Resulting Momentum Distribution

Rotations about the y-axis cause the effective grating period to decrease. However, the severe aspect ratio of these gratings causes a change in the phase path integral to be the dominant effect. Integrating over the neutron's trajectory through a phase-grating as a function of rotation about the y-axis modifies the effective phase profile from a nominal square wave. Note that this effect is not as pronounced for very cold neutrons [68], because the phase-gratings used have aspect ratios close to unity.

To quantify this effect, the integrated phase profiles were computed from the SEM micrographs as a function of rotation about the y-axis using silicon's neutron scattering length density of 2.1×10^{-6} Å^{-2}. The momentum distributions were computed by transforming the phase profiles taken from the SEM micrographs according to Eq. 2.2 using a fast Fourier

transform (FFT). The power spectra of the FFT compared to experimental momentum space distributions for Grating-1, along with the effective phase profiles, are shown in Fig. 2.4.

The diffraction peaks were characterized by fitting the measured intensity versus monochromator rotation to multiple Lorentzians. Fig. 2.5 compares the areas of the fitted Lorentzians to the areas of the peaks in the FFT power spectra taken from the grating SEM phase profiles. The computed diffraction peak areas from the SEM were scaled to match the absolute peak areas of the measured distributions with the relative areas between diffraction orders and grating rotations preserved. The asymmetry between the two first-order diffraction peak areas was unique to Grating-1. This effect can be understood by inspecting the phase profiles in Fig 2.4c. As the grating is rotated, the phase profile has an asymmetrical slope. The sign of the slope changes as the grating rotation crosses zero. This unique phase profile is only seen in Grating-1 because of the baseball-bat-shaped grating walls visible in the SEM micrograph Fig. 2.3b.

Due to the high aspect ratio of neutron phase-gratings, the phase profile vanishes as the rotation about the y-axis approaches $\sim \lambda_G/h \sim 5$ degrees. The quality of the grating further diminishes the angular range over which the grating is effective. This can be seen by inspecting the relative peak areas in Fig. 2.5. Because of the distorted walls of Grating-1, the first order peak areas have a large slope as a function of y-axis rotation when the grating is aligned to the beam. This adds a transverse momentum dependence to the diffracted wave amplitudes if the grating is used in a phase-grating NI, which may diminish interferometer contrast. Even for the typical beam divergence of ~ 0.5 degrees, the angular edges of the beam probe drastically different grating profiles. This effect is absent in Grating-2 and Grating-3, where the diffracted peak areas form a maximum when the grating is aligned to the beam.

Rotations about the x-axis only change the effective thickness of the grating, and therefore the phase of the grating changes by

$$\phi(x) \rightarrow \frac{\phi(x)}{\cos\alpha}. \tag{2.8}$$

A 50% comb-fraction grating with a π phase amplitude theoretically has the zeroth-order peak suppressed as shown in Fig. 2.2a. However, the amplitude of the zeroth order peak is proportional to $\cos^2(\phi_0/2)$, hence the peak reappears slowly as a function of grating thickness. Demonstration of the zeroth-order peak suppression is shown in Fig. 2.6 by rotating Grating-2 about the x-axis.

However, the disappearance of the zeroth-order peak does not hold true for a π phase-grating with sloped walls. Thus, if a grating is known to be aligned to the y-axis, as in the previous section, and to be the proper thickness of silicon to be a π phase-grating, the lack of a zeroth order peak is a measure of the squareness of the grating. The almost complete suppression of the zeroth order peak seen in Fig. 2.6b matches the SEM micrograph in Fig. 2.3 in that Grating-2 is of very high quality and closely estimates a square wave.

Grating rotations about the z-axis rotate the diffraction plane of the grating out of the diffraction plane of the monochromator-analyzer pair (the x-z plane in Fig. 2.3a). This can be interpreted as effectively lengthening the grating's period by

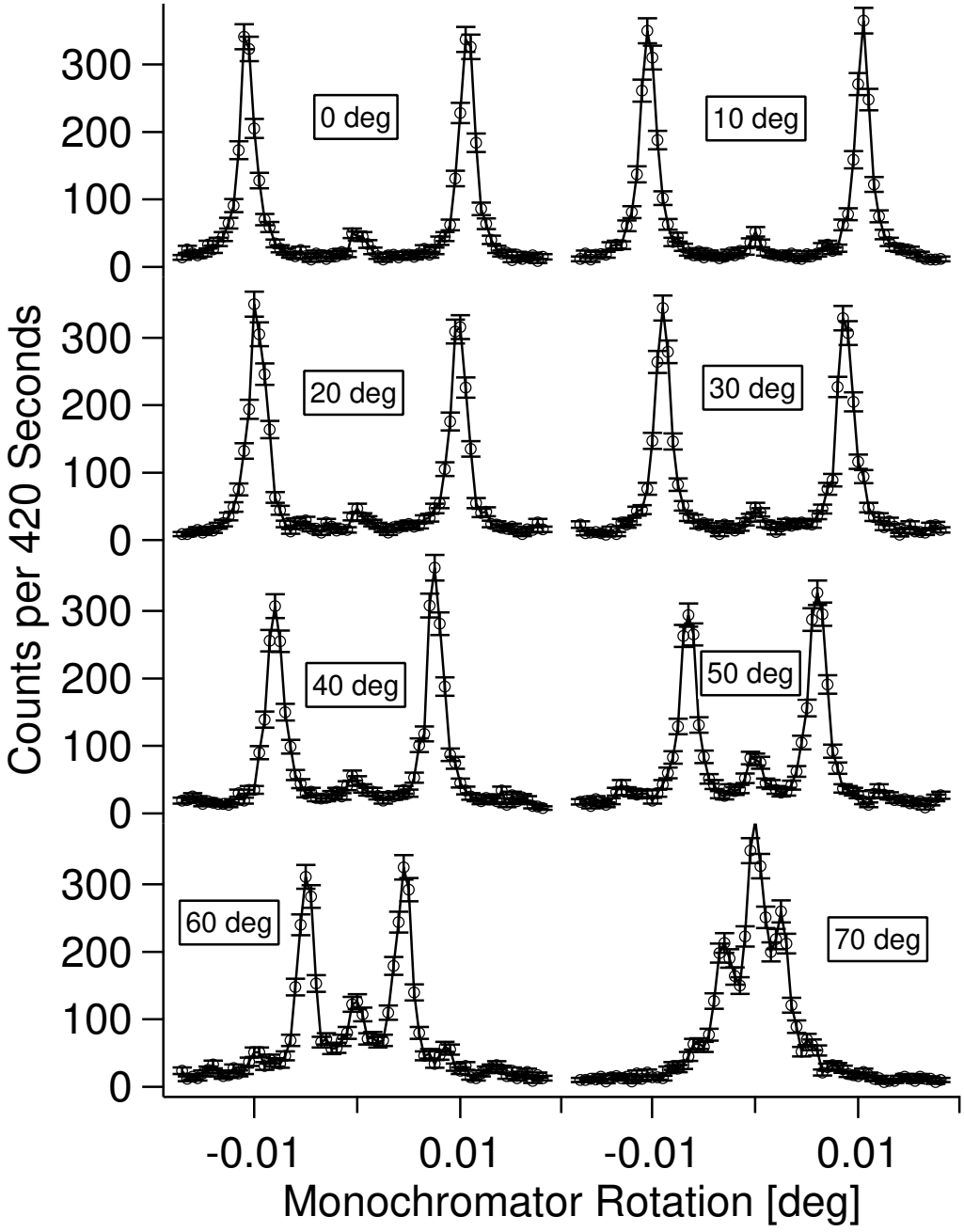

Figure 2.7: Grating-2 diffraction peaks in the $\sim \pi$ orientation as a function of rotation about the z-axis. Uncertainties shown are pure statistical. Lines connecting data points are shown for clarity. Figure taken from Ref. [11].

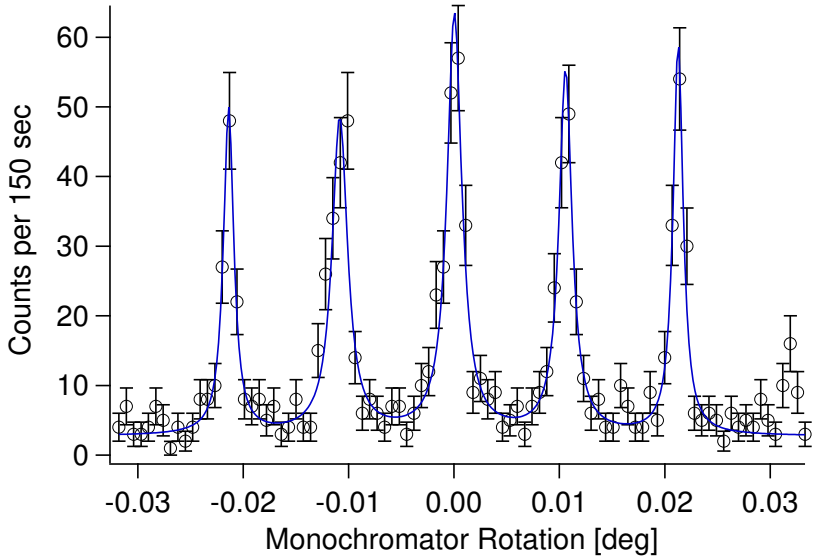

Figure 2.8: Double grating momentum distribution with Grating-1 and Grating-2 and fitted Lorentzians. Each grating was aligned to the beam about the y-axis separately. Uncertainties shown are pure statistical. Figure taken from Ref. [11].

$$\lambda_G \to \frac{\lambda_G}{\cos\gamma}, \tag{2.9}$$

where γ is the angle of elevation between the crystal and grating diffraction planes about the z-axis. Because the momentum distribution is only narrow in the crystal diffraction direction, rotating the grating about the $\hat{z}$ axis reduces the σ/λ_G ratio (see Fig. 2.2d). This causes the measured diffraction peaks to overlap as the grating is rotated as shown in Fig. 2.7.

When two gratings with the same period are used in series, the n-order diffraction peaks from the first grating are diffracted into $n+m$ order peaks, where m is the diffraction order of the second grating. The measured momentum distribution of Grating-1 and Grating-2 operated in series is shown in Fig. 2.8. Second order diffraction peaks now have amplitudes similar to the first and zeroth order peaks.

If one or both of the gratings are rotated about the z-axis, Eqn. 2.6 is modified and the crystal monochromator/analyzer pair will measure peak locations of

$$\theta = \sin^{-1}\left[\frac{\lambda}{\lambda_G}(n\cos\gamma_1 + m\cos\gamma_2)\right] \tag{2.10}$$

for two gratings of the same period λ_G, with γ_1 and γ_2 the z-axis rotation of Grating-1 and Grating-2, respectively. The effect of rotating one grating about the z-axis while leaving the other aligned is shown in Fig. 2.9. The number of observable peaks increases because $n + m\cos\gamma$ need not add to an integer between -2 and 2 for n and m restricted to $\{0, \pm 1\}$. As shown in Fig. 2.9 seven diffraction peaks were resolvable; though up to nine peaks are possible.

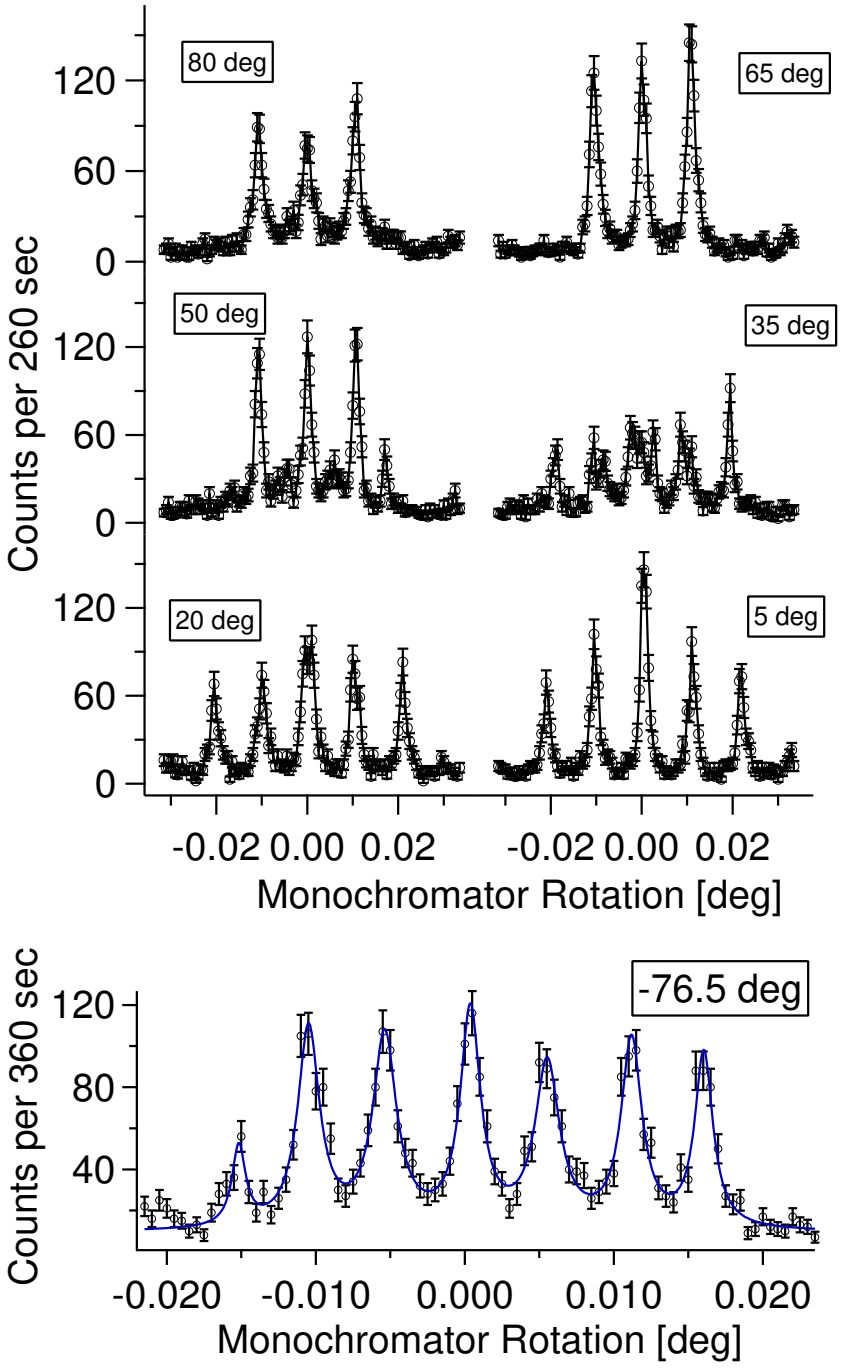

Figure 2.9: Two grating measured momentum distributions with Gratings-1 and -2. Grating-1 is being rotated about the z-axis while Grating-2 was held fixed. Each grating was aligned to the beam about the y-axis separately. Uncertainties shown are pure statistical. In the upper array of plots, lines between data points are shown for clarity. Fitted Lorentzians are shown in the bottom plot. Figure taken from Ref. [11].

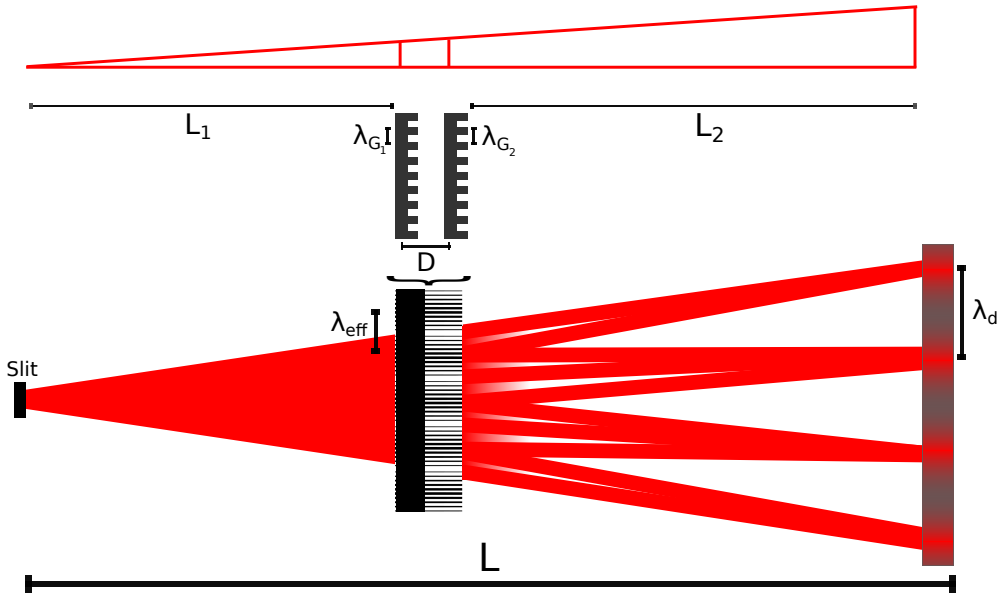

Figure 2.10: Two phase-grating moiré NI operating in the far-field. The setup relies on a modulated phase-grating which resulted from the overlap of two phase-gratings with slightly different periods. With a diverging beam two phase-gratings with identical periods $\lambda_{G_1} = \lambda_{G_2}$ can be used and the distance between them, D, determines the effective period, λ_{eff}. The camera is placed in the far-field to image the intensity formed by the diffraction orders.

2.3 Two Phase-Grating Moiré Interferometer[3]

This section describes the implementation of a two phase-grating moiré neutron interferometer (PGMI) operating in the far-field regime. The demonstration includes the use of a continuous monochromatic beam ($\lambda = 0.44$ nm), a continuous bichromatic beam (1/3 intensity $\lambda_1 = 0.22$ nm and 2/3 intensity $\lambda_2 = 0.44$ nm), a continuous polychromatic beam (approximately given by a Maxwell-Boltzmann distribution with $T_c = 40$ K or $\lambda_c = 0.5$ nm), and a pulsed neutron beam ($\lambda = 0.5$ nm to $\lambda = 3.5$ nm).

2.3.1 Theory

The far-field moiré NI relies on a modulated phase-grating which resulted from the overlap of two phase-gratings with slightly different periods, as shown in Fig. 2.10. With a diverging beam two phase-gratings with identical periods $\lambda_{G_1} = \lambda_{G_2}$ can be used. In the small angle approximation the effective period of the second grating is given by:

$$\lambda'_{G_2} = \frac{\lambda_{G_1}(L_1 + D)}{L_1} \tag{2.11}$$

where L_1 is the distance from the slit to the first phase-grating, and D is the distance from

[3]This section is largely taken from Ref. [12].

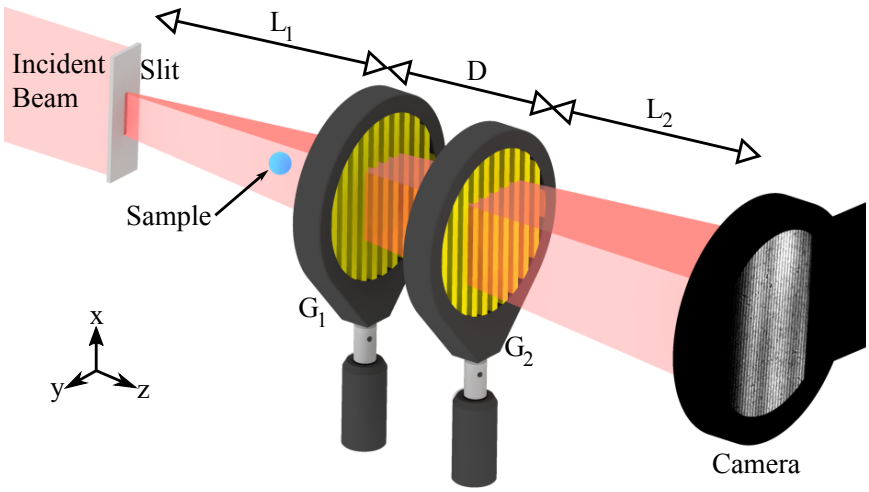

Figure 2.11: Schematic of the two phase-grating interferometer setup. A neutron beam is passed through a narrow slit to define the neutron coherence length along the direction which is perpendicular to the grating fringes. Two identical phase-gratings (G_1 and G_2) are separated by distance D. They are placed at a distance L_1 from the slit and L_2 from the imaging camera. The fringe pattern period at the camera is wavelength independent and the fringe visibility can be optimized with the conditions discussed in the text. A sample to be imaged may be placed before the gratings (upstream position) or after the gratings (downstream position). Figure taken from Ref. [12].

the first to the second phase-grating. The period of modulated phase-grating resulting from the overlap of λ_{G_1} and λ'_{G_2} is given by:

$$\lambda_{eff} = \frac{\lambda_{G_1}\lambda'_{G_2}}{\lambda_{G_1} - \lambda'_{G_2}} = \frac{\lambda_{G_1}(L_1 + D)}{D} \tag{2.12}$$

Finally, the effective period of the modulated phase-grating at the location of the detector is given by:

$$\lambda_d = \frac{L\lambda_{eff}}{(L_1 + D)} = \frac{L\lambda_{G_1}}{D} \tag{2.13}$$

where $L = L_1 + D + L_2$ is the distance between the slit and the camera.

In order for the neutron to diffract from the first grating G_1 at the distance L_1, the neutron's coherence length (along the y-axis in Fig. 2.11), should be at least equal to the

period of the grating. The coherence length is given by Eq. 1.15:

$$\sigma = \frac{\lambda L_1}{s_w} \geqslant \lambda_{\mathrm{G}_1}. \tag{2.14}$$

The second grating G_2 is placed at a distance D from the first grating, and a distance L_2 from the neutron camera. As neutron cameras have limited spatial resolution η, the fringe period λ_d at the camera should be bigger than neutron camera resolution:

$$\lambda_d = \frac{L\lambda_{\mathrm{G}_1}}{D} > \eta, \tag{2.15}$$

Similarly the fringe oscillations on the detector are a periodic function of the slit location, with the period (often called source period) given by:

$$\lambda_s = \frac{L\lambda_{\mathrm{G}_1}}{D}. \tag{2.16}$$

Therefore, in order to observe a fringe pattern on the detector the slit width should be smaller than the source period, i.e. $\lambda_s < s_w$.

To verify that we are indeed in a far-field regime we consider the Fraunhofer distance when the coherence length is used as the source dimension:

$$d_F = 2\frac{\sigma^2}{\lambda} = 2\lambda\Big(\frac{L_1}{s_w}\Big)^2. \tag{2.17}$$

We consider the coherence length because it is always equal or greater than the grating period in the setup. To satisfy the far-field regime L_2 should be greater than the Fraunhofer distance:

$$\frac{d_F}{L_2} \approx \frac{\lambda L}{s_w^2} \ll 1. \tag{2.18}$$

Given the experimental parameters of the monochromatic beamline $d_F/L_2 \approx 0.04$, polychromatic beamline $d_F/L_2 \approx 0.02$ for $\lambda = 0.5$ nm, and the beamline at the pulsed source $d_F/L_2 \approx 0.08$ for $\lambda = 0.35$ nm. The other two conditions for far-field regime are:

$$L_2 \gg \lambda, \quad L_2 \gg s_w. \tag{2.19}$$

In our cases they are the least strict conditions.

The intensity at the camera must be computed numerically by propagating the neutron wave function into the far-field. The intensity is then fit to a cosine curve to obtain the contrast. It has been shown [65] that for equal period $\lambda_{\mathrm{G}_1} = \lambda_{\mathrm{G}_2} \equiv \lambda_G$, $\pi/2$-phase-gratings, with 50% comb fraction, the maximum contrast is optimized for the condition $\delta_1(\lambda) = \delta_2(\lambda) = 0.5$, where:

$$\delta_1(\lambda) = \frac{\lambda L_1 D}{L\lambda_G^2}, \quad \delta_2(\lambda) = \frac{\lambda L_2 D}{L\lambda_G^2}. \tag{2.20}$$

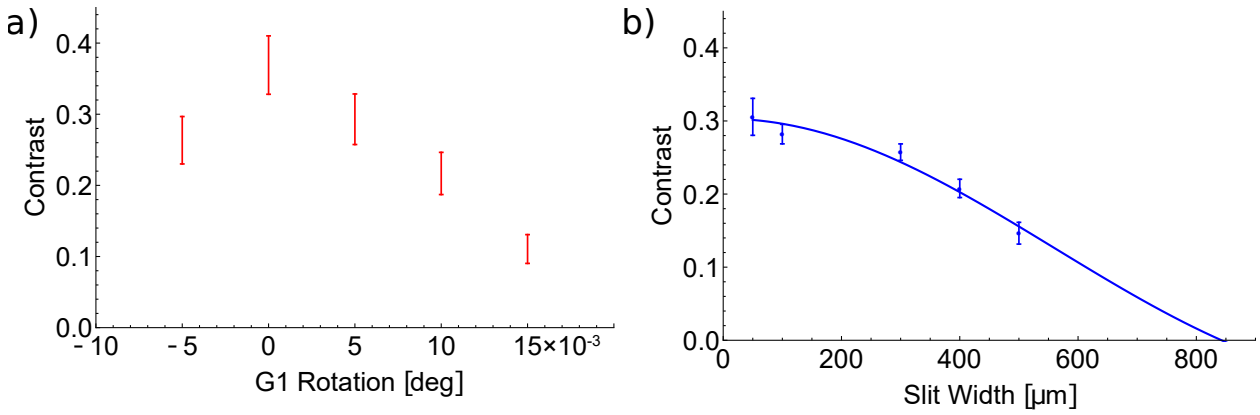

Figure 2.12: Optimization data. a) The contrast is found by placing the gratings vertically and rotating one of them along the roll axis in very fine increments. The plot shows the contrast at the monochromatic beamline as a function of the first grating rotation around the neutron propagation axis. b) The dependence of the contrast at the bichromatic setup on the slit width s_w. The fit is given by applying Eqn. 2.23 to the data, and shows good agreement with the calculated source period P_s. Figure taken from Ref. [12].

The experimental setup, shown in Fig. 2.11, consists of a slit, two identical linear phase-gratings of silicon combs with a period of $\lambda_{G_1} = \lambda_{G_2} = 2.4$ μm, and a neutron imaging detector (neutron camera). To align the gratings the setup is initially arranged with theoretically calculated optimal slit width and lengths L_1, D, and L_2. Then one of the gratings is rotated around the neutron propagation axis ($\hat{z}$ axis) until the fringe pattern is observed at the camera. The contrast with the monochromatic setup as a function of the first grating rotation around the $\hat{z}$ axis is shown in in Fig. 2.12a.

The slit height s_h (slit length along the x-axis direction in Fig. 2.11) can be larger than the slit width s_w in order to increase neutron intensity, provided that the gratings are well aligned to be parallel to that direction. The angular range of appreciable contrast is inversely related to the slit height $\lambda_G/(2L_1 s_h/L)$. The expected range of $\pm 0.007^\circ$ agrees with the range depicted on Fig. 2.12a.

The intensity of the fringe pattern recorded by the camera can be fit to a cosine function

$$I = A + B\cos(2\pi f x + \phi), \tag{2.21}$$

where x is the pixel location on the camera. Thus the mean A, the amplitude B, the frequency f, and the differential phase ϕ can be extracted from the fit. The *contrast* or *fringe visibility* is given by :

$$\mathcal{C} = \frac{\max\{I\} - \min\{I\}}{\max\{I\} + \min\{I\}} = \frac{B}{A}. \tag{2.22}$$

Due to the generally low neutron flux of monochromatic beamlines, the slit widths are optimized for intensity vs contrast. The contrast as a function of the slit width for the bichromatic setup is shown in Fig. 2.12b. Variation of the contrast vs. slit width could be

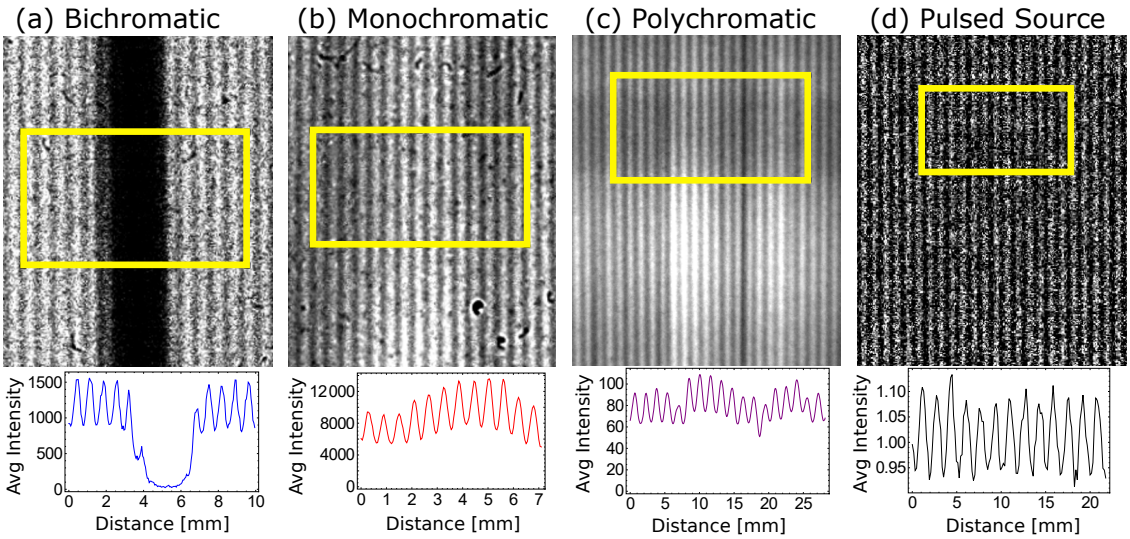

Figure 2.13: Typical far-field images obtained with (a) 300 s exposure time with the bichromatic neutron beam (b) 10000 s exposure time with the monochromatic neutron beam, (c) median filter applied on three images with 2 s exposure time with the polychromatic neutron beam (d) normalized image from the J-PARC pulsed source. The integrated intensities of the regions specified by the yellow rectangle show the observed fringe pattern at the camera. The dark region in the middle of the bichromatic image is due to the collimator in that particular setup and not due to the gratings. Figure taken from Ref. [12].

described by the sinc function:

$$\mathcal{C} = \mathcal{C}_0 \left| \mathrm{sinc} \left[\frac{\pi s}{\lambda_s} \right] \right|. \tag{2.23}$$

where $\mathcal{C}_0$ is the maximum achievable contrast with a given setup. Thus, given a slit width of one third of the source period, in our case 281 μm, would give an upper bound of 83% contrast. The fit in Fig. 2.12b gives a source period of $\lambda_s = 843 \pm 43$ μm, which is in good agreement with $\lambda_s = 845$ μm obtained with Eq. 2.16 where $D = 10$ mm.

2.3.2 Experimental Methods

Although $\pi/2$-phase-gratings for a specific neutron wavelength give optimal fringe visibility, available to us were five different gratings with various depths. We had used gratings corresponding to 0.27π phase shift at 0.44 nm wavelength for the mono- and bi-chromatic setups and 0.2π phase shift at 0.5 nm wavelength for the polychromatic setup.

The experiment was performed in four different configurations. The bichromatic and monochromatic beam configurations were performed at the NG7 NIOFa beamline [4] at the National Institute of Standards and Technology Center for Neutron Research (NCNR) with $L_1 = 1.73$ m and $L = 3.52$ m for bichromatic beam and $L_1 = 1.20$ m and $L = 2.99$ m for monochromatic beam. See Fig. 1.3 for the beamline's location at the NCNR, and see section 1.4.3 for a description of the NIOFa beamline. The neutron camera used in this

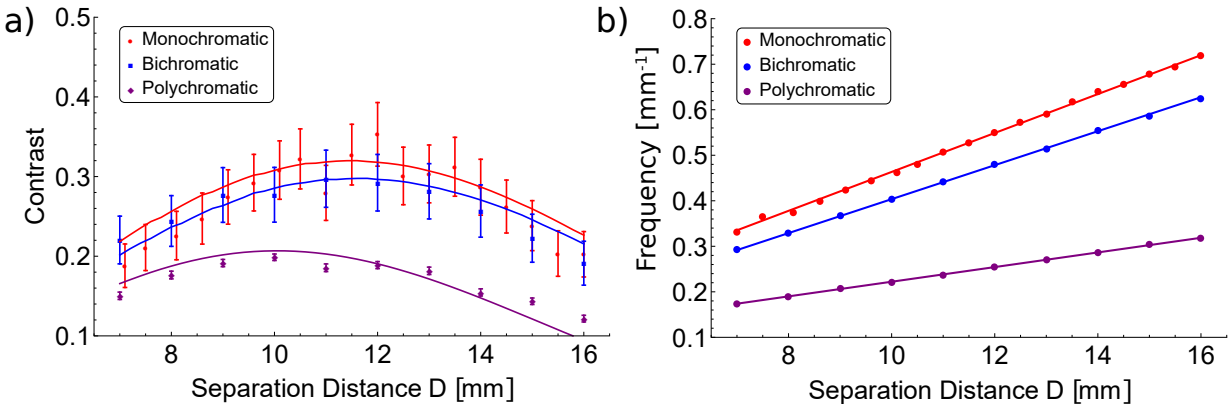

Figure 2.14: a) The contrast as a function of the separation distance between the gratings for the monochromatic, bichromatic, and polychromatic neutron beams. The fits are given by Eq.12 in [65], and the contrast for the monochromatic, bichromatic and polychromatic beamlines is optimized at $D = 12$ mm, 12 mm, and 10 mm respectively, agreeing well with theoretical predictions [65]. b) The frequency of the oscillation fringes varies linearly as a function of the distance between the gratings. The linear fit is according to $(D - D_0)/(L\lambda_G)$ which for the monochromatic setup gives $D_0 = -0.75$ mm and $L = 3.04$ m, the bichromatic setup gives $D_0 = -0.8$ mm and $L = 3.51$ m, and polychromatic setup gives $D_0 = -3.8$ mm and $L = 8.36$ m. The exposure time was 2 s. Figure taken from Ref. [12].

setup has an active area of 25 mm diameter, with scintillator NE426 (ZnS(Ag) type with ^{6}Li as neutron converter material) and a spatial resolution of ~ 100 μm, and virtually no dark current noise [69]. Images were collected in 300 s long exposures. The neutron quantum efficiency of the camera is 18% for $\lambda = 0.22$ nm and about 50% for $\lambda = 0.44$ nm. The neutron beam is extracted from a cold neutron guide by a pyrolytic graphite (PG) monochromator with $\lambda = 0.44$ nm and $\lambda = 0.22$ nm components with an approximate ratio of 3.2:1 in intensity. To change from bichromatic to monochromatic configuration, i.e. filter out the $\lambda = 0.22$ nm component, a liquid nitrogen cooled Be-filter with nearly 100% filter efficiency [4] was installed downstream of the interferometer entrance slit. The slit width was set to 200 μm and slit height to 2.5 cm.

The polychromatic beam configuration was performed at the NG6 Cold Neutron Imaging (CNI) facility [70] at the NCNR. See Fig. 1.3 for the beamline's location at the NCNR. The CNI is located on the NG6 end-station and has neutron spectrum approximately given by a Maxwell-Boltzmann distribution with $T_c = 40$ K or $\lambda_c = 0.5$ nm. The slit to detector length is $L = 8.8$ m and slit to G_1 distance is $L_1 = 4.65$ m. The slit width was set to 500 μm and slit height to 1.5 cm.

The imaging detector was an Andor sCMOS NEO camera viewing a 150 μm thick LiF:ZnS scintillator with a Nikon 85 mm lens with a PK12 extension tube for a reproduction ratio of about 3.7, yielding a spatial resolution of $\eta = 150$ μm. To reduce noise in the sCMOS system, the median of three images were used for analysis.

The fourth configuration used a pulsed neutron beam produced at the Energy-Resolved Neutron Imaging System (RADEN) [71], located at beam line BL22 of the Japan Proton Accelerator Research Complex (J-PARC) Materials and Life Science Experimental Facility

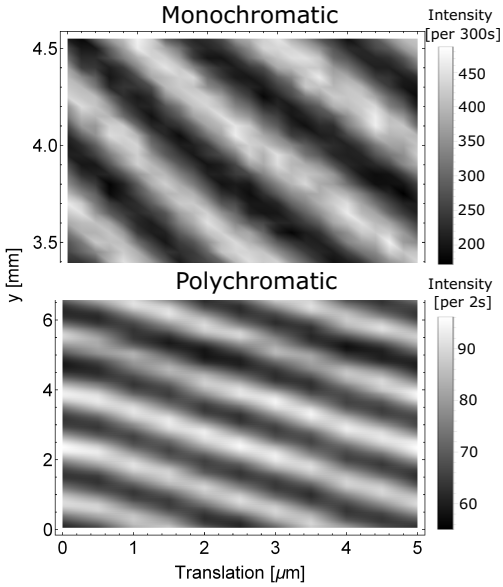

Figure 2.15: Linear phase stepping is achieved with parallel translation of the first grating G_1 by increments smaller than the period of the gratings. (Top) Data from the monochromatic beamline (Bottom) Data from the polychromatic beamline. In both cases linear dependence between the phase and grating translation is observed, while the contrast is preserved. Data was collected for the translation range of 0 μm to 5 μm, in increments of 0.2 μm (0.5 μm) for monochromatic (polychromatic) plot. Figure taken from Ref. [12].

(MLF). The wavelength range that was used was from 0.05 nm to 0.35 nm. The slit to detector length is $L = 8.6$ m and slit to G_1 distance is $L_1 = 4.24$ m. The slit width was set to 200 μm and slit height to 4 cm. The neutron imaging system employed a micro-pixel chamber (μPIC), a type of micro-pattern gaseous detector with a two-dimensional strip readout, coupled with an all-digital, high-speed FPGA-based data acquisition system [72]. This event-type detector records the time-of-arrival of each neutron event relative to the pulse start time for precise measurement of neutron energy, and it has a spatial resolution of 280 μm (FWHM). The readout of the μPIC detector introduces a fixed-pattern noise structure which is completely removed by normalizing to empty beam measurements. Thus, the visibility measurements are from open-beam normalized images of the moiré pattern. The average number of detected neutron events was about 80 per 160 micron pixel with a 4 h integration time.

2.3.3 Results and Discussion

By observing the interference fringes with and without a sample that has been placed either upstream or downstream of the gratings we can extract the conventional beam attenuation, dark-field contrast, and differential phase contrast. By varying the grating spacing D, this interferometer may also be employed to measure small angle scattering of microstructures in the range of nm to several μm, as described in section 2.2.

Fig. 2.13 (a)-(d) show examples of typical images of the interference pattern obtained in optimized configurations for different beamlines: (a) bichromatic beam with $\lambda_1 = 0.22$ nm

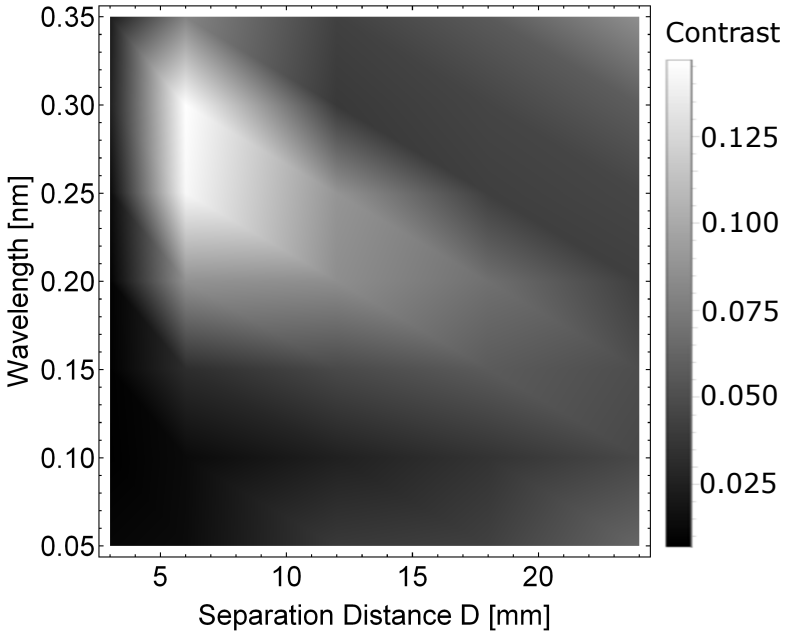

Figure 2.16: Grayscale representation of the contrast (fringe visibility) dependence on neutron wavelength and gratings separation distance, D. Contrast data obtained with a pulsed neutron beam from a spallation source at J-PARC. Data was collected for the wavelength range of 0.05 nm to 0.35 nm, in increments of 0.05 nm; and for separation distance values of 3 mm, 6 mm, 12 mm, 18 mm, and 24 mm. Figure taken from Ref. [12].

and $\lambda_2 = 0.44$ nm (b) same beamline as (a) but with a Be-filter to completely eliminate the $\lambda_1 = 0.22$ nm component (c) polychromatic neutron beam with peak wavelength $\lambda_c = 0.5$ nm and (d) a pulsed source for $\lambda = 0.25$ nm. In Fig. 2.13 (a) the middle dark region corresponds to the collimator which was placed at the front in the setup, and not the grating pattern. As the Be-filter adds divergence to the beam it can be seen that the dark middle region gets washed out in Fig. 2.13 (b). The box on each image represents a region of integration along the vertical axis and the integral curve is shown under each image. Such integral curves were used to fit with Eq. [2.21] to extract phase, frequency, and compute the contrast via Eq. [2.22].

Fig. 2.14a shows contrast (fringe visibility) change versus grating separation, D. The data obtained at NIST for the monochromatic, bichromatic and polychromatic beamlines is plotted on the same figure for comparison. The theoretically calculated contrast curves for the three conditions are also plotted, which were based on estimates of 0.27π phase shift gratings at 0.44 nm wavelength for the mono- and bi-chromatic setups and 0.2π phase shift at 0.5 nm wavelength for the polychromatic setup. The maximum contrast for the monochromatic, bichromatic and polychromatic beamlines are achieved at $D = 12$ mm, 12 mm, and 10 mm respectively, agreeing well with theoretical predictions. Theoretical estimates indicate that there is room for improvement of contrast by improving grating profile and detector resolution. Fig. 2.14b shows the linear dependence of the fringe frequency at the camera on the grating separation. As the distance between the gratings is increased the period of the fringes at the camera is decreased. The linear fit is according to $(D-D_0)/(L\lambda_G)$

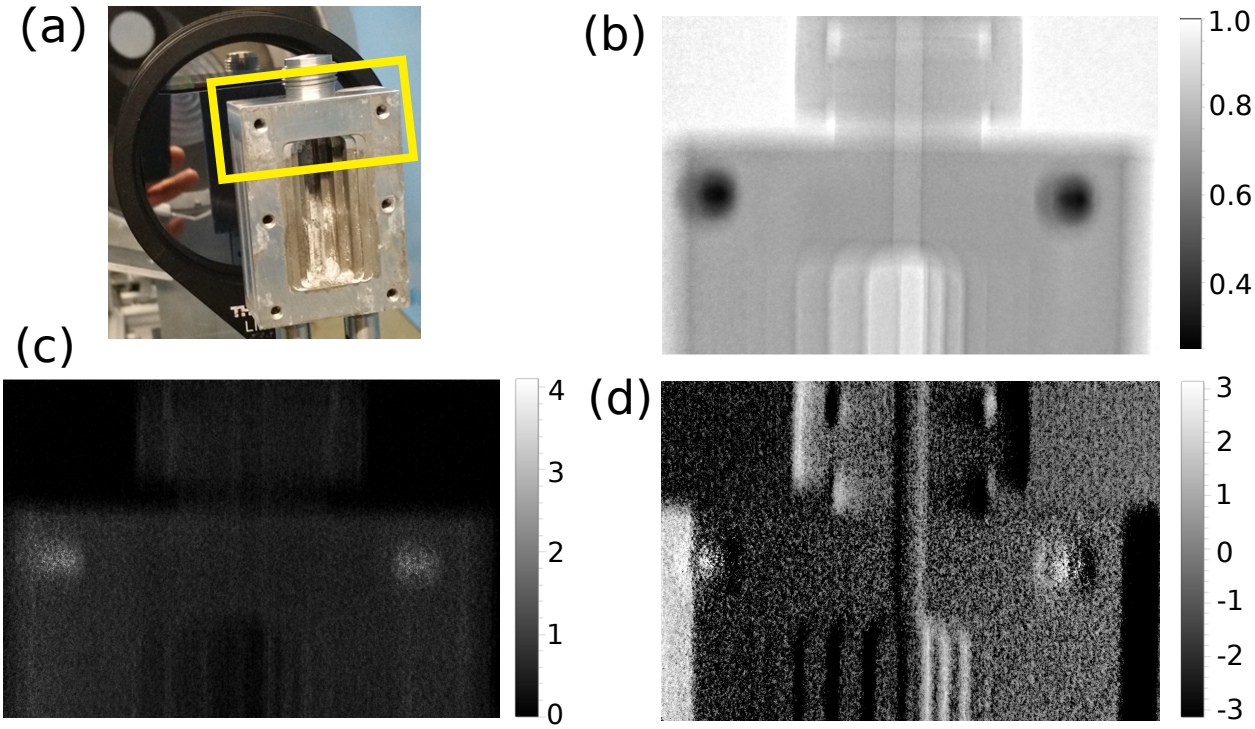

Figure 2.17: Phase-contrast imaging with a polychromatic beam (a) The aluminum sample in front of the G_1 grating. The yellow box roughly outlines what is being imaged. The sample has a step profile in the middle region and threaded screw holes in the corners. (b) Neutron attenuation image due to absorption and scattering. Grayscale bar represents transmission through the sample. (c) Spatial variation of the contrast attenuation due to the sample, $-\log(\mathcal{C}_{\text{sample}}/\mathcal{C}_{\text{empty}})$. In this case white represents a loss in contrast and black represents no loss in contrast. (d) Phase shift in the moiré pattern at the detector due to the sample. Grayscale bar represents radians. Here, the white and black patterns represent the highest phase gradient that the neutrons acquire when passing through the sample. Figure taken from Ref. [12].

which for the monochromatic setup gives $D_0 = -0.75$ mm and $L = 3.04$ m, the bichromatic setup gives $D_0 = -0.8$ mm and $L = 3.51$ m, and polychromatic setup gives $D_0 = -3.8$ mm and $L = 8.36$ m.

To implement phase stepping of the fringe pattern at the camera one grating needs to be translated in-plane in the perpendicular direction to the grating lines (along the y-axis in Fig. 2.11 or along the grating vector). The translation step size needs to be smaller than the grating period. The top plot in Fig. 2.15 shows the two-dimensional plot of phase stepping for the monochromatic beamline setup; and the bottom plot in Fig. 2.15 shows the phase stepping for the polychromatic beamline setup. In both cases linear dependence between the phase and grating translation is observed, while the contrast is preserved.

Similar aligning procedures and measurements were performed at J-PARC spallation pulsed source. Fig. 2.16 shows the contrast as a function of the wavelength for various grating separations. Due to the nature of the pulse source we were able to extract contrast as a function of wavelength. Note that at the time of the experiments J-PARC was running

at 200 KW as opposed to 1 MW due to technical problems. This lowered the neutron flux to 1/5 of the standard flux and the low intensity proved to be a significant challenge in terms of optimizing the setup for each independent wavelength.

The beam attenuation, decoherence, and phase gradient images shown in Fig. 2.17 (b)-(d) are of an aluminum sample shown in Fig. 2.17 (a). The approximate imaged area is depicted by the rectangular box. The images in Fig. 2.17 (b)-(d) were obtained by the Fourier transform method described in [73]. At the described polychromatic beamline at NIST three images with 20 s exposure time were taken at each step in the phase-stepping method [74]. A median filter was then applied to every set of three images. The phase step size was 0.24 μm ranging from 0 to 2.4 μm of the G_2 transverse translation. The G_1 - G_2 grating separation was $D = 11.5$ mm.

Fig. 2.17 (b) shows the conventional attenuation-contrast radiography of the sample, where white color represents full transmission (no attenuation). The shape and features of the sample are well defined in the image. Fig. 2.17 (c) shows the decoherence of the fringe contrast due to the sample, $-\log(\mathcal{C}_{\text{sample}}/\mathcal{C}_{\text{empty}})$, where the white color represents loss of contrast and the black color represent no contrast reduction. As expected the areas which caused the largest attenuation also caused the largest loss of contrast. Fig. 2.17 (d) shows the phase shift in the moiré pattern at the detector due to the sample. The white and black patterns represent highest phase gradient that the neutrons acquire when passing through the sample.

2.4 Measuring the Microstructure of Samples with the Far-Field Interferometer[4]

This section describes the demonstration that a neutron far-field interferometer can be employed to measure the microstructure of a sample. The autocorrelation length of the two phase-grating moiré neutron interferometer, and hence the microstructure length scale that is probed, is proportional to the grating spacing and the neutron wavelength, and can be varied over several orders of magnitude for one pair of gratings. The potential advantages of a far-field neutron interferometer include high contrast with a polychromatic beam (over 30%), no requirement for an absorbing grating to resolve the interference fringes, and the ability to measure the microstructure in the length scale range of 100 nm to 10 μm by varying either the grating spacing or neutron wavelength with a broad wavelength range and single set of gratings.

Neutrons probe matter primarily via the strong nuclear force and thus provide a complimentary measure of the composition of a sample to electromagnetic probes such as x-rays. The interaction with the nucleus also provides a means for isotopic sensitivity, for instance allowing one to create contrast matched solutions composed of heavy and light water. In conventional attenuation based neutron radiography, one measures the local areal density (Nt) from σNt, where σ is the total scattering cross section with typical values of 10^{-24} cm^2 (~ 1 barn), N is the number density and t is the path length through the material. In neutron phase imaging, one measures a phase shift of the wavefront which is proportional

[4]This section is largely taken from Ref. [13]. The lead author was Daniel Hussey.

to the local areal density from $b_c\lambda Nt$, where b_c is the coherent scattering length ($\sim 10^{-13}$ cm) and λ is the neutron wavelength ($\sim 10^{-8}$ cm). Thus if the measurements have similar counting statistics and other uncertainties, neutron phase imaging would be ∼1000 times more sensitive to variations in the areal density of an object. If there are fluctuations in the scattering length density (Nb_c) due to a non-uniform microstructure, one observes small angle scattering (SAS). In interferometric phase imaging measurements, SAS results in a reduction of the contrast of the interference pattern [75–78].

Talbot-Lau interferometer (TLI) has been used to measure the pair-correlation function of samples. The auto-correlation length of the TLI is linear in the separation of the detector and sample position. In order to scan through a range of auto-correlation lengths, the sample-detector separation needs to be varied, which loses the inherent spatial registration over the measurements. As well, to probe smaller auto-correlation lengths (<1 μm) requires small ($\sim$ 1 cm) separation between detector and sample so that the auto-correlation length will vary through an object prohibiting these methods from obtaining tomographic (3D) reconstructions. Recently spin echo modulated small angle neutron scattering (SEMSANS) has been demonstrated to provide a quantitative measure of the pair-correlation function [79]. Such a system allows one to scan the auto-correlation length through scanning the neutron wavelength and differences between two magnetic field regions to cover a broad range of auto-correlation lengths. Similar to the TLI, the method also places the sample in close proximity ($\sim$ 1 cm) to the detector so that the auto-correlation length will vary through a sample of finite thickness. As well, the method requires neutron spin polarization and analysis, which in practice reduces the intensity by an order of magnitude from the incident intensity.

The diffraction angle due to a sample with periodicity λ_s is given by:

$$\theta \sim \pm\frac{\lambda}{\lambda_s} = \pm\frac{q\lambda}{2\pi} = \pm\frac{y_0}{L_s}, \tag{2.24}$$

where q is the Q-vector, L_s is the distance between the sample and the detector, and y_0 is the displacement at the detector which corresponds to a phase shift in the fringe pattern:

$$\phi_0 = \pm\frac{2\pi y_0}{\lambda_d} = \pm\frac{\lambda L_s}{\lambda_d}q = \pm\zeta q, \tag{2.25}$$

where ζ is commonly referred to as the autocorrelation length of the PGMI. Taking $L_s \sim L/2$ (placing the sample near the gratings):

$$\zeta = \frac{\lambda L_s}{\lambda_d} = \frac{\lambda L_s D}{\lambda_G L} = \frac{\lambda D}{2\lambda_G}, \tag{2.26}$$

In the presented work, the grating separation D was the primary means of varying ζ, with D ranging from about 3.5 mm to 40 mm.

As the sample simultaneously induces a positive and a negative phase shift the contrast at the camera reduces. The greatest reduction in contrast typically occurs for $\phi_0 = \pi$, which

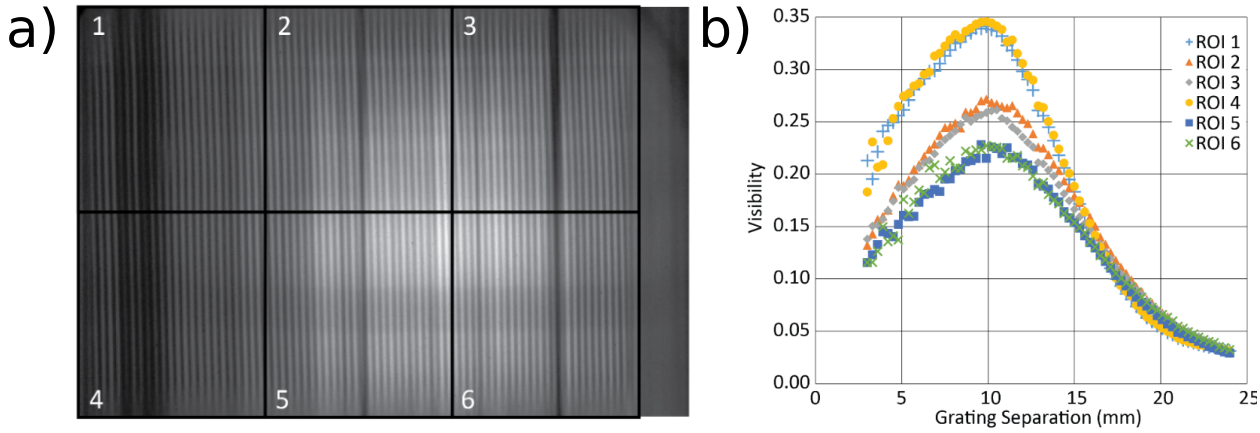

Figure 2.18: Empty interferometer visibility. (a) The raw moiré pattern for 10 mm grating separation. (b) The visibility of the moiré pattern as a function of grating separation for the 6 regions of interest indicated in (a). The spatial resolution of the detector was 0.25 mm and limited the range of the visibility measurements in this case. Figure taken from Ref. [13].

corresponds to:

$$q \sim \frac{2\pi\lambda_G}{D\lambda}. \tag{2.27}$$

Hence the PGMI is sensitive to a specific inverse length scale within the sample.

By measuring the contrast reduction, μ_d at different autocorrelation lengths of the interferometer, ζ, one measures the pair-correlation function $G(\zeta)$ [78]:

$$e^{-\mu_d(\zeta)t} = \frac{C_{sample}(\zeta)}{C_{empty}(\zeta)} = e^{-\int_{\text{path}} \Sigma[1-G(\zeta)]dt} \sim e^{-\Sigma t[1-G(\zeta)]} \tag{2.28}$$

where t is the thickness of the sample, Σ is macroscopic scattering cross section, and the rightmost relation holds for homogeneous samples. For a monodisperse solution of spheres [78]:

$$\Sigma = \frac{3}{2}\phi_v \Delta\rho^2 \lambda^2 r. \tag{2.29}$$

where ϕ_v is the sphere volume fraction, r is the radius, and $\Delta\rho = \rho_{\text{particle}} - \rho_{\text{solvent}}$ is the difference between the scattering length densities of the spheres and the water.

2.4.1 Experimental Methods

The experiments were conducted at the cold neutron imaging (CNI) instrument on the neutron guide 6 (NG-6) at the NIST Center for Neutron Research (NCNR) [70]. See Fig. 1.3 for the beamline's location at the NCNR. The instrument flight path enabled an overall length of L = 8.44 m, L_2= 4.24 m, and L_1= 4.20 m. A vertical slit of 0.5 mm width masked

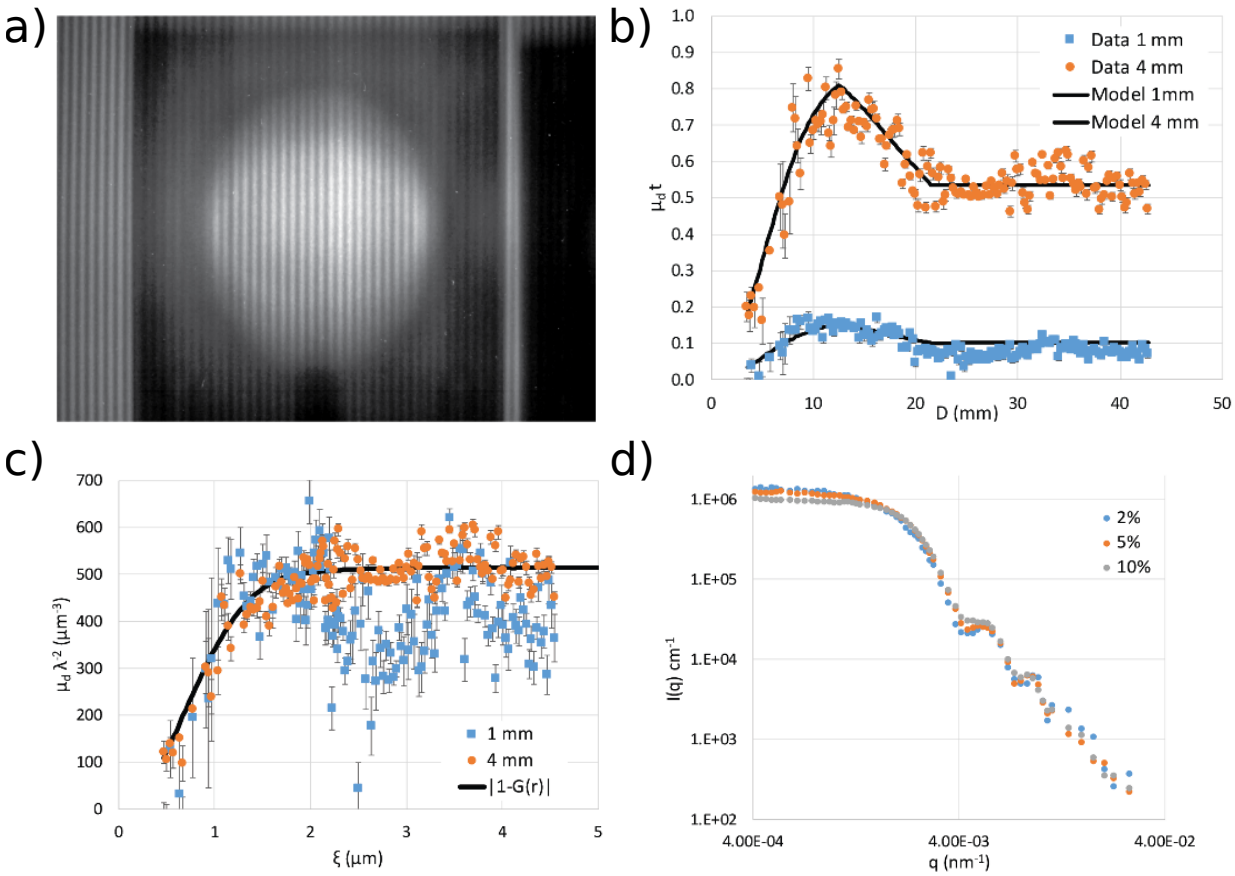

Figure 2.19: Scattering data from a dilute, monodisperse suspension of polystyrene spheres. (a) Raw image of the 1 mm thick polystyrene sample at a grating separation of 13.5 mm. (b) Measured visibility reduction as a function of grating spacing. The uncertainty bars are derived from the one standard deviation of measured fringe visibility reduction over the imaged area of the cuvette. As such, the actual uncertainty is likely larger due to other systematic measurement uncertainties that have yet to be fully quantified. The solid lines are a model assuming a dilute mixture of spheres, and the mean of the wavelength distribution changes linearly between two grating separations, which were determined from a non-linear least squares fit. Note that measurements with a monochromatic beam would not suffer from this systematic effect. (c) Using the lambda ramp function, $\mu_d \lambda^{-2}$ is plotted vs calculated pair-wise auto-correlation $|1 - G(\zeta)|$ for a dilute suspension of spheres. The data show an oscillation, indicating that clustering (short-range order) of the spheres or multiple scattering is being observed. This might also indicate that the correction for the change in wavelength needs to be improved. (d) USANS measurements of three volume fractions of spheres, from which the diameter was measured; the oscillations are due to the monodispersity of the spheres. Figures taken from Ref. [13].

the beam at the entrance; thus the transverse coherence length for a neutron wavelength of 0.5 nm was about 4 μm. Two silicon phase-gratings of 2.4 μm period were used. Grating trenches were oriented vertically to avoid gravitational effects. The first grating was held fixed, while the second grating could be manipulated in pitch, roll, yaw, and longitudinal separation. The mounting scheme was such that the closest approach of the two gratings was about 3 mm.

The data in Fig. 2.18 was obtained with an amorphous silicon detector in direct contact with a 300 μm thick LiF:ZnS scintillator screen. The spatial resolution of this system is about 250 μm, and 100 exposures of 1 s were averaged. The data in Fig. 2.19 were obtained with an Andor sCMOS NEO camera viewing a 150 μm thick LiF:ZnS scintillator with a Nikon 85 mm lens with a PK12 extension tube for a reproduction ratio of about 3.7, yielding a spatial resolution of about 150 μm. To reduce noise in the sCMOS system, the median of three images with 20 s exposure time were used for analysis.

The wavelength distribution of the imaging instrument at NG-6 has not yet been measured. The simulated wavelength distribution can be approximated by a Maxwell-Boltzmann distribution with temperature 40 K giving a peak neutron wavelength of about 0.5 nm. While the far-field interferometer is achromatic, the visibility is maximized for wavelengths which experience a $\pi/2$ phase shift. To provide a $\pi/2$-phase shift for neutrons with a 0.5 nm wavelength, the grating depth in silicon should be 15.1 μm. However, there were 5 available gratings for the experiment, of varying depths, all with period of 2.4 μm and etched with a Bosch process. The gratings were fabricated at the NIST Nanofabrication facility. We measured the visibility obtainable with three combinations of G_1 and G_2 after aligning the relative roll between G_1 and G_2 and scanned their relative separation. Since the gratings employed in this experiment were not optimized for this spectrum, it is possible that higher visibility could be obtained.

The raw images were converted to attenuation, phase gradient, and fringe visibility images using a Fourier transform method that requires a reference image with no sample and a single structured image of the sample. Note that without phase stepping data the algorithm demodulates the images so that the pixel pitch of the reconstructed images is that of the fringe spacing; with phase stepping data, the reconstructed data have the same pixel pitch as the input data. In this work, only the attenuation and visibility images were analyzed.

By scanning either (or both) the inter-grating spacing or the wavelength one obtains a measure of the pairwise auto-correlation function $G(\zeta)$. For the geometry of the present setup, the q-ranges from 10^{-2} nm^{-1} to 10^{-4} nm^{-1}. It would be feasible to approach higher q-ranges with either larger period gratings or grating mounting that enabled a closer approach. To reach higher q-ranges, one could use finer pitched gratings or a detector with higher spatial resolution may enable resolving the fringes for large separations, but the fringe visibility maybe reduced to an impractical level. That said, the q-range of a typical first order Talbot-Lau neutron interferometer is more tightly restricted due to the constraints from the wavelength specific Talbot-distance and the proximity of the sample with the gratings.

2.4.2 Results and Discussion

The pair of gratings that produced the highest visibility were installed and finely aligned with regards to pitch, roll and yaw, and overall yaw alignment with the beam. A scan of

Figure 2.20: Photo of the sample holders for the polystyrene sphere solution about 3 weeks after the measurements. The 4 mm thick holder is on the left and is clearly turbid, while the 1 mm thick holder is on the right showing that the spheres have settled out. Figure taken from Ref. [13].

the change in visibility with respect to the inter-grating spacing, D, was conducted, shown in Fig. 2.18.

A distribution of the visibility of the far-field interferometer flat field was observed, as can be seen in the raw images and persists for the range scanned D. The visibility distribution may be connected to the wavelength distribution of the flat field or to inhomogeneities in the etch depth of the gratings. A ray-tracing simulation of the beam line shows that the average wavelength in the beam center (corresponding to the right-hand side of the images) is about 0.55 nm and increases to about 0.8 nm where the highest visibility is observed on the left.

To assess the quantitative measurement of the microstructure with the far-field interferometer, a monodisperse solution of 1.97 ± 0.34 μm diameter polystyrene spheres with sample thickness 1 mm and 4 mm were imaged. The polystyrene spheres were in a solvent mixture of 50% H_2O, 50% D_2O (by volume) to give a sphere volume fraction $\phi_v = 0.05$ so that the mass densities of solid spheres and solvent were nearly matched to prevent sedimentation during the measurement. The pair correlation function of the sample can be approximated by:

$$G(\zeta) = \sqrt{1 - \frac{\zeta^2}{4r^2}} \left(1 + \frac{\zeta^2}{8r^2}\right) + \frac{\zeta^2}{2r^2} \left(1 - \frac{\zeta^2}{16r^2}\right) \ln \left[\frac{\zeta/r}{2 + \sqrt{4 - \zeta^2/r^2}}\right] \sim e^{-\frac{8}{9}\frac{\zeta}{r}} \tag{2.30}$$

Therefore as ζ increases, as per Eq. 2.28 and Eq. 2.29, the contrast reduction for dilute spheres of radius r should asymptotically approach:

$$\mu_d = \frac{3}{2} \phi_v \Delta\rho^2 \lambda^2 r. \tag{2.31}$$

The fringe visibility reduction was measured over the 1 cm diameter sample area and

is shown in Fig. 2.19. The data show a clear decrease in μ_d with grating separation (and hence ζ). We believe this is due to the fact that as the grating separation is increased, the wavelengths that contribute most strongly to the contrast are shifted to shorter wavelengths. Working on this assumption, we model the change in the average of the wavelength distribution as a ramp function:

$$\begin{aligned}\lambda(D) =&\lambda_1\Theta\{D_1 - D\} + \lambda_2\Theta\{D - D_2\} \\ &+ \Theta\{D - D_1\}\Theta\{D_2 - D\}\left(\lambda_1 + \frac{(\lambda_2 - \lambda_1)(D - D_1)}{(D_2 - D_1)}\right)\end{aligned} \tag{2.32}$$

where $\Theta\{...\}$ is the Heaviside function. The four free parameters were determined from a nonlinear least squares fit of the data using the pair correlation function for dilute spheres, which is shown as the solid lines in Fig. 2.19b. From the fit, $D_1 = (12.74 \pm 0.80)$ mm, $D_2 = (21.83 \pm 0.61)$ mm, $\lambda_1 = (0.643 \pm 0.013)$ nm, while $\lambda_2 = (0.515 \pm 0.003)$ nm, which are reasonable wavelengths for the cold neutron spectrum of the NG6 imaging beamline. While the model is somewhat heuristic, we intend to conduct spectral measurements of the NG-6 beamline to permit calculation of the visibility and thus provide a better correction. Further, this situation would not be present if the measurements were made with a monochromatic beam, either using a double crystal monochromator, velocity selector, or time of flight measurements.

Using Eq. 2.26 and Eq. 2.32 to calculate ζ, Fig. 2.19c shows μ_d/λ^2 for both the 1 mm and 4 mm thick samples. The predicted μ_d from a dilute monodisperse solution of polystyrene spheres is also plotted. The data show clear oscillations, which may indicate that multiple scattering is present or that the spheres are sticking together to create twin dumbbells. In the latter case the auto-correlation $|1-G(\zeta)|$ has an expected oscillation period of $(2/\pi)$diameter $= 1.25$ μm, which approximately matches the observed period of about 1.5 μm. That the oscillations are more prevalent in the 1 mm sample than the 4 mm sample is surprising, but the 1 mm sample showed a faster settling rate than the 4 mm thick sample, as shown in Fig. 2.20, indicating that there was likely a higher number of particles that formed dumbbell pairs.

In follow up experiments, a two PGMI setup was used to study sub-micron porosity detection in laser sintered stainless steel alloy 316 (SS316) test objects [80], and selective laser melted and conventionally manufactured SS316 dogbones [81].

2.5 Three Phase-Grating Moiré Interferometer[5]

This section describes the demonstration of a broadband, three PGMI operating in the far-field. The schematic diagram of the setup is depicted in Fig. 2.21. The three PGMI employs the universal moiré effect [65] and is an extension to the two PGMI [12, 13]. Contrary to the typical MZ interferometers that have two separate and distinct beam paths, the three PGMI works in the full-field of a cone beam from a finite source, similar to in-line holographic devices. Such full-field systems can be understood intuitively in the framework of Fourier imaging developed by Cowley and Moodie [82, 83]: the 2$^{\text{nd}}$ grating produces a series of

[5]This section is largely taken from Ref. [14].

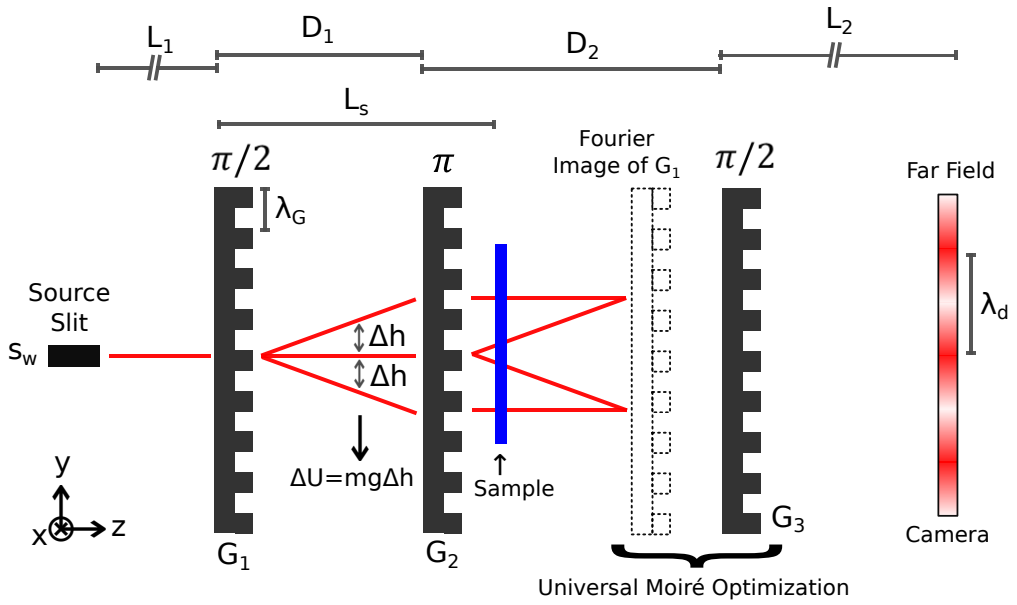

Figure 2.21: Three phase-grating interferometer schematic diagram where the 3^{rd} grating is offset from the echo-plane to produce the moiré pattern, with period λ_d, at the camera. The system can be analyzed as the superposition of continuous arrays of Mach-Zehnder interferometers; two of which are illustrated in the figure. This interferometer is sensitive to phase gradients, such as those induced by gravity. A sample may be placed between the gratings for phase imaging, or for dark field imaging. Figure taken from Ref. [14].

achromatic Fourier images of the 1st grating at a specific "echo-plane" downstream. The 3rd grating is detuned from the echo-plane to produce a phase moiré effect with the Fourier images, which is observed as a beat pattern in intensity in the far-field. When all three gratings have the same period (λ_G) the fringe period at the detector (λ_d) is given by [65]:

$$\lambda_d = \frac{(L_1 + D_1 + D_2 + L_2)}{|D_2 - D_1|}\lambda_G. \tag{2.33}$$

where L_1, D_1, D_2, and L_2 are defined in Fig. 2.21. The fringe frequency at the detector is given by $f_d = 1/\lambda_d$. The Fourier image and the 3rd phase-grating both possess regular square grating profiles. Therefore, the moiré pattern they create are broad straight fringes. If there is an angle between the two, the direction of the moiré fringes will rotate relative to the grating direction of the 3rd grating.

The experiments were performed at the Cold Neutron Imaging (CNI) facility [70] at the National Institute of Standards and Technology's (NIST) Center for Neutron Research (NCNR), where a 20 MW reactor provides a steady flux of thermal and cold neutrons for a variety of instruments. The CNI is located at the end position of neutron guide 6 and as such has a polychromatic neutron spectrum that is approximately given by a Maxwell-Boltzmann distribution with $T_c = 40$ K or $\lambda_c = 0.5$ nm. See Fig. 1.3 for the beamline's location at the NCNR.

For this demonstration, we used Si gratings which were available, but not necessarily optimal for our setup. The period of each grating was 2.4 μm. The 1st and 3rd gratings had

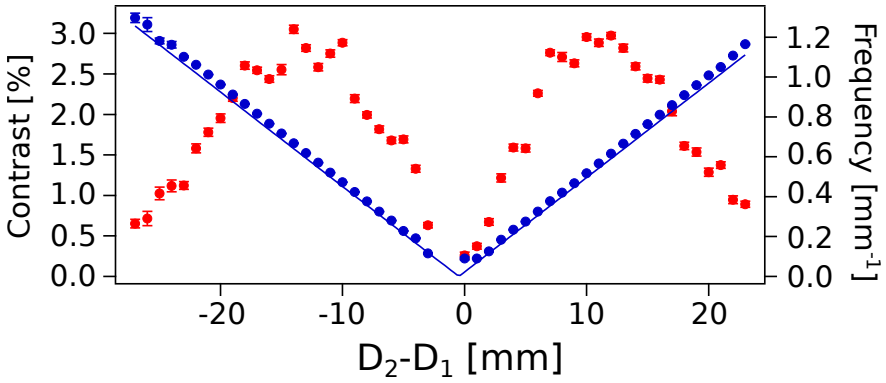

Figure 2.22: The measured contrast (red) and frequency (blue) of the interference pattern at the camera as a function of the difference between the grating separations. The uncertainties are purely statistical. The plotted theoretical frequency (straight blue line) derived from Eq. 2.33 shows good agreement with the measured data. Figure taken from Ref. [14].

a depth of 16 μm corresponding to a phase shift of $\sim \pi/2$ for the mean wavelength of 0.5 nm, while the 2$^{\text{nd}}$ grating had a depth of 30 μm corresponding to a phase shift of $\sim \pi$. The effect of a single $\pi/2$ or π phase-grating on the neutron transverse momentum distribution is shown in Fig. 2.2b. The gratings were oriented vertically to avoid beam deviation due to gravity. Rotational alignment of the gratings about the z-axis was done with 0.01° accuracy. The slit width was set to 500 μm and slit height to 1.5 cm. The slit to detector length was fixed at $L = 8.8$ m, while the distance between the slit and the 2$^{\text{nd}}$ grating was fixed at 4.75 m. The detector used was an sCMOS camera viewing a 150-μm-thick LiF:ZnS scintillator and had a spatial resolution of ~ 150 μm. The exposure time was 20 s per image, and the detector efficiency was ~ 0.4.

Contrast as a function of the difference between the grating separations $(D_2 - D_1)$ is plotted in Fig. 2.22. The distance between the 1$^{\text{st}}$ and 2$^{\text{nd}}$ grating was $D_1 = 4.6$ cm, while the distance between 2$^{\text{nd}}$ and 3$^{\text{rd}}$ grating, D_2, was scanned. In the methods section of [65] it is shown that the contrast is dependent on the autocorrelation functions of the 1$^{\text{st}}$ and 3$^{\text{rd}}$ grating profiles, and that for ideal 50% comb-fraction gratings the contrast peaks when the autocorrelation distances are half the grating period. For our geometry, $D_2 - D_1 \approx \pm 1.2$ cm values produce autocorrelation distances close to half a period for both 1$^{\text{st}}$ and 3$^{\text{rd}}$ gratings. The peak positions of the observed contrast agree with this prediction. At equal separation distances, $D_1 = D_2$, the third grating is at the Fourier image location and no fringes are expected. On Fig. 2.22 it can also be seen that the fringe frequency is linearly proportional to the difference of separation distances, as per Eq. 2.33.

The 1$^{\text{st}}$ and the 3$^{\text{rd}}$ grating can be translated away from the middle grating in synchronized intervals in order to achieve large interferometer length. Fig. 2.23 shows the peak contrast as a function of the distance from the 1$^{\text{st}}$ to the 3$^{\text{rd}}$ grating. The data are the contrast of the empty interferometer and illustrate how the contrast varies with the length of the interferometer, possibly pointing to coherence loss from increased air scattering and mechanical vibrations [84]. At each new length the contrast optimization was performed by finely translating the 3$^{\text{rd}}$ grating. Contrast was observed with an interferometer length of 4 m, which was the limit of our experimental setup. An interferometer area of ~ 8 cm^2 is

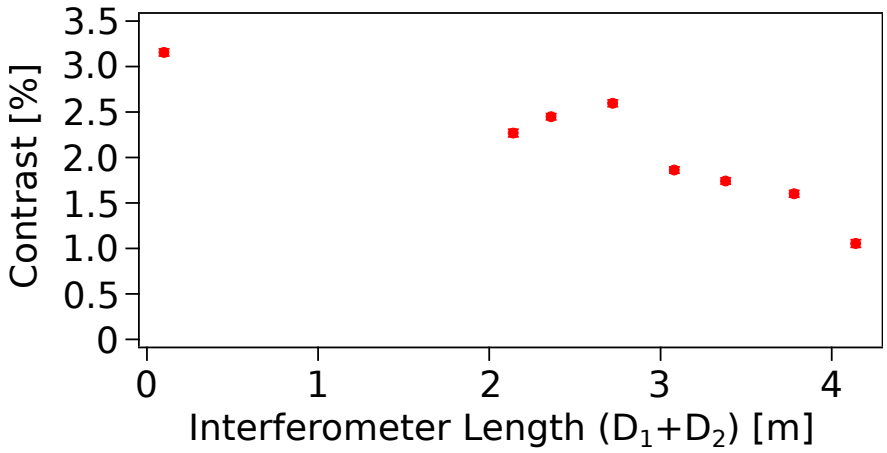

Figure 2.23: Peak contrast, where $D_2 - D_1 \approx 1.2$ cm, as a function of the distance between the 1st and 3rd grating. The purely statistical uncertainties are smaller than the individual points. Figure taken from Ref. [14].

estimated for that configuration.

To observe phase shifts inside the three PGMI and quantify the robustness of the setup we performed "linear phase stepping" depicted in Fig. 2.24. This process verifies that the phase shifts of the fringes from the grating movement agree with expected phase stepping behavior - movement of the grating by one period (2.4 μm) causes a 2π phase shift. Here the phase shift of the induced interference fringes is obtained by parallel translation of the third grating with step sizes smaller than the period of the gratings. It was observed that the phase of the interference fringes linearly increases as expected.

Placing a sample between the gratings allows for phase and dark-field imaging [12,85]. For a rectangular sample of 6061 aluminum alloy the linear attenuation of integrated intensity calculated as -ln(I_{sample}/I_{empty}) and the normalized contrast calculated as $\mathcal{C}_{sample}/\mathcal{C}_{empty}$ are shown in Fig 2.25. It is observed that the sample degrades the relative contrast to 0.28, most likely due to small angle neutron scattering off of the microstructure present in the alloy. The images were obtained by the harmonic analysis method described in [75].

The three PGMI presents a unique opportunity for material characterization as one can readily vary by orders of magnitude the autocorrelation length used to probe the sample. The method is analogous to the probing of autocorrelation lengths with a two phase-grating interferometer [13], but the probed autocorrelation length in this case is the separation length of the individual MZ interferometers depicted in Fig. 2.21:

$$\Delta h \approx \frac{\lambda}{\lambda_G} L_s \tag{2.34}$$

where L_s is the distance from the 1st grating to the sample. Therefore, the unique ability of the three PGMI is accessing larger autocorrelation lengths (>100 μm), which are beyond the standard limits of the ultra small angle neutron scattering (USANS) and other neutron dark-field imaging methods. Potential applications would be the probing of porous mineral samples and oil/gas core samples, man-made porous scaffolds and materials.

The enclosed area of the interfering neutron paths is an important parameter of a NI and

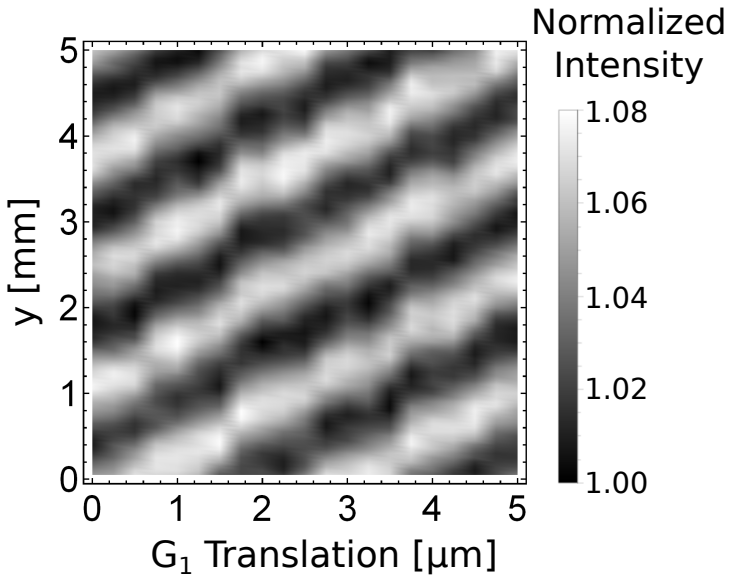

Figure 2.24: Phase stepping. The phase of the interference fringes at the detector is linearly varied by a parallel translation of the 3rd grating. The interferometer length was set to 2 m, and $D_2 - D_1 \approx 1.2$ cm to optimize contrast. The 3rd grating was then translated along the grating vector (along the y-direction in Fig. 2.21) from 0 to 5 μm in increments of 0.25 μm. Figure taken from Ref. [14].

its response to potential gradients and forces. Perfect crystal interferometers are limited to the practical size of commercially available perfect or dislocation free Si ingots. For perfect crystals with Bragg angles of $\sim \pi/4$ an area of ~ 100 cm^2 can be achieved for the particular monochromatic wavelength [48]. The three PGMI has the unique opportunity to reach and surpass the perfect crystal NI in this regard. In the current setup, with 2 m separation between the gratings, the enclosed area is ~ 8 cm^2 for 0.5 nm wavelength neutrons, while it is ~ 15 cm^2 for largest perfect crystal NI available at NIST for 0.271 nm neutrons. Reducing the grating period to 600 nm and upgrading to a longer beamline which can accommodate grating separation of 4.5 m will potentially increase the area to ~ 160 cm^2. Another key advantage of the three PGMI is in terms of the accepted neutron flux, as the uncertainties in the NI contrast measurements are purely statistical. The neutron acceptance of a perfect crystal is orders of magnitude smaller than the broadband acceptance of the three PGMI.

Although this initial demonstration achieved a maximum 3% contrast, the theoretical maximum contrast for square profile gratings is 32%. The factors that reduce the contrast are the finite slit width, which is estimated at a relative fraction of between 11% and 18% depending on the slit transmission profile; the actual phase-shift profile of G_2 which determines its efficiency; neutron scattering over the long distance of the NI by air or intervening parts such as vacuum windows. Contrast reduction with increased grating separation also points to scattering effects over distance and mechanical vibration as potential factors that degrade performance. Future work will include direct assessment of individual grating diffraction efficiencies to characterize and minimize these losses.

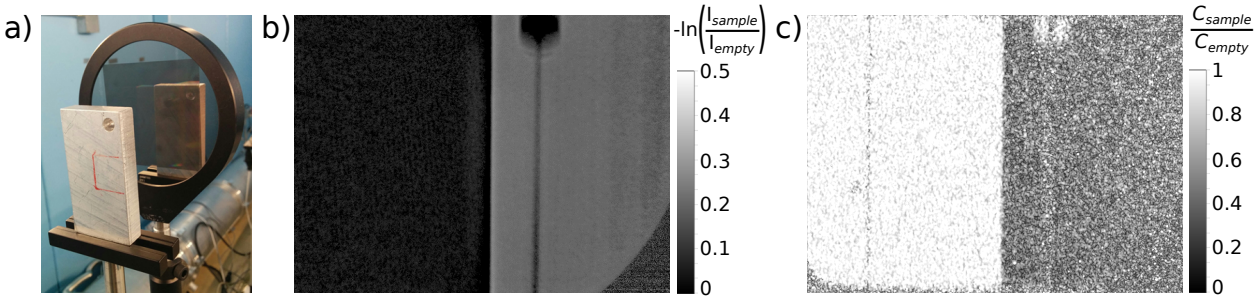

Figure 2.25: Sample imaging. a) A rectangular sample of 6061 aluminum alloy was placed downstream from the 2nd grating. b) Linear attenuation of integrated intensity. The shape of the sample and the hole in the corner are recognizable in the image. c) Normalized contrast. It is observed that the sample degrades the relative contrast to 0.28, most likely due to small angle neutron scattering off of the microstructure present in the alloy. Figure taken from Ref. [14].

2.5.1 Potential Applications

One of the hallmark neutron interferometer experiments was the "COW" experiment (named for the authors of the first paper: Collella, Overhauser, and Werner) which measured the phase shift of neutrons caused by their interaction with Earth's gravitational field [36], which is a measure of the local acceleration due to gravity "g". The interferometer used had an area of ~ 8 cm^2, and the most sensitive versions of the experiment were completed with $\delta g/g \approx 10^{-2}$ disagreement with expectations, but with a statistical uncertainty of $\delta g/g \approx 10^{-3}$ [86]. Recently it has been proposed that this disagreement may have been due to Bragg-plane misalignments in the interferometer blades [66]. Since the original COW experiments, g has been measured using neutrons with a very cold neutron interferometer at the 8×10^{-4} level [51] and a spin-echo spectrometer at the 10^{-3} level [87]. It should be noted that the current benchmark of $\delta g/g = 2 \times 10^{-11}$ is set by atom interferometry [62, 88, 89].

The three PGMI allows for a similar experiment, where the gratings and the source slit are rotated in synchronization around the beam axis as to vary the angle of the diffracted path, and thereby the induced gravitational potential. Considering only the current setup with $10^7\,\mathrm{mm^{-2}\,s^{-1}}$ neutron fluence rate and the 15 mm by 0.5 mm slit will yield an incoming flux of $N \approx 7.5 \times 10^7$ s^{-1}. With current contrast $\mathcal{C} = 0.01$ and detector efficiency $\eta = 0.4$, the uncertainty $\delta\phi$ in the phase (ϕ) due to counting statistics (shot noise) is:

$$\delta\phi = \frac{1}{\mathcal{C}\sqrt{\eta N t}} \approx 2.4 \times 10^{-3}\,\mathrm{rad} \tag{2.35}$$

in a $t = 1$ minute measurement time. The phase due to Earth's gravitational acceleration ($g = 9.8\,\mathrm{m\,s^{-2}}$) is:

$$\phi = gT^2\left(\frac{2\pi}{\lambda_G}\right) \approx 160\,\mathrm{rad}, \tag{2.36}$$

with grating period $\lambda_G = 2.4\,\mu$m, and $T = D_{12}/v_n$ is the neutron flight time between the

gratings where $v_n \approx 800\,\mathrm{m\,s^{-1}}$ is the peak neutron velocity. Thus one minute of measurement in the current setup would offer:

$$\frac{\delta\phi}{\phi} = \frac{\delta g}{g} \approx 1.5 \times 10^{-5}. \tag{2.37}$$

Furthermore, a successful realization of the COW experiment could lead to a similar experiment to measure big "G", the Newtonian constant of gravitation. The CODATA recommended value of $G = 6.67408(31) \times 10^{-11}\ \mathrm{m^3 kg^{-1} s^{-2}}$ with relative standard uncertainty of 4.7×10^{-5} [21] consists of several discrepant experimental results. One can take advantage of the long path of the three PGMI to place a large mass along the neutron paths. Benefit over atom interferometry would be precise knowledge of the neutron path w.r.t. to the source mass. In principle this would allow for a measurement using the three PGMI of $\delta G/G$ to a 10^{-5} level or smaller.

There are many aspects of the three PGMI that we can improve and expand. These include interferometer contrast which for our setup can reach up to 32% [65]. The factors that reduce the contrast are the finite slit width, which is estimated to reduce the contrast by between 11% and 18% depending on the slit profile; the actual phase-shift profile of G_2 which determines its efficiency; neutron scattering over the long distance of the NI by air or intervening parts such as vacuum windows. Future work will include direct assessment of individual grating diffraction efficiencies to characterize and minimize these losses. In addition to contrast gains, using smaller grating period and increasing the interferometer length will also improve the sensitivity of the three PGMI.

2.6 Conclusion

This chapter introduced and described the far-field phase-grating moiré neutron interferometers. The designs have a broad wavelength acceptance and requires non-rigorous alignment. The interferometers operate in the far-field regime and can potentially circumvent many limitations of the single crystal and grating based Mach-Zehnder type interferometers, and the near-field Talbot-Laue type interferometers that are in operation today. Mach-Zehnder type interferometers may provide the most precise and sensitive mode of measurements but a successful implementation requires highly collimated and low energy neutron beams. On the other hand, a near-field Talbot-Laue interferometer requires absorption analyzer gratings which curtails flux and interference fringe contrast. These constraints can be significant in a variety of applications.

The performance of the demonstrated interferometers was limited primarily by grating imperfections and detector resolution. However, the design is simple and robust. It is expected that the next generation of interferometers based on the far-field design will open new opportunities in high precision phase based measurements in materials science, condensed matter physics, and bioscience research. In particular, because of the moiré fringe exploitation in this type of interferometers, the uses may be highly suitable for the studies of biological membranes, polymer thin films, and materials structure. Also, the modest cost and the simplicity of assembly and operation will allow this type of interferometers to have wide acceptance in small to modest research reactor facilities worldwide.

The chapter also describes that using only phase modulating gratings, one can create a neutron far-field interferometer which creates neutron small-angle scattering images. One can easily tune the autocorrelation length probed by this far-field interferometer to obtain a measure of the microstructure of an object, thus providing multi-scale imaging capability. After correcting for a change in wavelength, the measured reduction in fringe visibility agree reasonably well with that expected from a monodisperse solution of spheres. The fairly broad range of probed autocorrelation length also allowed observation of a likely short-range ordering of the spheres.

Chapter 3

Neutron Orbital Angular Momentum and Applications to Holography[1]

3.1 Overview of $e^{i\ell\phi}$

Since their experimental demonstrations a quarter-century ago [90, 91], there has been great progress in generation, detection, and applications of "structured waves" of light and quantum particles, where the wavefront is patterned to attain nontrivial propagation characteristics such as orbital angular momentum (OAM), non-diffraction, and self-healing [92–96]. The structured OAM waves have demonstrated a number of applications in microscopy, encoding and multiplexing of communications, and manipulation of matter [97–103].

Electromagnetic waves can carry three types of momentum: linear momentum along the propagation axis which is described by Eq. 1.1, spin angular momentum (SAM) of $\pm\hbar$ associated with circular polarization, and OAM associated with an azimuthally varying phase profile $e^{i\ell\phi}$. Analogously, neutrons can carry three types of momentum: linear momentum along the propagation axis which is described by Eq. 1.3, spin angular momentum (SAM) of $\pm\hbar/2$ associated with the quantum spin, and OAM associated with an azimuthally varying phase profile $e^{i\ell\phi}$. The azimuthal phase structure can clearly be associated with beams carrying OAM by looking at the analogous expressions in azimuthal coordinates for the momentum operator and the wavevector in terms of total phase (see Eq. 1.8, note that here the total phase of the wave is denoted by Φ to distinguish it from the azimuthal coordinate ϕ):

$$k_x = \frac{\partial\Phi}{\partial x} \quad \& \quad \hat{p}_x = -i\hbar\frac{\partial}{\partial x} \quad \Rightarrow \quad k_\phi = \frac{\partial\Phi}{\partial\phi} \quad \& \quad \hat{L}_z = -i\hbar\frac{\partial}{\partial\phi} \tag{3.1}$$

Poynting in 1909 postulated that circularly polarized light must carry an angular momentum of $\pm\hbar$ [104]. In 1936 Beth demonstrated the transfer of this angular momentum from circularly polarized light to the rotational motion of a birefringent wave plate [105]. The analogous form of angular momentum appears for spin$-1/2$ particles in the form of spin polarization which is an intrinsic form of angular momentum carried by elementary particles.

[1] The material in this chapter is largely taken from Refs. [16–18].

In 1992 Allen et al. recognized that light beams carrying "phase singularities" in the form of $e^{i\ell\phi}$ also carry a well defined OAM of $\ell\hbar$ [91]. Work on lines of phase singularities date back to Dirac's work of 1930s on magnetic monopoles [106]. Whereas electromagnetic phase singularities were considered by Nye and Berry in 1970s in their studies of Antarctic ice sheets [107]. OAM beams are also called "helical beams" because their wavefronts are helices (as opposed to planar wavefronts of plane waves which carry no OAM), and "doughnut beams" because their intensity in the far-field has a ring shape. Coullet in his work related the mathematics of helical beams to superfluid vortices and coined the term "optical vortex" [108], which is also used today.

The most direct way of generating OAM waves is to pass a Gaussian beam through an azimuthally varying potential gradient such as that of a spiral phase plate (SPP), as demonstrated by Beijersbergen et al. in 1994 [109]. A more versatile and useful method of generating helical phase beams is the use of pitch fork holograms which were first demonstrated by Bazhenov et al. in 1990 [90]. These optical devices are currently the standard means by which helical phase beams are generated.

Electron OAM was demonstrated in 2010 by M. Uchida and A. Tonomur [110]. The following year B. J. McMorran et al. demonstrated electron OAM with high values [111]. In 2015, my colleagues demonstrated the control of neutron OAM [15].

3.2 Basis States of Orbital Angular Momentum

For convenience let us consider a neutron beam propagating in the z-direction with momentum k_z, and the expectation values of momentum in the transverse plane equal to zero. The OAM operator in a cylindrical coordinate system (r, ϕ, z) is $L_z = -i\hbar\frac{\partial}{\partial\phi}$. The OAM eigenstates are a convenient basis for the neutron wave packet when the coherence lengths in the transverse directions are equal $\sigma_x = \sigma_y \equiv \sigma_\perp$, where $\sigma_{x,y} = 1/(2\Delta k_{x,y})$, and $\Delta k_{x,y}$ are the x and y spreads of the wave packet's transverse momentum distributions.

Under this cylindrical symmetry the neutron wave function is separable in terms of spin and each of the cylindrical coordinates $\Psi_s(r, \phi, z) = R(r)\Phi(\phi)Z(z)\,|s\rangle$, where $s \in \{\uparrow = \binom{1}{0}, \downarrow = \binom{0}{1}\}$ specifies the neutron spin state along the quantization axis. With the standard deviation of momentum being constant in the transverse direction, the transverse wave function $R(r)\Phi(\phi)$ may be described in terms of solutions to the 2-D harmonic oscillator, and the longitudinal wave function $Z(z)$ treated as a Gaussian wave packet. The eigenstates, denoted by $|n_r, \ell, k_z, s\rangle$, are specified by the radial quantum number n_r, the azimuthal quantum number ℓ, the wave vector along the z direction k_z, and the spin state s.

The eigenstates in cylindrical coordinates (r, ϕ, z) are

$$|n_r, \ell, k_z, s\rangle = \mathcal{N}\xi^{|\ell|}e^{-\frac{\xi^2}{2}}\mathcal{L}_{n_r}^{|\ell|}\left(\xi^2\right)e^{i\ell\phi}Z(z)\,|s\rangle\,, \tag{3.2}$$

where $\xi = r/\sigma_\perp$ is the rescaled radial coordinate, $\mathcal{N} = \frac{1}{\sigma_\perp}\sqrt{\frac{n_r!}{\pi(n_r+|\ell|)!}}$ is the normalization constant, $n_r \in (0, 1, 2...)$, $\ell \in (0, \pm1, \pm2...)$, and $\mathcal{L}_{n_r}^{|\ell|}\left(\xi^2\right)$ are the associated Laguerre poly-

nomials. The total neutron energy is

$$E_{\mathrm{T}} = \hbar\omega_{\perp}(2n_r + |\ell| + 1) + \frac{\hbar^2 k_z^2}{2m} - \vec{\mu}\cdot\vec{B}, \tag{3.3}$$

where $\vec{\mu}$ is the neutron magnetic dipole moment, $\omega_{\perp}^2 = \hbar/(2m\sigma_{\perp}^2)$, m is the neutron mass, and $\vec{B}$ is the external magnetic field.

Before we consider spin-orbit states of neutrons it is useful to describe the action of a SPP in terms of orbital basis states. We may ignore the spin component here as the action of this spiral phase plate is spin independent. Consider a SPP of thickness $h(\phi) = h_0 + h_s\phi/(2\pi)$, where ϕ is the azimuthal angle, h_0 is the base height, and h_s is the step height. As a result of the optical potential, a neutron wave packet propagating on axis through the SPP acquires a phase of $\alpha(\phi) = -Nb_c\lambda h(\phi) = \alpha_0 + q\phi$, where Nb_c is the scattering length density of the SPP material, λ is the neutron wavelength, $q = -Nb_c\lambda h_s/(2\pi)$ and the uniform phase $\alpha_0 = -Nb_c\lambda h_0$. The parameter "$q$" is commonly referred to as the topological charge and it quantifies the nature of the singularity at the center. The operator of the SPP can be expressed as:

$$\hat{U}_{\mathrm{SPP}} = e^{i\alpha_0}e^{iq\phi}. \tag{3.4}$$

Generally, when a plane wave propagates through such a topology, the wavefronts become $|q|$ intertwined helical surfaces with a helicity defined by the sign of q.

Let the incident neutron state carry well defined quantum numbers $n_{r_{\mathrm{in}}}$ and ℓ_{in}:

$$|\psi_{\mathrm{in}}\rangle = |n_{r_{\mathrm{in}}}, \ell_{\mathrm{in}}\rangle\,, \tag{3.5}$$

where we suppress the k_z and s labels as they are unaffected by the SPP. To simplify we set $z = 0$ at the exit of the SPP and we set $\sigma_{\perp} = 1$. The state after the SPP can be expanded in terms of the basis functions

$$|\Psi_{\mathrm{SPP}}\rangle = \hat{U}_{\mathrm{SPP}}\,|\Psi_{\mathrm{in}}\rangle = \sum_{n_r=0}^{\infty} C_{n_r,\ell_{\mathrm{in}}+q}\,|n_r, \ell_{\mathrm{in}} + q\rangle\,. \tag{3.6}$$

with the coefficients

$$C_{n_r,\ell} = \int_0^{\infty} dr \int_0^{2\pi} d\phi\; r\langle n_r, \ell\,|\Psi_{\mathrm{SPP}}\rangle\,. \tag{3.7}$$

When the incoming neutrons have zero OAM ($n_{r_{\mathrm{in}}} = \ell_{\mathrm{in}} = 0$), the coefficients are

$$C_{n_r,\ell} = \begin{cases} e^{iq\pi}\mathrm{sinc}(q\pi) & \text{for } n_r = \ell = 0 \\ \frac{\frac{|\ell|}{2}\Gamma\left(1+\frac{|\ell|}{2}\right)}{\sqrt{n_r!(n_r+|\ell|)!}} e^{i(q-\ell)\pi}\mathrm{sinc}[(q-\ell)\pi] & \text{otherwise} \end{cases} \tag{3.8}$$

where $\Gamma\left(1 + |\ell|/2\right)$ is the gamma function. When the incoming state has a definite orbital

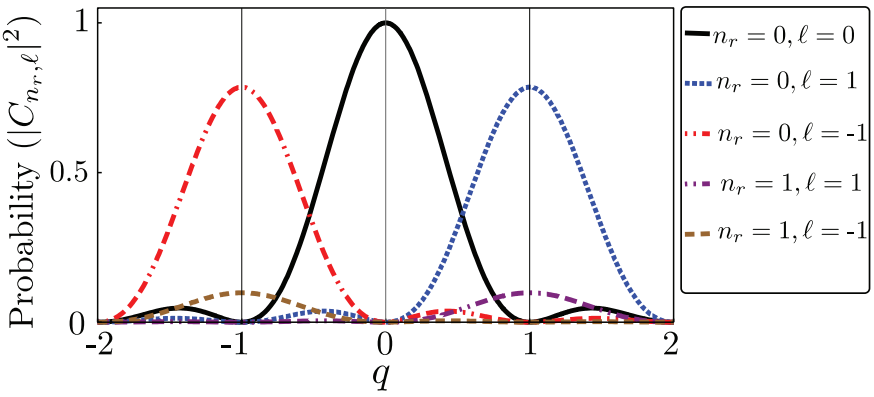

Figure 3.1: The probabilities for each of the $\ell = -1, 0, 1$ and $n_r = 0, 1$ states when a neutron wave packet with no OAM ($n_{r_{\text{in}}} = \ell_{\text{in}} = 0$) passes through a spiral phase plate with a topological charge q. Figure taken from Ref. [17].

quantum number ℓ_{in}, the output state is a state with definite orbital quantum number $\ell_{\text{in}} + q$.

Fig. 3.1 shows the probabilities $|C_{n_r,\ell}|^2$ for $n_r = 0, 1$ and $\ell = -1, 0, 1$. From Eq. 3.8 we see that $C_{n_r,\ell=0} \neq 0$ only when $n_r = 0$. From Fig. 3.1 we see that when a neutron wave packet with zero OAM passes through a SPP, the OAM quantum number of the neutron wave packet is incremented by the topological charge (q) of the SPP. The radial quantum number of the outgoing wave packet can take any allowed value, the most probable one is $n_r = 0$ for small q-values. If we consider, for example, a topological charge of $q = +1$ then the state after the SPP is

$$|\Psi_{\text{SPP}}\rangle = \sqrt{\frac{\pi}{16}} \sum_{n_r=0}^{\infty} \sqrt{\frac{1}{n_r!(n_r+1)!}} \, |n_r, 1\rangle \, . \tag{3.9}$$

Hence a SPP provides control over the orbital quantum number.

3.3 Intrinsic and Extrinsic Orbital Angular Momentum

Heretofore, we have discussed neutron wave packets for which the propagation axis coincides with the SPP or quadrupole axis. In this case, the SPP/quadrupole axis defines the OAM quantization axis. However, neutron beams are typically an incoherent superposition of neutron wave packets, where the neutron beam diameter is between 10^{-1} m and 10^{-4} m, and the transverse coherence length of the neutron wave packets, $\sigma_{\perp}$, is of the order of 10^{-5} m to 10^{-9} m [112, 113].

In studies of optical OAM a distinction is made between "extrinsic OAM" and "intrinsic OAM" [114, 115]. One can extend this distinction to the case of neutron beams. Extrinsic OAM is the orbital angular momentum centered about the SPP/quadrupole axis and it is given by the cross product of wave packet's position and its total linear momentum; intrinsic OAM, usually associated with helical wavefronts, is the orbital angular momentum

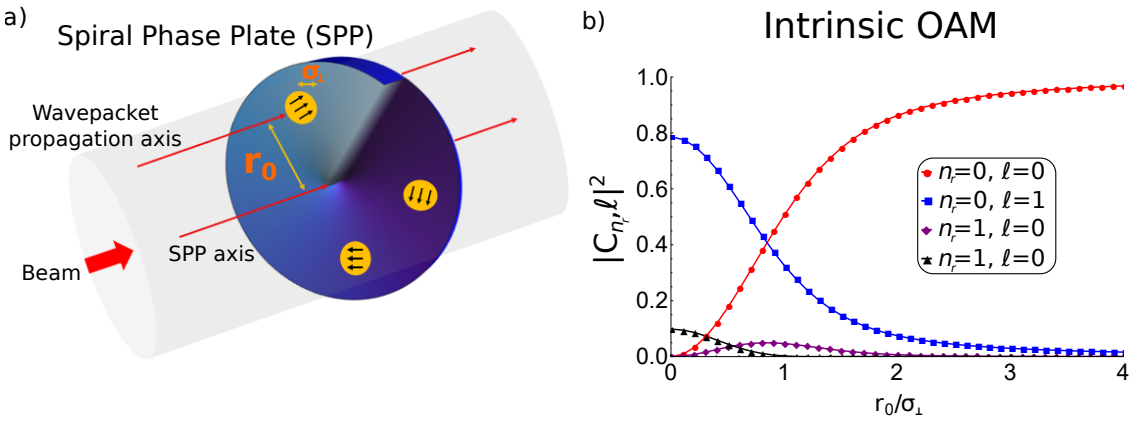

Figure 3.2: a) As the coherence length of the neutron wave packets is much smaller than the beam diameter, we may differentiate between "extrinsic OAM" calculated w.r.t. the SPP axis as the cross product of wave packet's position and its total linear momentum, and "intrinsic OAM" which is associated with helical wavefronts. The black arrows on top of the wave packets indicate the direction of the induced diffraction due to the SPP. b) The probabilities of the $n_r = 0, 1$ and $\ell = 0, 1$ states when a neutron wave packet with no OAM $n_{r_{\text{in}}} = \ell_{\text{in}} = 0$ passes through an SPP with $q = 1$. The probabilities are calculated w.r.t. the neutron's propagation axis and they are plotted as a function of the rescaled distance from the center of the SPP, $r_0/\sigma_\perp$, where r_0 is the distance between the SPP axis and the wave packet's propagation axis, and $\sigma_\perp$ is the transverse coherence length of the wave packet. Figure taken from Ref. [18].

represented by ℓ. The intrinsic OAM does not depend upon the position of the axis, provided that the axis is parallel to the propagation axis [116]. This is depicted on Fig. 3.2a which shows that a helical wavefront is induced only for the wave packet whose propagation axis coincides with the SPP axis.

Consider a neutron wave packet with $n_{\text{in}} = \ell_{\text{in}} = 0$ and which is centered on (r_0, ϕ_0):

$$|\Psi_{\text{o}}\rangle = \frac{1}{\sqrt{\pi\sigma_\perp^2}} e^{-\frac{r^2+r_0^2-2rr_0\cos(\phi-\phi_0)}{2\sigma_\perp^2}}, \tag{3.10}$$

After passing through an SPP which is centered at $r = 0$, the expectation value of OAM about the SPP axis is:

$$<\hat{L}_z> = \int_0^\infty dr \int_0^{2\pi} d\phi\, r \,\langle\Psi_{\text{o}}|\, \hat{U}_{\text{SPP}}^\dagger \left(-i\hbar\frac{\partial}{\partial\phi}\right) \hat{U}_{\text{SPP}}\, |\Psi_{\text{o}}\rangle = \hbar q. \tag{3.11}$$

Therefore all wave packets in the output beam acquire a well defined mean OAM relative to the SPP axis. Such wave packets are diffracted in the transverse direction, such that the induced external OAM relative to the SPP axis is independent of their location:

$$L_z = \vec{r} \times \vec{p} = r_0 \hbar k_\perp = \hbar q, \tag{3.12}$$

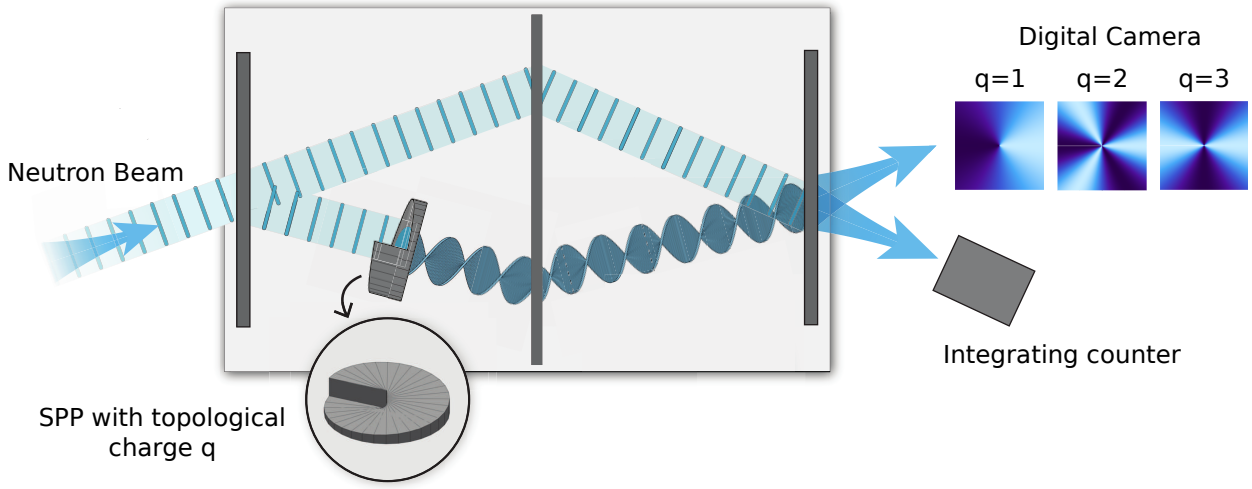

Figure 3.3: Schematic describing the experiment of Ref. [15] where an SPP was used to induce OAM onto the neutron beam. The phase profile of the beam was imaged via the perfect crystal NI as shown. The intensity profiles at the camera at the output are indicative of the azimuthal phase profile of an OAM beam.

where $k_\perp = q/r_0$ is induced by the SPP (in Fig. 3.2a the diffraction direction is depicted with black arrows).

On the other hand, as shown in Fig. 3.2b, the intrinsic OAM of a neutron wave packet quickly vanishes as the wave packet's propagation axis is displaced from the center of the SPP. The intrinsic OAM of the output beam has a Gaussian dependence to the displacement from the center of the SPP [117].

For material studies there is a need for methods to generate neutron spin-orbit states not restricted to one particular axis. This may be achieved by creating a lattice of spin-orbit states as described in the next section. When considering beams carrying OAM of major importance is the one fixed axis in space about which the OAM is quantized. In the case of beams carrying a lattice of OAM states there is a two-dimensional array of such axes and we are interested in what happens locally within each cell. Particularly, when this beam interacts with a material then the region around the local OAM axes becomes important.

3.4 Demonstration of Neutron Orbital Angular Momentum

In 2015 my colleagues demonstrated the control of neutron orbital angular momentum [15]. A brief description of the experiment is provided here.

The goal of the experiment, depicted in Fig. 3.3, was to increment neutron OAM by imparting an azimuthally varying phase over the beam via an SPP, and use the perfect crystal neutron interferometer (NI) to image the phase profile. The experiments were performed at the NIOF beamline which is described in section 1.4.3. The perfect crystal NI is described in section 1.4.2.

The standard method to characterize the induced OAM is to prepare the OAM beam in one arm of an interferometer. The output of the interferometer will then be a coherent superposition of the given OAM beam with a reference beam carrying no OAM. The 2D intensity profile of the output beam will possess a helical structure whose order of rotational symmetry equals $|q|$. Applying a phase shift between the two paths via a phase flag inside the interferometer effectively rotates the resulting 2D intensity profile. The direction of rotation determines the sign of q.

In the experiment of Ref. [15] several SPPs machined out of aluminum were used. The SPP diameter was 1 cm and the step heights correspond to ℓ =1, 2, 4, 7.5 for neutron wavelength of $\lambda = 0.271$ nm. The neutron beam diameter was ∼2 cm, while the transverse coherence lengths of the neutron wave packets were in the range of nanometers to micrometers.

3.5 Holography with a Neutron Interferometer

3.5.1 Introduction

Holography was introduced by Dennis Gabor in 1948 [118], who showed that a far-field electron micrograph of an object could be used to make a transmission mask that allows the object to be reconstructed with visible light. Due to subsequent advances in the brightness of electron sources and, notably, the development of techniques for numerical reconstruction [119], holography has since become a significant branch of electron microscopy [120]. Atomic-resolution neutron holography has been demonstrated and applied to the determination of crystal structures [121–123]. The advent of coherent laser light sources in the 1960s made all–optical holography practical [124, 125], to a degree that optical security holograms are now routinely printed on many paper currencies, credit cards, and identification documents [126, 127]. Holography remains a vibrant field of research in imaging science, as shown by numerous recent research papers.

This section describes the first demonstration of holography using neutron beams and macroscopic optical elements. Although deployed in a neutron interferometer (NI) with a Mach-Zehnder configuration [33], the method is a simple adaptation of the two-beam wedge technique introduced by Leith and Upatnieks [124, 125], and it is discussed using the conventional terminology of object, reference and reconstruction beams.

The object is a spiral phase plate (SPP) that was previously used to impart orbital angular momentum (OAM) to neutron waves [15]. In this respect the experiment is a neutron analogue of the holography of braided optical fibers performed by Bazhenov, Vasnetsov and Soskin [90]. The neutron holograms resemble the fork dislocation gratings synthesized by them and by Heckenberg, *et al.* [128], which have since been used to transfer angular momentum to electrons [110, 111] and light [129]. Digital reconstruction of this hologram provides information about the phase generated by the SPP, which should be useful in the design of the next generation of neutron OAM experiments.

Holography provides a direct connection between the refractive and diffractive mechanism of OAM imprinting of particles and waves. This first demonstration of neutron holography of a macroscopic object suggests that the complex grating methods used to produce OAM,

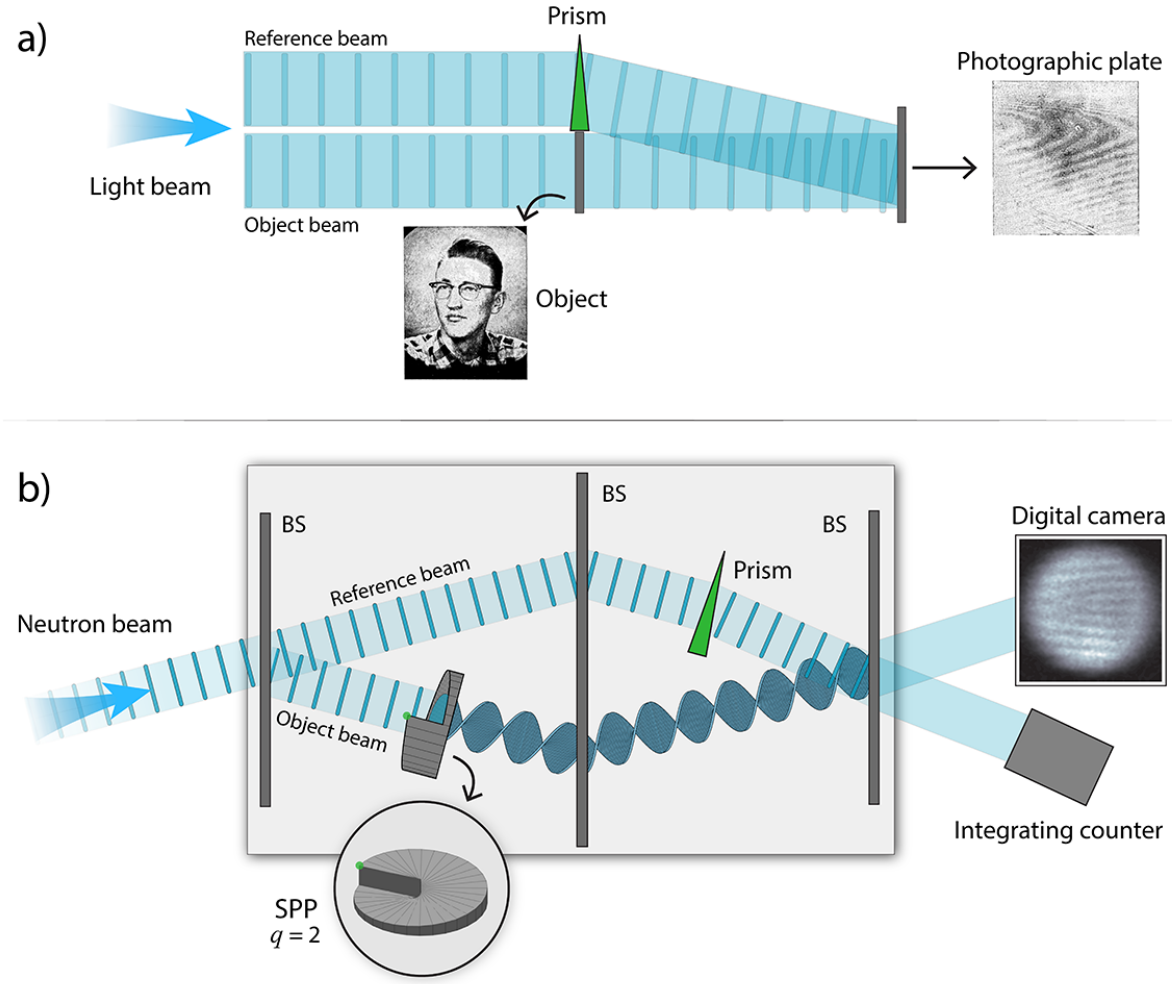

Figure 3.4: a) The off-axis method of optical holography of semitransparent objects introduced by Leith and Upatnieks. The object here is a continuous-tone transparency; its hologram was recorded on a photographic plate. The object shown here is actually the holographic reconstruction of the original object, said to be a good facsimile of the original. b) An artistic depiction of the neutron holography experiment. A neutron enters a single-crystal silicon Mach-Zehnder neutron interferometer (NI) and is separated into two paths by the left beamsplitter (BS). A spiral phase plate (SPP) with q = 2 is placed in the lower path, generating the object beam; a prism tilts the wavefront of the upper path to provide the reference beam. Object and reference beams are reflected at the central BS, and are coherently combined at the right BS. One of the output beams of the right BS is sent to an imaging detector, the other to an integrating counter that serves as an intensity monitor. Note that the experiment is an expectation valued measurement over many events, each of which involves only a single neutron. That is, there is one neutron at a time in the NI and the hologram is build up from an incoherent superposition of many events. Figure taken from Ref. [16].

Bessel, and Airy beams for light and electrons [130–132] may also be extended to neutrons.

3.5.2 Schematic of Neutron Holography

A NI is used to effect the coherent superposition of an object beam and a reference beam. As shown in Fig. 3.4b, the object beam consists of neutrons that have passed through an aluminum SPP in one arm of the NI. The SPP imprints a spatially-varying phase of $q\phi$ upon the neutron input beam, where q is the topological charge of the SPP and ϕ is the azimuthal angular coordinate on the neutron wavefront, with coordinate origin being the center of the SPP surface. The other arm of the NI provides the reference beam. The holographic image is constructed from the interferogram of object and reference beams, as recorded by a neutron sensitive digital camera. When no optical device is present in the reference arm, this interferogram displays the topological charge of the object beam, which is the same as that of a beam with OAM of $\ell\hbar$, where $\ell = q$. By placing a prism into the reference beam we introduce a linear gradient which effectively tilts the wavefronts.

The experiment is an expectation valued measurement over many events, each of which involves only a single neutron. In optics one would manipulate fully coherent beams and in the neutron case where an interferometer is used the coherence need only be larger than the deviation due to the prism and the object. There is no advantage in the neutron case in having the coherence beyond that because there is one neutron at a time in the interferometer and the hologram is built up from an incoherent superposition of many events. The neutron coherence length is a function of the beam momentum spread, and in our experimental setup it is on the order of microns, while the incident neutron beam is several millimeters in size, and the deviation due to the SPP and the prisms is on the order of nanometers. Hence the coherence length we use captures the physics needed to perform holography. We have combined neutron interferometry with holography and an appropriate coherence length must be used as the modification of the neutron coherence is extremely difficult and time consuming.

The transverse wave function of the incoming neutron wave packet, which is centered at an arbitrary position (x_0, y_0) in the beam, can be taken to be:

$$\Psi_{\mathrm{t}} = (2\pi\sigma^2)^{-1/2} e^{-\frac{(x-x_0)^2+(y-y_0)^2}{4\sigma^2}}, \tag{3.13}$$

where $\sigma_x = \sigma_y \equiv \sigma$ is the coherence length. After the first NI blade there is a coherent superposition of the two paths inside the interferometer. The wave function of the object beam (Ψ_o) acquires a $e^{-iq\phi}$ term due to the SPP and the wave function of the reference beam (Ψ_r) acquires a e^{-iky} term due to the prism; where k is proportional to the spatial gradient due to the prism, and y is the vertical coordinate in the plane of the image, as indicated in Fig. 3.4b. In addition, there is an intrinsic phase θ between the two paths. The last NI blade coherently combines the two paths and the intensity at the camera is then given by:

$$I = \int_0^d \int_0^d |\Psi_r + \Psi_o|^2 dx_0 dy_0 = A + B\cos(ky - q\phi + \theta), \tag{3.14}$$

where d is the beam size, and $d >> \sigma$; and A and B are experimental constants which are

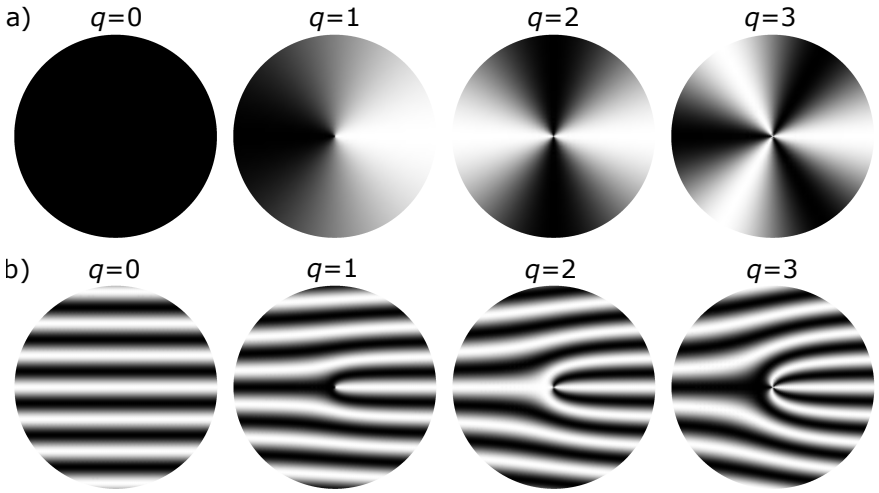

Figure 3.5: Simulation of the intensity profiles at the 2D detector for SPPs with topological charges of $q = 0, 1, 2, 3$ in the object beam, and (a) no prism in the reference beam, and (b) a prism in the reference beam. Fractional values of q correspond to admixtures of orbital angular momentum states with various integer values of ℓ. Note that the successive fork dislocations unfold as q passes through integer values. Figure taken from Ref. [16].

ideally equal to 1/2. The intensity profile is equivalent to what is obtained with a fully coherent beam. Figure 3.5a displays the calculated interferograms when only the SPP is present in the NI, and Fig. 3.5b shows the interferograms when both the SPP and the prism are present. We complete the holographic process by applying digital reconstructions to the measured forked dislocation structures, showing that they yield the phase and intensity profiles associated with the SPP.

3.5.3 Experimental Method

The experiment was performed at the NIOF beamline at the National Institute of Standards and Technology (NIST) Center for Neutron Research (NCNR) in Gaithersburg, MD [4, 5]. See Fig. 1.3 for the beamline's location at the NCNR, and see section 1.4.3 for a description of the NIOF beamline. The $\lambda = 0.271$ nm wavelength neutrons are incident onto a perfect crystal NI. See section 1.4 for a detailed description of the NI.

An aluminum SPP with $q = 2$ was placed in the object beam of the NI. The construction of the SPP is described in Ref. [15]. We note here that the SPP was made with a standard milling machine cutting a spiral staircase into the surface of a segment of aluminum dowel. A topological charge $q = 2$ is obtained with a staircase with a total vertical descent of 224 μm, which is $\approx 10^6 \times \lambda$. Those experienced in optical design for visible light may find it surprising that the mechanical figure of an optical component need only be controlled within a few thousand multiples of the operational wavelength. This is possible with neutrons, since neutron indices of refraction for most materials differ from unity by a few parts per million.

In the reference beam a vertical linear gradient was introduced by using two identical fused silica optical wedges arranged back-to-back. These wedges had a 6° angle and each could be rotated independently a full rotation of 2π. Note that any non-gradient phase shift

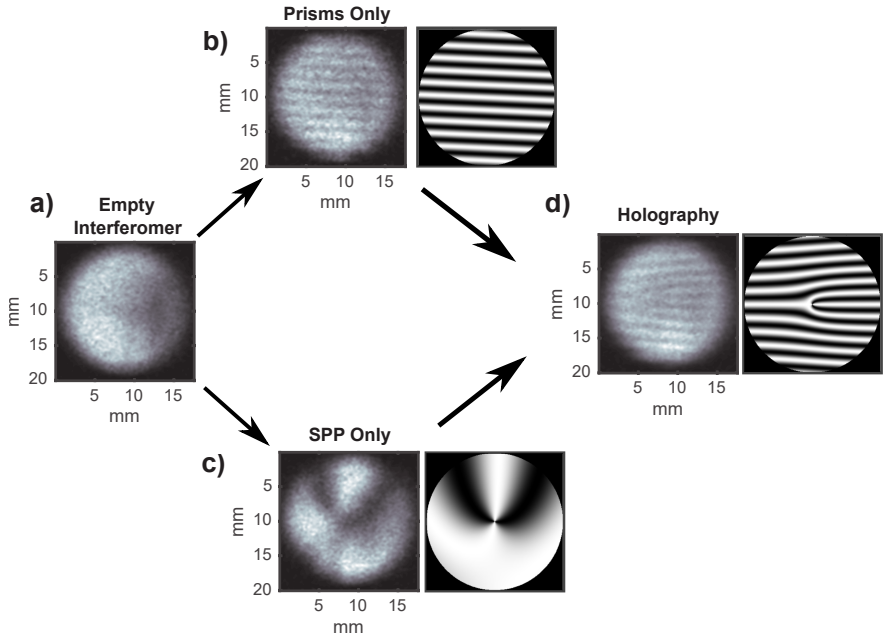

Figure 3.6: Measured and simulated interferograms at the 2D detectors for the $q = 2$ SPP and 6° fused silica prism independently, as well as when both are placed in the neutron interferometer to produce the pitch fork pattern. It is necessary to add a horizontal gradient of 0.3 rad/mm to the simulation to reproduce the measured images. Figure taken from Ref. [16].

inside the interferometer would only shift the pattern at the camera.

For the images depicted in Fig. 3.6, the wedges were adjusted to give a theoretical linear phase gradient of 3.4 rad/mm. Reactor fluctuations were monitored using the ^{3}He integrating counter. The interferograms were recorded on a neutron-sensitive digital camera that has an active area of 25 mm diameter and a spatial resolution of 100 μm. The neutron quantum efficiency of the camera is 18% and individual images were taken in 28-hour runs. The average of three images was used for analysis.

3.5.4 Results

Figure 3.6 depicts interferograms for four different configurations. Figure 3.6a shows the grayscale intensity profile obtained with an empty interferometer. It can be seen that the input beam is nonuniform. Figure 3.6b shows the experimental and simulated interferograms for the case in which only the prism is placed in the reference beam of the interferometer. The number of fringes in the simulated interferogram are in agreement with the measured image. Figure 3.6c shows the interferogram when only the SPP is present in the object beam. It is necessary to add a horizontal gradient of 0.3 rad/mm to the simulation for Figs. 3.6a and 3.6b to reproduce the measured figures. This horizontal gradient might explain the nonuniformity of Fig. 3.6a as well. Figure 3.6d shows the hologram obtained when the prism is placed in the reference beam and the SPP is placed in the object beam. The expected fork grating pattern is recognizable in this hologram.

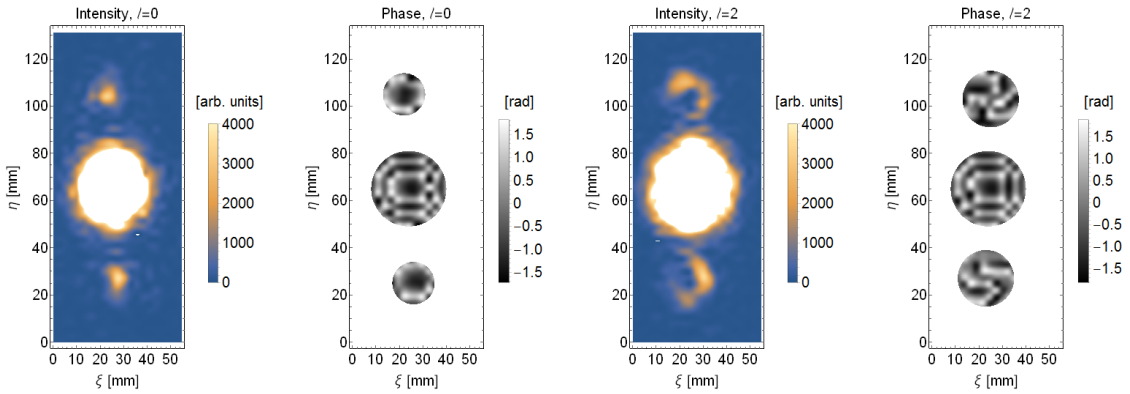

Figure 3.7: Intensity and phase profiles of the computed hologram reconstruction for the measured images in Fig. 3.6b corresponding to no SPP in the object beam; and Fig. 3.6d corresponding to a $q = 2$ SPP being in the object beam. Note that the phase range is from $-\pi/2$ to $\pi/2$, which is why we see four arms instead of two as seen on Fig. 3.5a, where the range is from $-\pi$ to π. The images are interpolated, and show the central 20x48 array of the numerical reconstruction. The mask for the phase plots is included for clarity. Figure taken from Ref. [16].

Figure 3.7 shows the numerical reconstruction of the experimental images shown in Figs. 3.6b and 3.6d. The reconstruction was obtained by computing the Fresnel-Kirchhoff diffraction integral in the Fresnel limit for $\lambda d = 70$ mm^2 using the expression:

$$\Gamma(\nu,\mu) = \frac{i}{\lambda d} e^{-i\pi\lambda d(\nu^2+\mu^2)} \mathcal{F}\left\{ h(x,y) \exp\left(-i\frac{\pi}{\lambda d}(x^2+y^2)\right)\right\} \tag{3.15}$$

where λ is the wavelength of the virtual wave illuminating the hologram; d is the distance between the hologram and the reconstruction plane; $\mathcal{F}$ is the Fourier transform; x and y are the hologram coordinates; $h(x,y)$ is the obtained hologram image; and ν and μ are the normalized forms of image reconstruction coordinates (ξ,η), such that $(\nu,\mu) = (\xi,\eta)/(\lambda d)$. The Fourier transform was computed using the Fast Fourier Transform algorithm. The reconstructed intensity, $|\Gamma|^2$, and the phase, $\tan^{-1}(\mathrm{Im}[\Gamma]/\mathrm{Re}[\Gamma])$, were then computed.

For the hologram, it can be seen from the uniform intensity distribution that the zero diffraction order corresponds to $\ell = 0$, while the first diffraction order displays the doughnut profile indicative of a beam carrying OAM. By plotting the reconstructed phase we confirm that the first diffraction beams correspond to beams with $\ell = 2$ as expected. Note that the spherical phase outside the Fourier transform was dropped in the Eqn. 3.15 reconstruction integral in order to look down the diffracted OAM beam paths and not along the reconstruction plane normal.

Chapter 4

Preparation of Spin-Coupled Orbital Angular Momentum States [1]

4.1 Introduction

In addition to possessing spin angular momentum, beams of light [91], electrons [110, 111], and neutrons [15] can carry orbital angular momentum (OAM) parallel to their propagation axis. There have been many recent developments in preparation and detection of OAM waves [95, 133]. OAM waves have found applications in microscopy, encoding and multiplexing of communications, quantum information processing, and the manipulation of matter [97–103].

In addition, it is possible to create "spin-orbit" states in which the spin and orbital angular momentum are correlated. For light, the correlation is between OAM and the polarization degree of freedom (DOF) [134, 135], while for electrons and neutrons it is between OAM and the spin DOF [17, 136]. Optical spin-orbit beams have demonstrated applications in high resolution optical imaging, high-bandwidth communication, optical metrology, and quantum cryptography [137–140].

Neutrons are spin$-1/2$ particles, and therefore the spin provides a two-level DOF. A "spin-orbit" state is one in which spin and OAM are correlated. In this chapter we specifically consider states where the two spin eigenstates are correlated with different OAM states:

$$|\Psi_{\mathrm{SO}}\rangle = \frac{1}{\sqrt{2}}(|n_\uparrow, \ell_\uparrow, \uparrow\rangle + e^{i\beta}\,|n_\downarrow, \ell_\downarrow, \downarrow\rangle), \tag{4.1}$$

where $\ell_\uparrow \neq \ell_\downarrow$, and β is an arbitrary phase.

This chapter describes methods of producing neutron spin-orbit states using special geometries of magnetic fields. The techniques are based on coherent averaging and spatial control methods borrowed from nuclear magnetic resonance [141–144]. A highly robust method is introduced and described, applicable to both electromagnetic and matter wave beams, that can produce a beam consisting of a lattice of spin-orbit states. The practical methods for preparation and detection of neutron spin-orbit states are quantified and compared. Lastly, methods are proposed to characterize neutron spin-orbit states by measuring

[1] The material in this chapter is largely taken from Refs. [17–19].

correlations between the spin direction and the momentum projected to a specific axis. This detection technique may be used to overcome the main challenges associated with low flux and the small spatial coherence of neutron beams.

4.2 Spin Polarization Geometries of Spin-Orbit States

Following the nomenclature of polarization correlated OAM states [133], we classify neutron spin-orbit states according to their spin orientation profile. There are four categories of spin-orbit states with radially independent spin orientations as shown in Fig. 4.1. They are:

(a) "cylindrically polarized states" where the spin orientation is given by $\vec{P} = \cos(\beta)\hat{r} + \sin(\beta)\hat{\phi}$, where β is an arbitrary phase;

(b) "azimuthally polarized states" which are a subset of cylindrically polarized states where $\vec{P} = \pm\hat{\phi}$;

(c) "radially polarized states" which are a subset of cylindrically polarized states where $\vec{P} = \pm\hat{r}$; and

(d) "hybrid polarization states" where $\vec{P} = \sin(2\phi + \beta)\hat{r} + \cos(2\phi + \beta)\hat{\phi}$, where β is an arbitrary phase.

The simplest method to generate any of those four states is to pass an appropriate input state into the magnetic SPP of $q = \pm 1$, as the four categories arise when $\Delta\ell = \ell_\uparrow - \ell_\downarrow = \pm 1$. The optical spin-orbit states with analogous polarization orientation geometries are not characterized by $\Delta\ell = \pm 1$. This difference comes from the fact that on the Poincaré sphere that describes optical polarization, any two antipodal points refer to orthogonal polarization directions; while on the Bloch sphere that describes the spin-1/2 state, any two antipodal points refer to anti-parallel spin directions.

We consider a spin-orbit state for which one orbital quantum number is zero and the other ± 1. When $\ell_\uparrow = 0$ the hybrid polarized states of Fig. 4.1d possess $\{\ell_\uparrow = 0, \ell_\downarrow = -1\}$, and the cylindrically polarized states possess $\{\ell_\uparrow = 0, \ell_\downarrow = 1\}$. All of the states with given $\{\ell_\uparrow, \ell_\downarrow\}$ differ by a phase on the spin DOF. This phase can be directly varied by an external magnetic field along the spin quantization axis, B_z. For $\ell_\downarrow = 0$ the hybrid polarized states possess $\{\ell_\uparrow = 1, \ell_\downarrow = 0\}$ while the cylindrically polarized states possess $\{\ell_\uparrow = -1, \ell_\downarrow = 0\}$. Hence a π spin rotation around $\hat{\sigma}_\perp$ can be used to transform a state with hybrid polarization geometry into a state with cylindrical polarization geometry (and vice versa), but not to change $\Delta\ell$.

The preparation techniques described in this chapter can also produce spin-orbit states with radially dependent spin orientations. The main three categories are shown in Fig. 4.1: e) quadrupole spin-orbit state; and two skyrmion-like states: f) hedgehog and g) spiral. The described rules for radially independent spin-orbit states also apply to these radially dependent spin-orbit states.

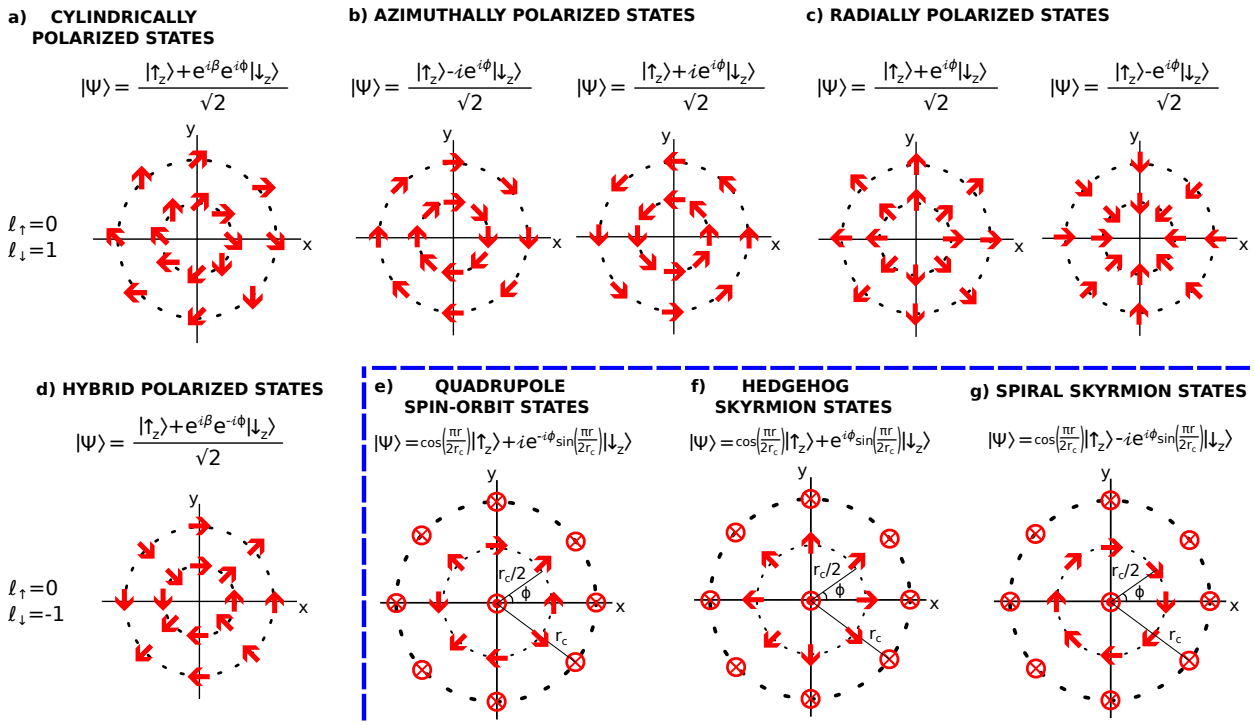

Figure 4.1: The spin orientation (red arrows) of the spin-orbit states with a coupling between $\ell_\uparrow = 0$ and $\ell_\downarrow = \pm 1$, where the $\hat{z}$ axis points out of the page. In analogy to optical OAM terminology, we may classify four categories of spin-orbit states with radially independent spin orientations: a) "cylindrically polarized states" where the spin orientation is given by $\vec{P} = \cos(\beta)\hat{r} + \sin(\beta)\hat{\phi}$, where β is an arbitrary phase; b) "azimuthally polarized states" which are a subset of cylindrically polarized states where $\vec{P} = \pm\hat{\phi}$; c) "radially polarized states" which are a subset of cylindrically polarized states where $\vec{P} = \pm\hat{r}$; and d) "hybrid polarization states" where $\vec{P} = \sin(2\phi + \beta)\hat{r} + \cos(2\phi + \beta)\hat{\phi}$, where β is an arbitrary phase. Note that all of the states with a certain $\{\ell_\uparrow, \ell_\downarrow\}$ differ by a phase on the spin DOF. The preparation techniques described in this chapter can also produce spin-orbit states with radially dependent spin orientations. The main three categories are: e) quadrupole spin-orbit states as described by Eq. 4.37; f) hedgehog skyrmion states; and g) spiral skyrmion states. An array of any of these three states can be obtained via the appropriate LOV prism pair combination. Figure taken from Ref. [18].

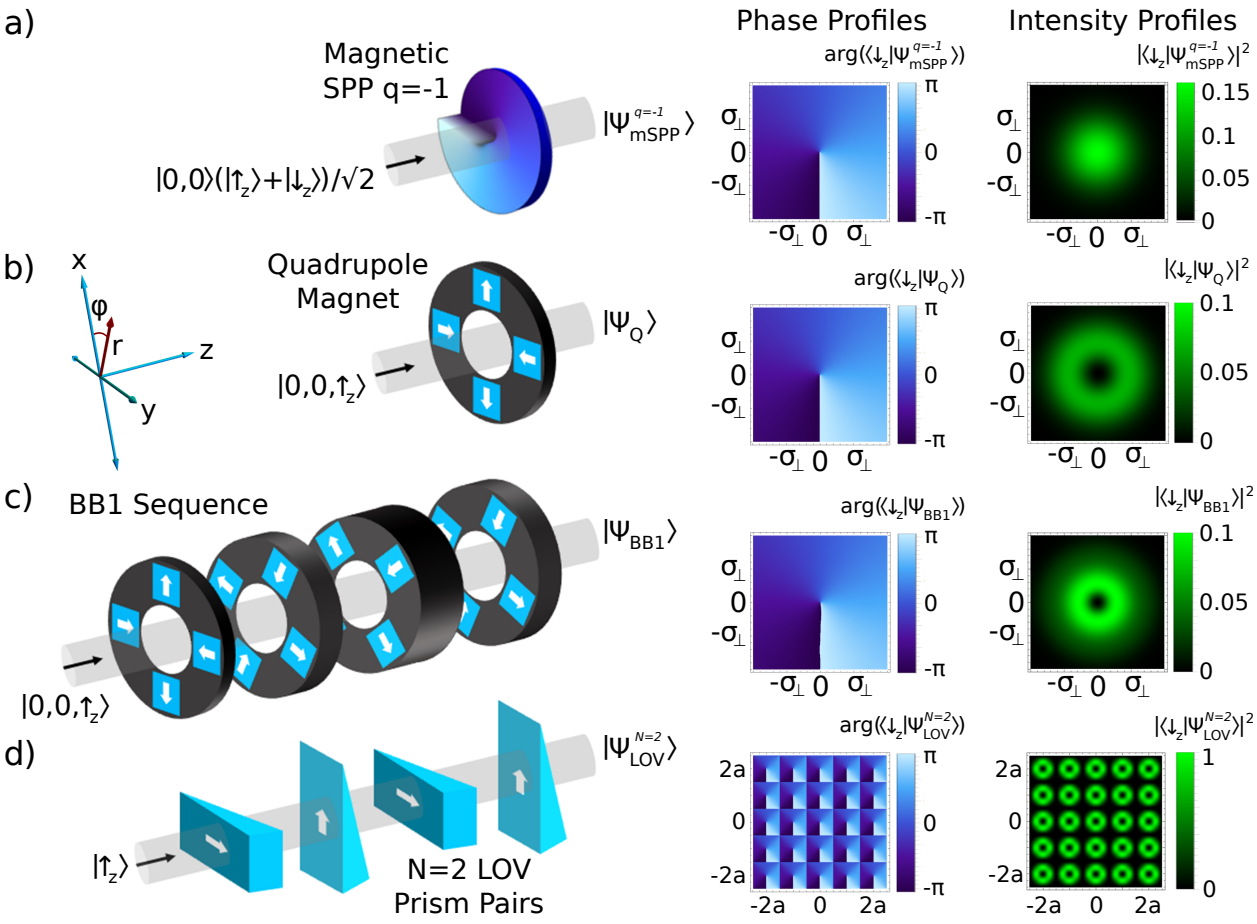

Figure 4.2: Four methods of producing neutron spin-orbit states. The phase and intensity profiles of the output states, post-selected on the spin state correlated to the OAM, are shown on the right. a) An incoming neutron wave packet in a coherent superposition of the two spin eigenstates passes through a magnetic SPP, which is made out of a material for which magnetic and nuclear scattering length are equal, thereby inducing an azimuthally varying phase for only one spin state. b) A spin-polarized neutron wave packet passes through a quadrupole magnetic field which induces the spin-orbit state. After transversing the quadrupole field, the intensity profile of the spin state correlated to the OAM has a ring shape. c) A sequence of quadrupoles with appropriate length and orientation acts as a BB1 pulse which increases the radii at which the spin and OAM are maximally entangled. d) A sequence of magnetic prisms (named LOV prism pairs) can be used to approximate the quadrupole operator and produce a lattice of neutron spin-orbit states. Figure taken from Ref. [18].

4.3 Methods to Prepare Neutron Spin-Orbit States

4.3.1 Magnetic Spiral Phase Plate

The spin-orbit state represented by Eq. 4.1 may be prepared by taking an incoming beam in a coherent superposition of spin up and spin down states (for convenience we shall choose the $\hat{z}$ axis to be the spin quantization axis and that $n_{r_{\text{in}}} = \ell_{\text{in}} = 0$):

$$|\Psi_{\text{in}}\rangle = \frac{1}{\sqrt{2}} |0,0\rangle \left(|\uparrow_z\rangle + |\downarrow_z\rangle\right), \tag{4.2}$$

and passing it through an SPP made out of a magnetic material. When such an SPP is magnetized along the spin quantization axis, its operator can be expressed as

$$\hat{U}_{\text{mSPP}} = e^{i[Nb_{\text{c}}\lambda h(\phi) + Nb_{\text{m}}\lambda h(\phi)\hat{\sigma}_z]}. \tag{4.3}$$

where b_{m} is the neutron magnetic scattering length of the material [27], and $\hat{\sigma}_z$ is the Pauli spin operator. Consider an SPP which is fabricated from a material whose nuclear and magnetic scattering lengths are equal, $b_{\text{c}} = b_{\text{m}}$. Then the phase acquired by one spin state would be $\alpha_{\uparrow}(\phi) = -N(b_{\text{c}} - b_{\text{m}})\lambda h(\phi) = 0$ and that of the other $\alpha_{\downarrow}(\phi) = -N(b_{\text{c}} + b_{\text{m}})\lambda h(\phi) = \beta + q\phi$, where now $q = -Nb_{\text{c}}\lambda h_{\text{s}}/\pi$ and $\beta = -2Nb_{\text{c}}\lambda h_0$. Using this magnetic SPP, spin-orbit states may be generated in the form of:

$$|\Psi^q_{\text{mSPP}}\rangle = \hat{U}_{\text{mSPP}} |\Psi_{\text{in}}\rangle \tag{4.4}$$

$$= \frac{e^{-\frac{r^2}{(2\sigma_\perp^2)}}}{\sqrt{2\pi\sigma_\perp^2}} (|\uparrow_z\rangle + e^{i\beta} e^{iq\phi} |\downarrow_z\rangle) \tag{4.5}$$

$$= \frac{1}{\sqrt{2}} (|0,0,\uparrow_z\rangle + e^{i\beta} \sum_{n_r=0}^{\infty} C_{n_r,q} |n_r, q, \downarrow_z\rangle). \tag{4.6}$$

The action of a $q = -1$ magnetic SPP is shown in Fig. 4.2a. For a convenient comparison with other methods of producing spin-orbit states we will set $\beta = \pi/2$ in Eq. 4.6. $|\Psi^q_{\text{mSPP}}\rangle$ possesses maximal single particle entanglement between the spin DOF and the OAM DOF as there is an equal superposition of $|\ell_\uparrow, \uparrow_z\rangle$ and $|\ell_\downarrow, \downarrow_z\rangle$.

4.3.2 Quadrupole Magnetic Field

Spin-orbit states can also be prepared with a quadrupole magnetic field [17]. In this case the OAM is induced via a Pancharatnam-Berry geometrical phase [145, 146]. The spin-orbit state is achieved by propagating a neutron wave packet that is spin polarized along the $\hat{z}$-direction,

$$|\Psi_{\text{in}}\rangle = |0,0,\uparrow_z\rangle\,, \tag{4.7}$$

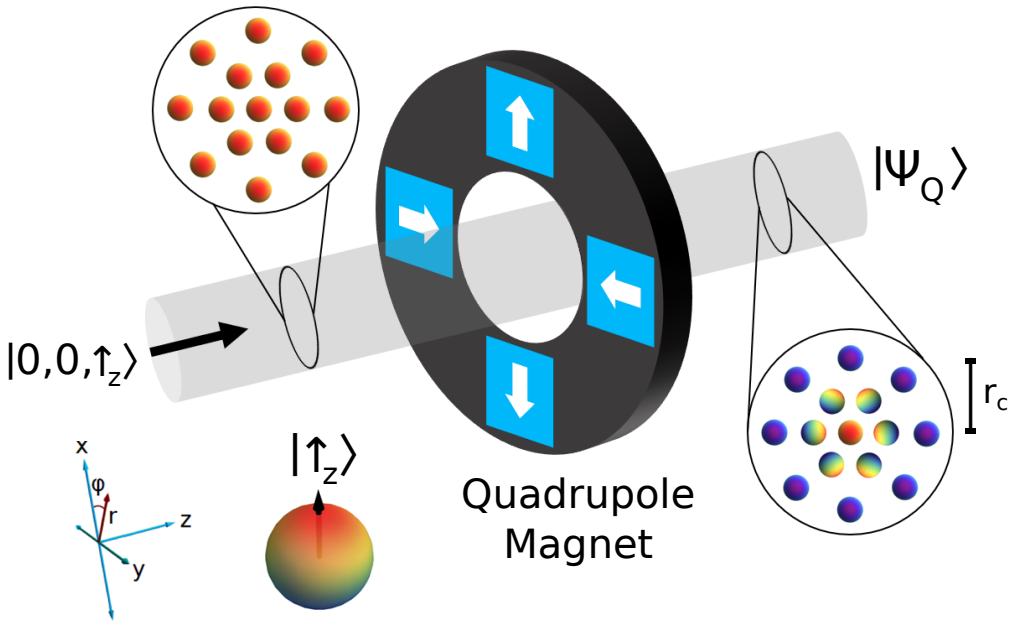

Figure 4.3: A spin-orbit state is achieved by propagating a neutron wave packet that is spin polarized along the $\hat{z}$-direction through a quadrupole magnetic field. In the output state the spin directions in the transverse plane acquire an azimuthal symmetry indicative of OAM.

through a quadrupole magnetic field $\vec{B} = K(-x\hat{x} + y\hat{y})$, where K is the magnitude of the quadrupole magnetic field gradient. The Hamiltonian of a neutron inside a magnetic field can be written as $H = \vec{\hat{\sigma}} \cdot \vec{B}\gamma\hbar/2$, where $\vec{\hat{\sigma}}$ is the vector of Pauli matrices $(\hat{\sigma}_x, \hat{\sigma}_y, \hat{\sigma}_z)$, and γ is the neutron gyromagnetic ratio. Assuming the neutron is traveling along the $\hat{z}$ axis, the time that the neutron spends inside the magnetic field is $\tau = d/v_z$, where d is the length of the quadrupole and v_z is the neutron velocity. By defining OAM raising and lowering operators $\hat{l}_\pm = e^{\pm i\phi}$ and spin operators $\hat{\sigma}_\pm = (\hat{\sigma}_x \pm i\hat{\sigma}_y)/2$, the quadrupole operator can be expressed as

$$\hat{U}_{\mathrm{Q}}(r_{\mathrm{c}}) = e^{-i\frac{\pi r}{2r_{\mathrm{c}}}[-\cos(\phi)\hat{\sigma}_x + \sin(\phi)\hat{\sigma}_y]} \tag{4.8}$$

$$= \cos\left(\frac{\pi r}{2r_{\mathrm{c}}}\right)\mathbb{1} + i\sin\left(\frac{\pi r}{2r_{\mathrm{c}}}\right)\left(\hat{l}_+\hat{\sigma}_+ + \hat{l}_-\hat{\sigma}_-\right), \tag{4.9}$$

where we have re-parametrized the quadrupole operator using the characteristic radial distance r_{c} at which the spin undergoes a π rotation after passing through the quadrupole,

$$r_{\mathrm{c}} = \frac{\pi v_z}{\gamma K d}. \tag{4.10}$$

The state after the quadrupole can be expanded in the basis functions of Eq. 3.2 as

$$\begin{aligned}|\Psi_{\mathrm{Q}}\rangle &= \hat{U}_{\mathrm{Q}}\,|\Psi_{\mathrm{in}}\rangle \\ &= \frac{e^{-\frac{r^2}{(2\sigma_\perp^2)}}}{\sqrt{\pi\sigma_\perp^2}}\left[\cos\left(\frac{\pi r}{2r_{\mathrm{c}}}\right)|\uparrow_z\rangle + ie^{-i\phi}\sin\left(\frac{\pi r}{2r_{\mathrm{c}}}\right)|\downarrow_z\rangle\right] \\ &= \sum_{n_r=0}^{\infty}\sum_{\ell=-\infty}^{\infty}\left(C_{n_r,\ell,\uparrow}\,|n_r,\ell,\uparrow\rangle + iC_{n_r,\ell,\downarrow}\,|n_r,\ell,\downarrow\rangle\right). \end{aligned} \tag{4.11}$$

The coefficients are given by

$$C_{n_r,\ell,\uparrow} = \int_0^{\infty} d\xi \int_0^{2\pi} d\phi\ \langle n_r,\ell\,|n_{r_{\mathrm{in}}},\ell_{\mathrm{in}}\rangle\,\xi\cos\left(\frac{\pi\sigma_\perp}{2r_c}\xi\right) \tag{4.12}$$

$$C_{n_r,\ell,\downarrow} = \int_0^{\infty} d\xi \int_0^{2\pi} d\phi\ \langle n_r,\ell\,|n_{r_{\mathrm{in}}},\ell_{\mathrm{in}}\rangle\,\xi e^{i\phi}\sin\left(\frac{\pi\sigma_\perp}{2r_c}\xi\right) \tag{4.13}$$

Integrating over ϕ selects $\ell = \ell_{\mathrm{in}}$ for the spin-up coefficients, and $\ell = \ell_{\mathrm{in}} - 1$ for the spin-down coefficients. This simplifies Eq. (4.11) to

$$|\Psi_Q\rangle = \sum_{n_r=0}^{\infty}\left(C_{n_r,\ell_{\mathrm{in}},\uparrow}\,|n_r,\ell_{\mathrm{in}},\uparrow\rangle + iC_{n_r,\ell_{\mathrm{in}}-1,\downarrow}\,|n_r,\ell_{\mathrm{in}}-1,\downarrow\rangle\right). \tag{4.14}$$

Note that this coupling between spin and OAM can easily be seen from the quadrupole operator in Eq. (4.9).

The coefficients $C_{n_r,\ell_{\mathrm{in}},\uparrow}$ and $C_{n_r,\ell_{\mathrm{in}}-1,\downarrow}$ are real for all values of $r_c/\sigma_\perp$. The various coefficients $C_{n_r,\ell,s}$ are plotted in Fig. 4.4, given an input state with $n_{r_{\mathrm{in}}} = \ell_{\mathrm{in}} = 0$. The ratio $r_c/\sigma_\perp$ quantifies the action of the quadrupole on the neutron wave packet. The strong quadrupole fields regime corresponds to $r_c \to 0$ and the weak quadrupole regime to $r_c \to \infty$. It can be verified that

$$\sum_{n_r=0}^{\infty}\left(C^2_{n_r,\ell_{\mathrm{in}},\uparrow} + C^2_{n_r,\ell_{\mathrm{in}}-1,\downarrow}\right) = 1. \tag{4.15}$$

In Fig. 4.4 it is shown that to maximize the single particle entanglement between the spin and OAM the quadrupole magnet should be of such strength and length as to produce a spin flip over 1.82 times the coherence length of the wave packet, that is $r_{\mathrm{c}} = 1.82\sigma_\perp$.

The action of the quadrupole magnet is shown in Fig. 4.2b and Fig. 4.3. It can be observed that the intensity profile of the spin state which is correlated to the OAM is now a ring shape.

4.3.3 Spin-Orbit States with Higher Order OAM Values

The quadrupole magnetic field method described above takes a spin-polarized input state with $\ell_\uparrow = \ell_\downarrow = 0$ and outputs a spin-orbit state with $\ell_\uparrow = 0$ and $\ell_\downarrow = \pm 1$. We now consider situations where the spin-orbit correlations involve higher order OAM values. With spin-orbit states generated via the magnetic SPP, this is a trivial matter of using a $|q| > 1$. For quadrupole magnetic fields the following sequence of j pulses may be used:

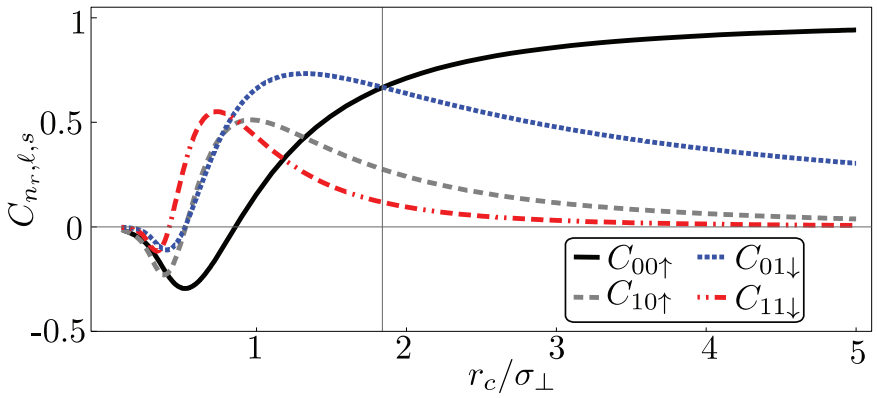

Figure 4.4: The coefficients $C_{n_r,\ell,s}$ of the spin-orbit state for $n_r = 0$ and $n_r = 1$ as a function of $r_c/\sigma_\perp$. The input state is $n_{r_{\text{in}}} = \ell_{\text{in}} = 0$. The vertical line at $r_c/\sigma_\perp = 1.82$ corresponds to the point of maximum concurrence for the $n_r = 0$ subspace. Strong quadrupole fields correspond to $r_c \to 0$ while no quadrupole $r_c \to \infty$. Figure taken from Ref. [17].

$$
\begin{aligned}
|\Psi_{\text{Q}}^{j}\rangle &= \left(\hat{U}_{\text{Q}}(r_{\text{c}}) e^{-i\frac{\pi}{2}\hat{\sigma}_x} |{\downarrow_z}\rangle \langle{\downarrow_z}|\right)^{j} \hat{U}_{\text{Q}}(r_{\text{c}}) |0,0,{\uparrow_z}\rangle \\
&= \frac{e^{-\xi^2/2}}{\sqrt{\pi\sigma_\perp^2}} \left[\cos\left(\frac{\pi r}{2r_{\text{c}}}\right) \sin^{j}\left(\frac{\pi r}{2r_{\text{c}}}\right) |{-j},{\uparrow_z}\rangle + i \sin^{j+1}\left(\frac{\pi r}{2r_{\text{c}}}\right) |{-(j+1)},{\downarrow_z}\rangle\right]
\end{aligned}
\tag{4.16}
$$

where $|{\downarrow_z}\rangle \langle{\downarrow_z}|$ is the projection operator for a spin-down state. The $j = 0$ case corresponds to the spin-orbit state produced via a quadrupole magnetic field as described in Eq. 4.37. For $j > 1$, both $|{\uparrow_z}\rangle$ and $|{\downarrow_z}\rangle$ are correlated to higher order OAM values, and the intensity profiles of $\langle{\uparrow_z}|\Psi_{\text{Q}}^{j}\rangle$ and $\langle{\downarrow_z}|\Psi_{\text{Q}}^{j}\rangle$ are both ring shapes.

4.3.4 BB1 Sequence

After a neutron wave packet passes through a quadrupole magnetic field, the maximally entangled spin-orbit state, given by $|\Psi_{\text{mSPP}}^{q=-1}\rangle$ (see Eq.4.6), occurs for $r = r_{\text{c}}/2$. However, the range of maximal entanglement can be increased by using a sequential chain of appropriately oriented quadrupole magnets. We will see that this results in the ability to increase the width of the ideal ring filter without significantly affecting the amount of spin-orbit entanglement, boosting post-selection performance. To begin, notice that the situation with a single quadrupole magnet resembles a standard over/under-rotation pulse error in spin physics [144]: with a fixed azimuthal coordinate ϕ, as the radial coordinate deviates from the ideal value $r = r_{\text{c}}/2$, the spin undergoes a rotation about the $\hat{\phi}$ axis with a rotation angle greater or less than $\pi/2$. The amount of such over/under-rotation is fixed for a given value of r.

To increase robustness to these errors we consider the Broad-Band$_1$ (BB1) composite pulse [147] which can be implemented by sequential quadrupoles with different strengths and orientations. This particular composite sequence is considered because of its robust performance while using only four quadrupole magnets. It is important to note that applying

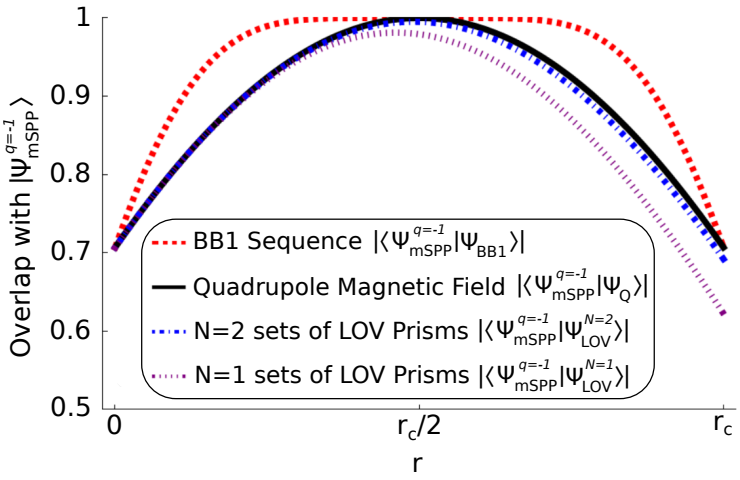

Figure 4.5: Overlap as a function of radius between the maximally entangled spin-orbit state $|\Psi_{\rm mSPP}^{q=-1}\rangle$ and output states produced by the following methods: (red) the BB1 sequence, $|\Psi_{\rm BB1}\rangle$; (black) the quadrupole, $|\Psi_{\rm Q}\rangle$; (blue) the N=2 sets of LOV prism pairs, $|\Psi_{\rm LOV}^{N=2}\rangle$; (purple) the N=1 sets of LOV prism pairs, $|\Psi_{\rm LOV}^{N=1}\rangle$. In each of these cases, $r_{\rm c} = 1.82\sigma_\perp$. Each lattice cell of $|\Psi_{\rm LOV}^{N=1}\rangle$ is shown to be a good approximation of $|\Psi_{\rm Q}\rangle$, and the approximation is improved by reapplying the LOV operator. It is also shown that the $|\Psi_{\rm BB1}\rangle$ has a larger range of radii than $|\Psi_{\rm Q}\rangle$ for which the spin and OAM are maximally entangled. Figure taken from Ref. [18].

the quadrupole operator repeatedly N times does not take the orbital quantum numbers outside the $\ell = 0, \pm 1$ values. That is, $[\hat{U}_{\rm Q}(r_{\rm c})]^N |\Psi_{\rm in}\rangle = \hat{U}_{\rm Q}(r_{\rm c}/N) |\Psi_{\rm in}\rangle$, where the quadrupole operator $\hat{U}_{\rm Q}(r_{\rm c})$ was defined in Eq. 4.8. However, the standard magnetic quadrupole can be rotated by an angle δ about the $\hat{z}$ axis. In this case its interaction is described by the modified operator, $\hat{\mathcal{U}}_{\rm Q}(r_{\rm c}, \delta) = e^{-i\frac{\delta}{2}\hat{\sigma}_z} \hat{U}_{\rm Q}(r_{\rm c}) e^{i\frac{\delta}{2}\hat{\sigma}_z}$, and the BB1 sequence results in the output state

$$|\Psi_{\rm BB1}\rangle = \hat{\mathcal{U}}_{\rm Q}\left(\frac{r_{\rm c}}{2}, \delta_1\right) \hat{\mathcal{U}}_{\rm Q}\left(\frac{r_{\rm c}}{4}, \delta_2\right) \hat{\mathcal{U}}_{\rm Q}\left(\frac{r_{\rm c}}{2}, \delta_1\right) \hat{\mathcal{U}}_{\rm Q}\left(r_{\rm c}, 0\right) |\Psi_{\rm in}\rangle\,, \tag{4.17}$$

where $\delta_1 = \cos^{-1}(-1/8)$ and $\delta_2 = 3\delta_1$. These angles were tuned to eliminate 1st and 2nd order over/under-rotation errors [147].

To quantitatively compare $|\Psi_{\rm BB1}\rangle$ with $|\Psi_{\rm Q}\rangle$ we can look at their overlap with the maximally entangled spin-orbit state $|\Psi_{\rm mSPP}^{q=-1}\rangle$ of Eq. 4.6. The overlap between two states $|\Psi_1\rangle$ and $|\Psi_2\rangle$ is given by $|\langle\Psi_1|\Psi_2\rangle|$, and it is a measure of the closeness of two quantum states, with a value of unity for identical states. Fig. 4.5 shows $|\langle\Psi_{\rm mSPP}^{q=-1}|\Psi_{\rm BB1}\rangle|$ and $|\langle\Psi_{\rm mSPP}^{q=-1}|\Psi_{\rm Q}\rangle|$ as a function of radius. It is clear that $|\Psi_{\rm BB1}\rangle$ has a larger range of radii for which the spin and OAM are maximally entangled. This can also be observed in the intensity profile of $\langle\downarrow_z|\Psi_{\rm BB1}\rangle$ that is plotted in Fig. 4.2c, where the inner dark region is smaller than that of Fig. 4.2b.

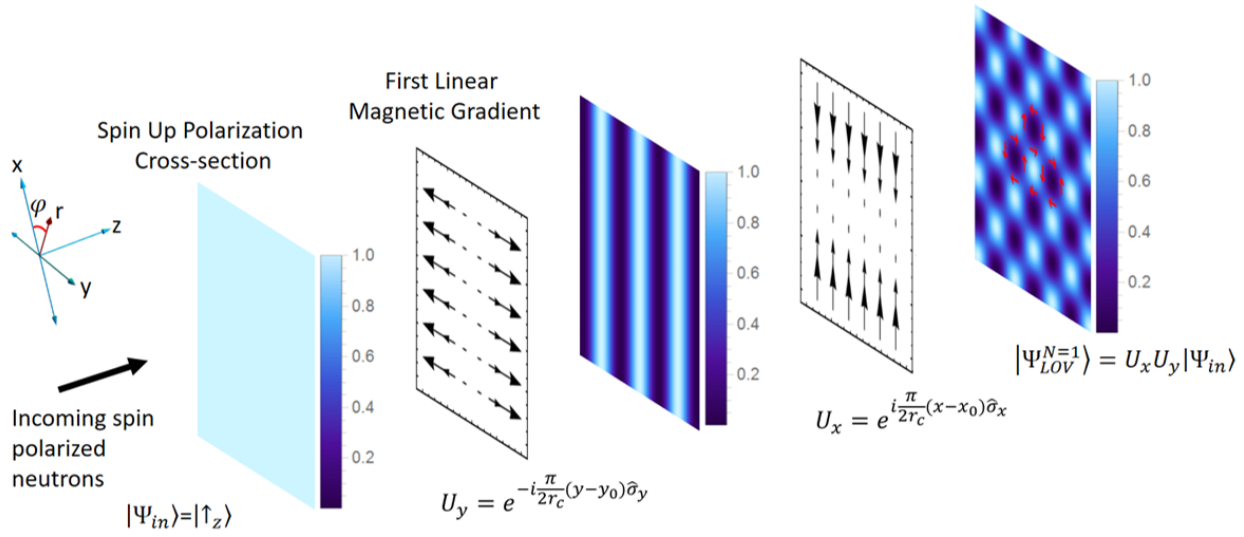

Figure 4.6: Spin up polarization profile as the beam passes through linear magnetic field gradients. The two gradients constitute a LOV prism pair which is used to create lattices of spin-orbit states.

4.3.5 Lattices of Spin-Orbit States

The method to produce lattices of spin-orbit states via the LOV prism pairs is motivated by applying the Suzuki-Trotter expansion to Eq. 4.8:

$$e^{i\frac{\pi}{2r_c}(x\hat{\sigma}_x - y\hat{\sigma}_y)} = \lim_{N\to\infty} (e^{i\frac{\pi}{2r_c N}x\hat{\sigma}_x} e^{-i\frac{\pi}{2r_c N}y\hat{\sigma}_y})^N. \tag{4.18}$$

We can see that N set of perpendicular linear magnetic gradients approximates the quadrupole operator. Fig. 4.12 illustrates how the spin manipulation via magnetic field gradients gives rise to a lattice of azimuthally varying spin directions. Choosing that the operators be independent of N, we define the linear magnetic gradient operator as

$$\hat{U}_{\phi_g,\phi_m} = e^{-i\frac{\pi}{2r_c}[x\cos\phi_g + y\sin\phi_g][\hat{\sigma}_x\cos\phi_m + \hat{\sigma}_y\sin\phi_m]} \tag{4.19}$$

where ϕ_g (ϕ_m) indicates the gradient (magnetic field) direction in the $\hat{x}-\hat{y}$ plane. For spin$-1/2$ particles one way to approximate the magnetic linear gradient operators is with magnetic prisms as shown in Fig. 4.2d. In our preceding work of Ref. [19], described in section 4.5, we have termed such linear gradient operators as "Lattices of Optical Vortices" (LOV) prism pairs. The general LOV operator can be expressed as:

$$\hat{U}_{\mathrm{LOV}}^N = (\hat{U}_{\phi_g,\phi_m}\hat{U}_{\phi_g\pm\frac{\pi}{2},\phi_m\pm\frac{\pi}{2}})^N, \tag{4.20}$$

and the corresponding beams with lattices of spin-orbit states are given by:

$$|\Psi^N_{\mathrm{LOV}}\rangle = (\hat{U}_{\phi_\mathrm{g},\phi_\mathrm{m}}\hat{U}_{\phi_\mathrm{g}\pm\frac{\pi}{2},\phi_\mathrm{m}\pm\frac{\pi}{2}})^N\,|\Psi_\mathrm{in}\rangle\,. \tag{4.21}$$

This process is shown in Fig. 4.2d for $(\hat{U}_{\pi,0}\hat{U}_{\frac{\pi}{2},\frac{\pi}{2}})^2$ and $|\Psi_\mathrm{in}\rangle = |\uparrow_z\rangle$, where the output beam is a lattice of spin-orbit states with $\ell_\uparrow = 0$ and $\ell_\downarrow = -1$.

When considering beams carrying OAM of major importance is the one fixed axis in space about which the OAM is quantized. In the case of beams carrying a lattice of OAM states there is a two-dimensional array of such axes and we are interested in what happens locally within each cell. Particularly, when this beam interacts with a material then the region around the local OAM axes becomes important. However, although the spin-orbit beam can cleanly be described via Laguerre-Gaussian modes, the beam carrying a lattice of spin-orbit states can not due to the translational symmetry.

The orientations of the gradient operators give us the possibility of producing lattices of spin-orbit states with positive and negative values of OAM. For example, $(\hat{U}_{0,0}\hat{U}_{\frac{\pi}{2},\frac{\pi}{2}})^2$ applied to an incoming state of $|\Psi_\mathrm{in}\rangle = |\uparrow_z\rangle$ produces an output beam with a lattice of spin-orbit states with $\ell_\uparrow = 0$ and $\ell_\downarrow = 1$. Note that this particular gradient sequence approximates the action of a monopole magnetic field geometry. Furthermore, we can obtain lattices of spin-orbit states with higher order OAM values by substituting the LOV operator, $\hat{U}^N_{\mathrm{LOV}}$, in place of the quadrupole operators, $\hat{U}_\mathrm{Q}(r_\mathrm{c})$, in Eq. 4.16.

Due to the periodic nature of the linear gradient operators, the spin-orbit states in these beams form a two-dimensional array with a lattice constant of

$$a = \frac{2\pi v_z}{\gamma|B|\tan(\theta)} \tag{4.22}$$

where $|B|$ is the magnitude of the magnetic field and θ is the inclination angle of the LOV prism pairs. In Fig. 4.2d the phase and intensity profiles of the polarization state which is correlated with the OAM illustrate the lattice structure. The OAM structure of the resulting beam can be analyzed by looking at the phase profile of the spin state which is correlated with the OAM:

$$\arg\left(\langle\downarrow_z|\Psi^N_{LOV}\rangle\right) = -\tan^{-1}\left[\cot\left(\frac{\pi y}{a}\right)\tan\left(\frac{\pi x}{a}\right)\right]. \tag{4.23}$$

By analyzing Eq. 4.23 it can be observed that the lattice cells are centered on a $\ell_z = 1$ phase structure, while the lattice cell corners are on a $\ell_z = -1$ structure. Although the number (N) of LOV prism pairs does not affect the phase profile, in any lattice cell the number of well defined intensity rings is equal to $N/2$. Therefore, N provides control over the mean radial quantum number n_r in a lattice cell, and even expansions of Eq. 4.18 should be used. Note that using LOV prism pairs which produce different lattice constants results in a "superlattice" which has an overlay of the distinct lattice constants.

Eq. 4.20 shows that a physical shift by a distance, d, of a prism along its incline direction (x or y) results in a simple phase shift of $d\pi/2r_c$ around the corresponding axis. This simplifies the aligning of the prisms.

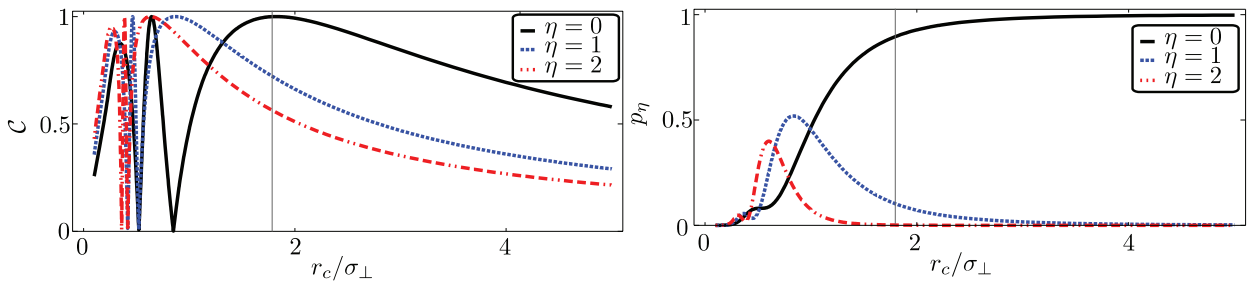

Figure 4.7: Concurrence (on the left) of the spin-orbit state for the filtered $\eta = 0, 1, 2$ subspaces, and the probability (on the right) of the given $\eta = 0, 1, 2$ subspaces. The vertical line at $r_c/\sigma_\perp = 1.82$ corresponds to the point of maximum concurrence for the $\eta = 0$ subspace. Figure taken from Ref. [17].

4.4 Characterization of Neutron Spin-Orbit States

4.4.1 Entanglement in the Spin-Orbit States

A useful measure of entanglement for a bipartite quantum system is the *concurrence*, which is equal to 1 when the entanglement is maximum and 0 when the state is separable. For a bipartite mixed state ρ_{SO}, the concurrence is given by

$$\mathcal{C}(\rho_{SO}) = max\{0, \lambda_1 - \lambda_2 - \lambda_3 - \lambda_4\}, \tag{4.24}$$

where the λ_i's are the eigenvalues, sorted in descending order, of

$$\sqrt{\sqrt{\rho_{SO}}(\sigma_y \otimes \sigma_y)\rho^*_{SO}(\sigma_y \otimes \sigma_y)\sqrt{\rho_{SO}}}, \tag{4.25}$$

and ρ^*_{SO} is the complex conjugate of ρ_{SO}. For a pure state $\rho_{SO} = |\psi_{SO}\rangle\langle\psi_{SO}|$, Eq. (4.24) reduces to

$$\mathcal{C}(|\psi_{SO}\rangle) = \sqrt{2\,(1 - \mathrm{Tr}[\rho_S^2])}, \tag{4.26}$$

where $\rho_S = \mathrm{Tr}_O[|\psi_{SO}\rangle\langle\psi_{SO}|]$ is the reduced density matrix obtained by tracing over the subsystem S (or equivalently tracing could be over subsystem O).

Let us first consider the entanglement of the spin-orbit neutron state in the case where we filter on a single radial quantum number $n_r = \eta$. In this case the renormalized spin-orbit state is a pure state

$$|\psi_\eta\rangle = \frac{1}{\sqrt{p_\eta}}\left(C_{\eta,\ell_{\mathrm{in}},\uparrow}\,|\ell_{\mathrm{in}},\uparrow\rangle + iC_{\eta,\ell_{\mathrm{in}}+1,\downarrow}\,|\ell_{\mathrm{in}}+1,\downarrow\rangle\right), \tag{4.27}$$

where p_η is the probability of the wave packet being in the specific $n_r = \eta$ subspace:

$$p_\eta = C^2_{\eta,\ell_{\mathrm{in}},\uparrow} + C^2_{\eta,\ell_{\mathrm{in}}+1,\downarrow}. \tag{4.28}$$

The concurrence of the $|\psi_\eta\rangle$ and probability coefficients p_η as a function of $r_c/\sigma_\perp$ are shown

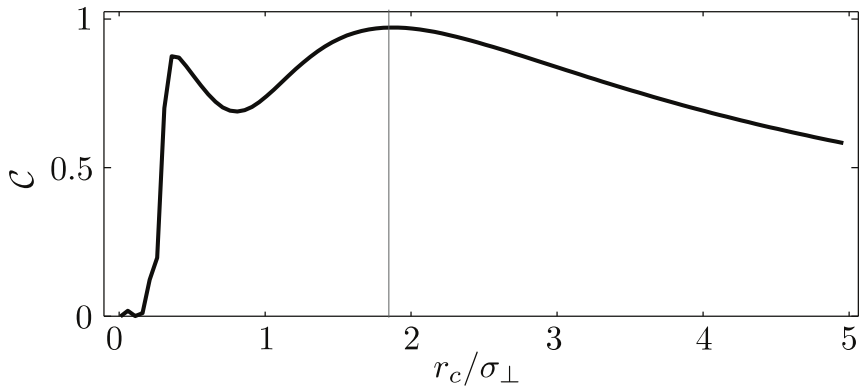

Figure 4.8: Concurrence of the spin-orbit state obtained by tracing the radial subspace. The vertical line at $r_c/\sigma_\perp = 1.82$ corresponds to the point of maximum mixed state concurrence of 0.97. The concurrence does not go to 1 because the traced state is not pure. Figure taken from Ref. [17].

in Fig. 4.7 for the radial subspaces $\eta = 0, 1, 2$. The concurrence of the spin-orbit state obtained by passing through a quadrupole is maximized for the $\eta = 0$ radial subspace when there is a spin flip at ~ 1.82 times the coherence length of the wave packet. This condition is represented by the vertical line in Figs. 4.4, 4.8, and 4.7.

Next we consider the case where the neutron capture cross-section of the detector is independent of the n_r subspace. ^{3}He neutron counting detectors do not distinguish different radial states and so the effect of measurement traces over the radial quantum number. For $n_{r_{\text{in}}} = \ell_{\text{in}} = 0$, the spin-orbit density matrix obtained by tracing over the radial degree of freedom is

$$\rho_{SO} = \sum_{n_r=0}^{\infty} \left[C^2_{n_r,0,\uparrow} \left|0,\uparrow\right\rangle \left\langle 0,\uparrow\right| + iC_{n_r,0,\uparrow} C_{n_r,1,\downarrow} \left|0,\uparrow\right\rangle \left\langle 1\downarrow\right| \right.$$
$$\left. -iC_{n_r,0,\uparrow} C_{n_r,1,\downarrow} \left|1,\downarrow\right\rangle \left\langle 0,\uparrow\right| + C^2_{n_r,1,\downarrow} \left|1,\downarrow\right\rangle \left\langle 1,\downarrow\right| \right]. \tag{4.29}$$

This reduced state is not a pure state ($Tr[\rho^2_{SO}] \neq 1$). The concurrence of this mixed spin-orbit state can be computed using Eq. (4.24) and it is shown in Fig. 4.8. We find that the maximum value of concurrence is $\mathcal{C}(\rho_{SO}) = 0.97$ and it occurs at $r_c/\sigma_\perp = 1.82$. Hence even after averaging over all radial subspaces the spin-orbit state is still highly entangled.

4.4.2 Spin-Orbit Ramsey Experiment

The successful preparation of the entangled state could be verified by using a Ramsey Fringe experiment. For the experiment we require a polarized neutron beam, two quadrupole magnets and a solenoid between them (see Fig. 4.9). The first quadrupole creates the spin-orbit state. The solenoid provides a uniform magnetic field along the spin quantization axis and introduces a phase shift, β, in the spin degree of freedom. The corresponding operator is $U_z(\beta) = \cos(\beta/2)\,\mathbb{1} + i\sin(\beta/2)\,\hat{\sigma}_z$. The second quadrupole can be rotated by angle θ and

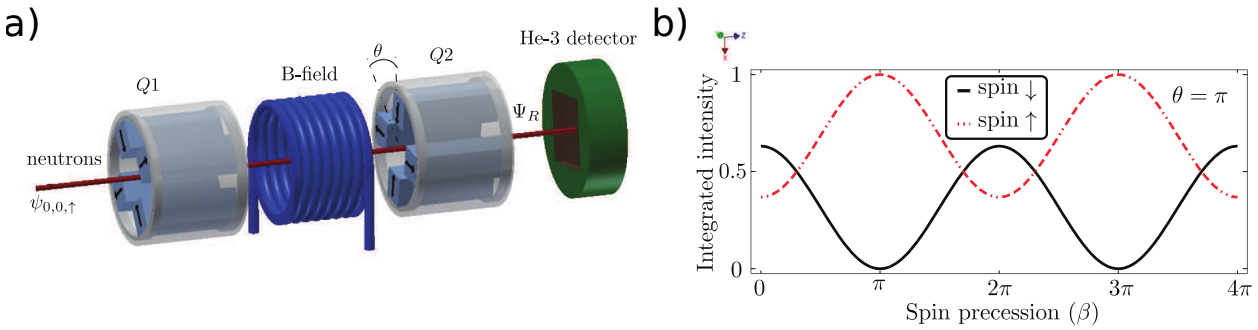

Figure 4.9: a) The setup for the spin-orbit Ramsey fringe experiment. The arrows on the magnets depict the quadrupole geometry. b) The integrated intensity at the output for the spin-up and spin-down neutrons as a function of the spin precession (β) inside the solenoid. The rotation of the second quadrupole is set to $\theta = \pi$. An identical plot can be obtained when $\beta = \pi$ and the quadrupole rotation is varied. This variation of the intensity is an indication of the correlations between the spin and OAM. The phase induced by the spin rotation can be compensated by the rotation of the quadrupole. Figure taken from Ref. [17].

can act as an inverse operator of the first quadrupole:

$$U_{Q2}(\theta) = \cos\left(\frac{\pi r}{2r_c}\right)\mathbb{1} + i\sin\left(\frac{\pi r}{2r_c}\right)\left[e^{-i\theta}l_+\hat{\sigma}_+ + e^{i\theta}l_-\hat{\sigma}_-\right] \tag{4.30}$$

With the setup shown in Fig. 4.9, when the input state is $|0,0,\uparrow\rangle$, the state at the exit (global phase excluded) is

$$\begin{aligned}|\Psi_R\rangle &= U_{Q2}(\theta)U_z(\beta)U_Q\,|0,0,\uparrow\rangle \\ &= \left[\cos\left(\frac{\pi r}{r_c}\right)\cos\left(\frac{\beta-\theta}{2}\right) - i\sin\left(\frac{\beta-\theta}{2}\right)\right]|0,0,\uparrow\rangle \\ &\quad - i\sin\left(\frac{\pi r}{r_c}\right)\cos\left(\frac{\beta-\theta}{2}\right)e^{i\phi}\,|0,0,\downarrow\rangle\end{aligned} \tag{4.31}$$

The integrated intensities at the output are

$$\begin{aligned}\overline{I_\uparrow}(\beta,\theta) &= \int_0^\infty dr\int_0^{2\pi} d\phi\; r\,|\langle\uparrow|\Psi_R\rangle|^2 \\ &= 1 - \frac{\pi\sigma_\perp}{r_c}F\left(\frac{\pi\sigma_\perp}{r_c}\right)\cos^2\left(\frac{\beta-\theta}{2}\right)\end{aligned} \tag{4.32}$$

$$\begin{aligned}\overline{I_\downarrow}(\beta,\theta) &= \int_0^\infty dr\int_0^{2\pi} d\phi\; r|\langle\downarrow|\Psi_R\rangle|^2 \\ &= \frac{\pi\sigma_\perp}{r_c}F\left(\frac{\pi\sigma_\perp}{r_c}\right)\cos^2\left(\frac{\beta-\theta}{2}\right),\end{aligned} \tag{4.33}$$

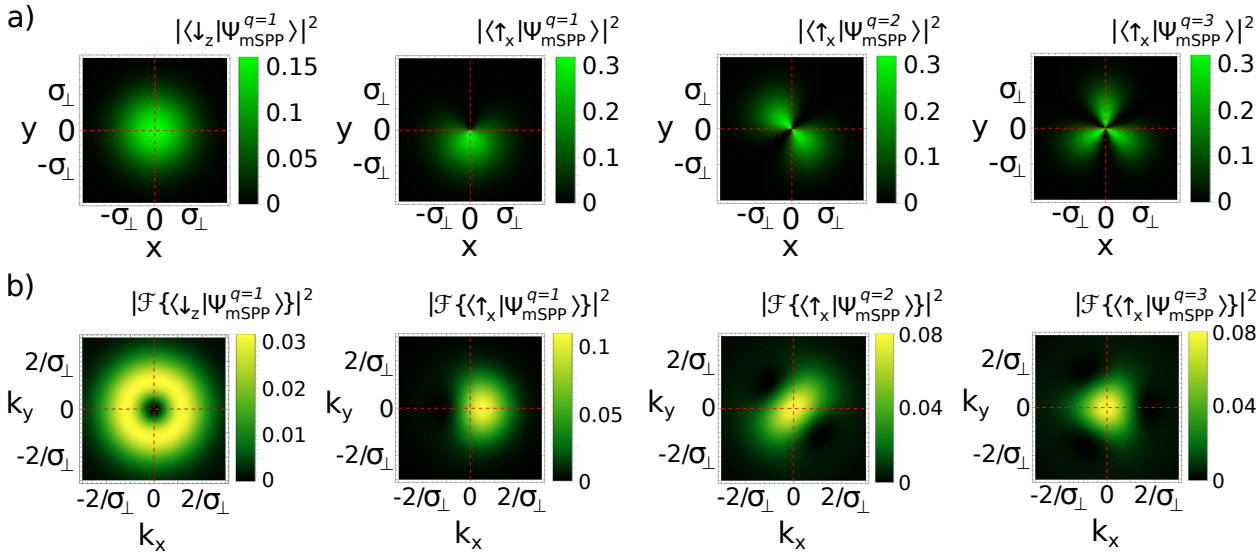

Figure 4.10: $\Delta\ell = |\ell_{\uparrow_z} - \ell_{\downarrow_z}|$ of spin-orbit states can be determined by mixing the two spin states and obtaining the a) 2D intensity profile or b) 2D momentum distribution. We set $\ell_{\downarrow_z} = 0$ so that $q = \Delta\ell$. By mixing the two spin eigenstate carrying different OAM, the OAM difference manifests itself as an asymmetry in the 2D intensity profile and the 2D momentum distribution profile. Without spin mixing, that is projecting onto $|\downarrow_z\rangle$, the 2D profiles show no azimuthal nodes. With spin mixing, that is projecting onto $|\uparrow_x\rangle$, the number of azimuthal nodes is equal to q. Figure taken from Ref. [18].

where $F(\pi\sigma_\perp/r_c)$ is Dawson's integral. The integrated spin intensities at the output Eq. 4.32 and 4.33 show the same behaviour if β is varied for fixed θ, and if θ is varied for fixed β. The fact that the phase induced by the spin rotation can be compensated by the rotation of the orbital state is an indication of the spin-orbit entanglement. The bottom part of Fig. 4.9 displays the spin-dependent integrated intensity for β varied with $\theta = \pi$ and with $r_c/\sigma_\perp = 1.82$. Note that the amplitude of the oscillations of the integrated intensity is not 1 because the spin-orbit state obtained by tracing the radial degree of freedom is not pure.

4.4.3 Intensity Correlations

The two paths of a Mach-Zehnder interferometer are isomorphic to a two-level quantum system such as the spin$-1/2$ DOF. Therefore after a mixing in the spin DOF, the spin dependent 2D intensity profiles will possess a helical structure which quantifies the induced OAM. For simplicity consider the spin-orbit state $|\Psi^q_{\text{mSPP}}\rangle$ (Eq. 4.6). The two-dimensional intensity, post-selected on a particular spin direction $|s\rangle$, is given by

$$I(x, y) = |\langle s|\Psi^q_{\text{mSPP}}\rangle|^2 \tag{4.34}$$

Without spin mixing, i.e. post-selecting on $|\uparrow_z\rangle$ or $|\downarrow_z\rangle$, the resulting 2D intensity profile is a Gaussian in both cases, which does not reveal any OAM structure.

To determine the induced OAM on the $|\downarrow_z\rangle$ component we would need to post-select

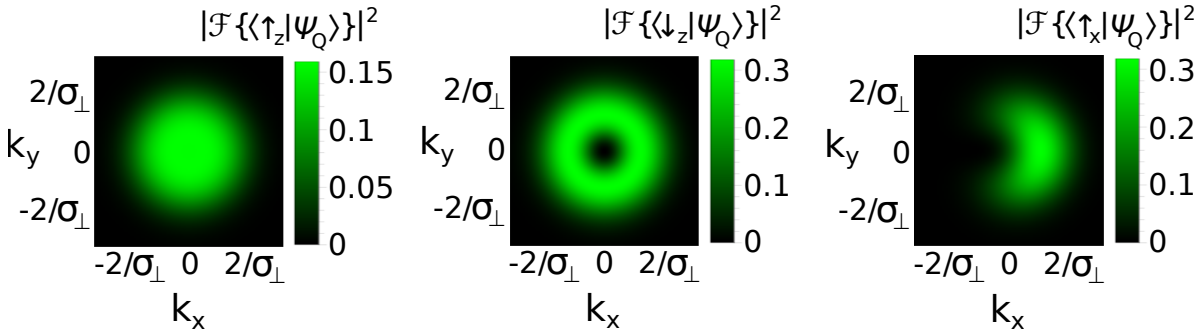

Figure 4.11: Spin dependent momentum distribution of $|\Psi_Q\rangle$. Except for the magnetic SPP, the other methods shown in Fig. 4.2 produce radial diffraction in addition to the azimuthal diffraction. However this does not change the described azimuthal asymmetry used to characterize the spin-orbit states. In comparison to Fig. 4.10 the azimuthal asymmetry is even more pronounced, as shown in this figure for the case of the spin-orbit state prepared via a quadrupole magnetic field.

on a perpendicular spin direction. The 2D intensity profiles projected onto $|\uparrow_x\rangle$, given by $|\langle\uparrow_x|\Psi^q_{\text{mSPP}}\rangle|^2$, are shown in Fig. 4.10a for magnetic SPPs with $q = 1, 2, 3$. These are identical to the expected profiles obtained via the interferometric measurement described above.

The order of rotational symmetry of the 2D intensity profiles is equal to $|\Delta\ell| = |\ell_\uparrow - \ell_\downarrow| = |q|$. Applying a spin rotation along $\hat{\sigma}_z$ before the spin mixing effectively rotates the resulting 2D intensity profile. The direction of rotation determines the sign of q. The initial azimuthal offset determines β at the detector.

4.4.4 Momentum Correlations

Another method to characterize spin-orbit states is to measure their 2D momentum distribution. The 2D momentum distribution, post-selected on a particular spin direction $|s\rangle$, is given by

$$P(k_x, k_y) = |\mathcal{F}\{\langle s|\Psi^q_{\text{mSPP}}\rangle\}|^2 \tag{4.35}$$

where $\mathcal{F}\{...\}$ is the Fourier transform. If we apply spin filters along the spin eigenbasis of $|\Psi^q_{\text{mSPP}}\rangle$, i.e. along $|\uparrow_z\rangle$ or $|\downarrow_z\rangle$, then the 2D momentum distribution of $\langle\uparrow_z|\Psi^q_{\text{mSPP}}\rangle$ would be a Gaussian profile indicative of the prepared incoming state carrying no OAM, and that of $\langle\downarrow_z|\Psi^q_{\text{mSPP}}\rangle$ would be a ring shape. However, the ring-shaped momentum distribution does not uniquely define an OAM beam; for example, it is possible to have a radially diverging beam which has a ring-shaped 2D momentum distribution.

If we post-select on a perpendicular spin axis then the spin-orbit coupling breaks the symmetry of the 2D momentum distribution profile as shown in Fig. 4.10b. Therefore we propose a method to characterize the spin-orbit states by mapping out their 2D momentum distribution after spin filtering along a perpendicular spin axis.

In this method as well, the order of rotational symmetry of the 2D momentum profiles is equal to $|\Delta\ell| = |\ell_\uparrow - \ell_\downarrow| = |q|$. Applying a spin rotation along $\hat{\sigma}_z$ before the spin mixing

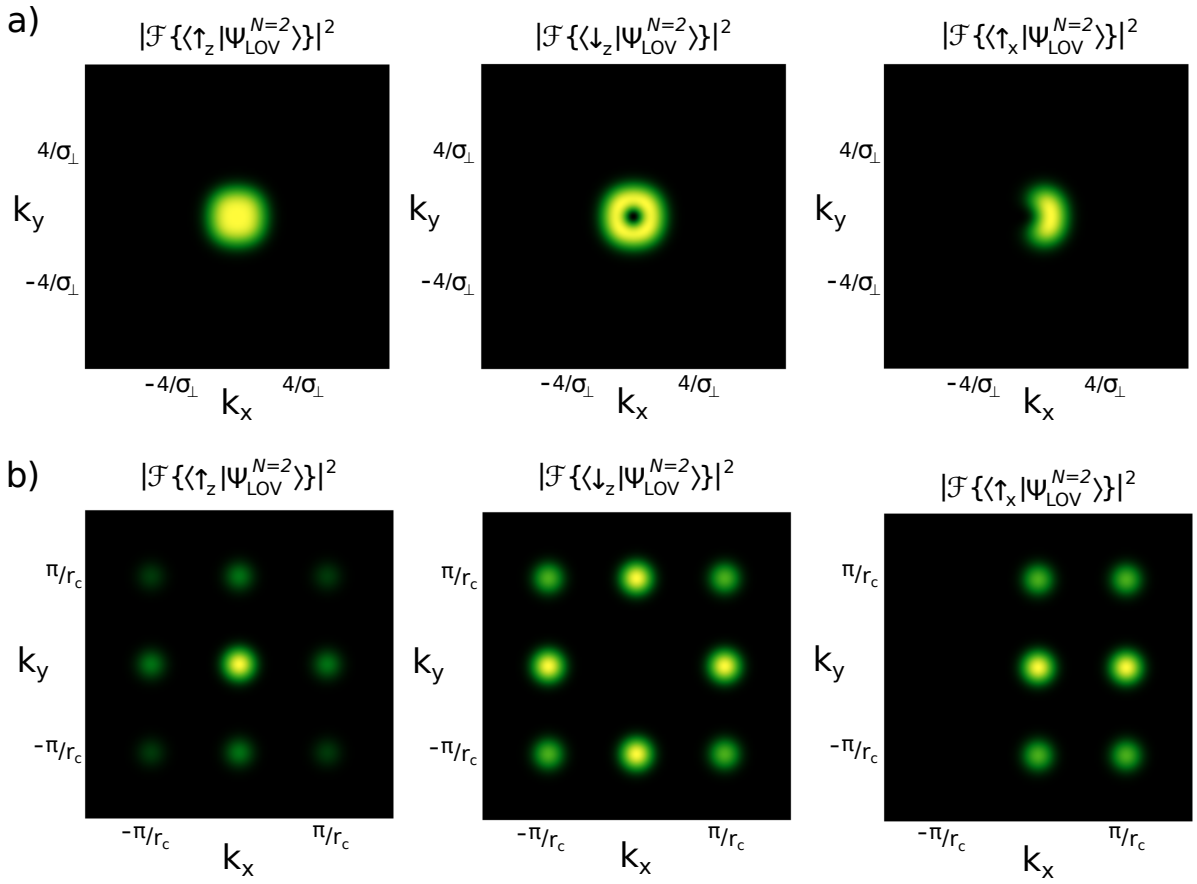

Figure 4.12: Spin dependent momentum distribution of the $|\Psi_{\text{LOV}}^{N=2}\rangle$ when the beam is composed of a) one lattice cell where $r_c = 1.82\sigma_\perp$ b) multiple lattice cells. The plots show that each lattice cell of the $|\Psi_{\text{LOV}}^{N=2}\rangle$ beam carries spin dependent OAM, but the beam which composed of many lattice cells does not carry OAM. The plots in b) also describe the spin dependent intensities of the $|\Psi_{\text{LOV}}^{N=2}\rangle$ beam in the far-field. Lastly, it should be noted that both cases a) and b) possess azimuthal symmetry in their momentum distribution which can be used to characterize the spin dependent OAM of each lattice cell.

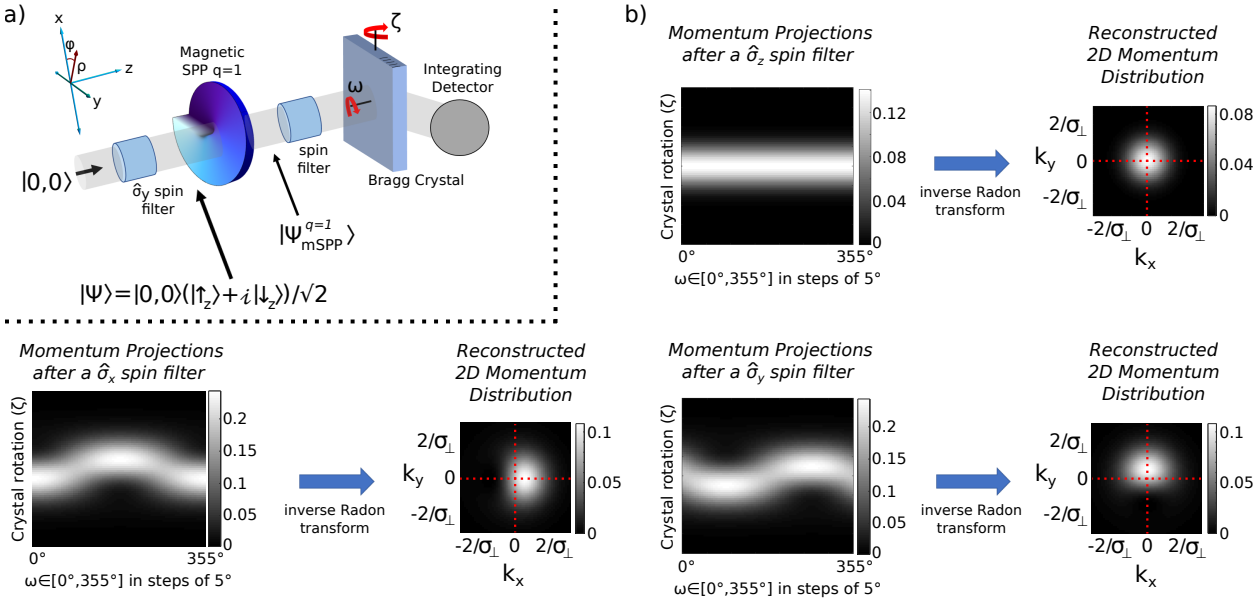

Figure 4.13: When post-selecting onto a perpendicular spin eigenbasis of a spin-orbit state the OAM manifests itself as an asymmetry in the 2D momentum distribution (see Fig. 4.10). a) Proposed experiment to map out the 2D momentum distribution of a neutron spin-orbit state by measuring the momentum projections via a Bragg crystal. This allows for analysis of the beam's OAM components by mapping out the momentum distribution. b) We may assemble the momentum projections at each ω obtained by rotating the Bragg crystal around the crystal plane direction. The 2D momentum distribution is obtained from the projection curves via the inverse Radon transform. In the examples depicted we perform the inverse Radon transform on 36 equally spaced slices of $\omega \in [0°, 175°]$ and reconstruct the 2D momentum distribution. Figure taken from Ref. [18].

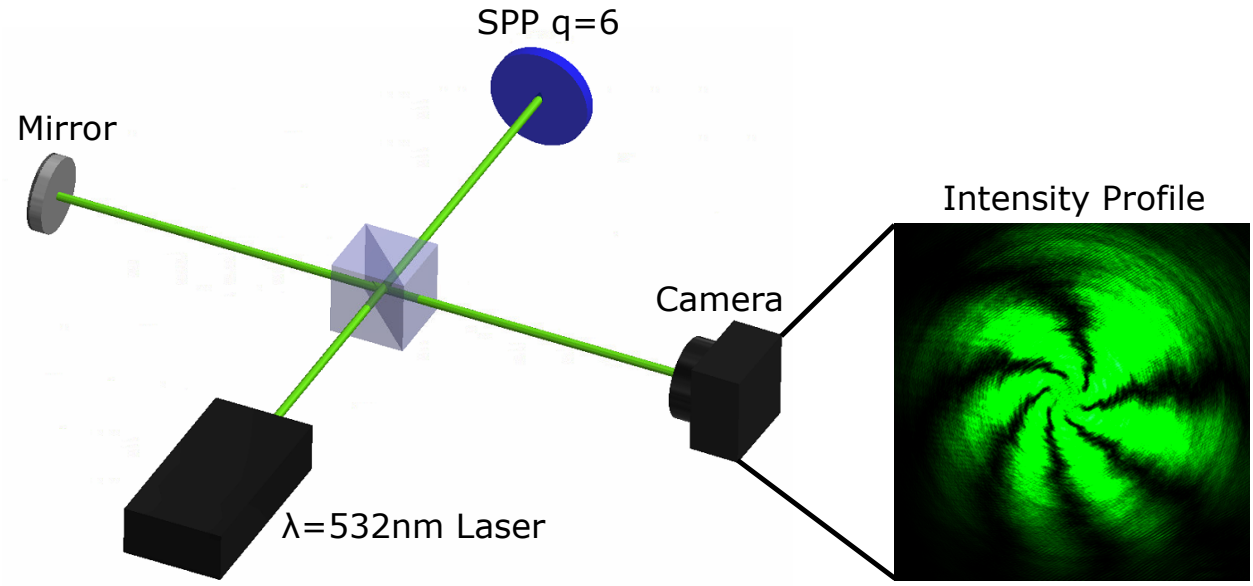

Figure 4.14: Optical Michelson interferometer where the sample is the polished aluminum SPP. Here we characterize the action of an SPP which in reflection mode acts as a $q = 6$ for $\lambda = 532$ nm light. The helical phase structure is clearly visible.

effectively rotates the resulting 2D momentum profile. The direction of rotation determines the sign of q. The initial azimuthal offset determines β at the detector.

Allowing a state to propagate into the far-field, where the intensity profile is indicative of the momentum distribution profile, is not practical with the small neutron diffraction angles induced by the OAM. A more practical method is to use a diffracting crystal and obtain momentum projection curves which can then be used to reconstruct the 2D momentum distribution. A proposed experiment is shown in Fig. 4.13a. A spin-orbit state is prepared by passing a coherent superposition of the two spin eigenstates through a magnetic SPP. The spin is then projected onto a perpendicular spin direction using a spin filter. A rotatable Bragg crystal enables a measurement of the momentum projected to the crystal plane direction. The two rotation angles ω and ζ effectively allow us to obtain the projections of the 2D momentum distribution along an arbitrary angle in the transverse plane, as shown in Fig. 4.13b. A standard problem of medical imaging, obtaining the "backprojection image" (2D momentum distribution) via the "sinogram" (projection curves) is achieved with the inverse Radon transform [148]. Fig. 4.13b shows the reconstructed image obtained via 36 equally spaced projections. Note that because of the azimuthal symmetry of the spin-orbit state, rotating the spin filter of Fig. 4.13a by an angle ω and fixing the Bragg crystal orientation produces the same outcome as shown in Fig. 4.13b.

These procedures work similarly if the spin-orbit state is created via any method depicted in Fig.4.2. Note that other than the magnetic SPP, the other methods produce radial diffraction in addition to the azimuthal diffraction. However this does not change the described azimuthal asymmetry used to characterize the spin-orbit states. In fact, the asymmetry becomes even more pronounced. Fig. 4.11 and Fig. 4.12 show the spin dependent momentum distribution of $|\Psi_{\mathrm{Q}}\rangle$ and $|\Psi_{\mathrm{LOV}}^{N=2}\rangle$ respectively. Therefore we proposed that an initial exper-

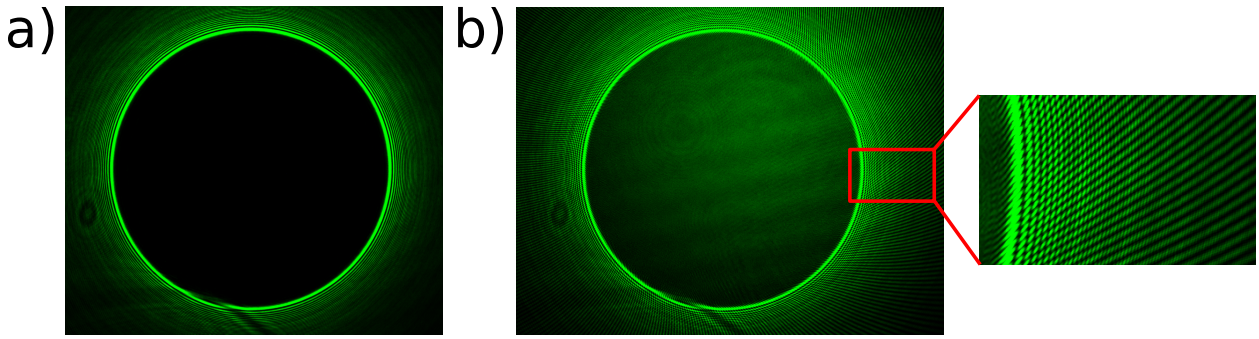

Figure 4.15: The measured a) far-field intensity profile, and b) phase profile measured via the Michelson interferometer of Fig. 4.14, of the $\ell = 420$ optical OAM beam. The ring shape intensity profile and the helical phase structure are clearly visible. The aluminum SPP used to create this optical OAM beam in reflection mode, would act as a $q = 1$ SPP for $\lambda = 0.271$ nm neutrons in transmission mode.

iment be done with LOV prism pairs to maximize the use of the incoming beam flux and circumvent problems with small coherence lengths.

4.5 Lattices of Optical Spin-Orbit states

4.5.1 Optical OAM

As the methods of generating neutron lattices of spin-orbit states are based on a general model we can demonstrate the power of these protocols on photon beams by producing a lattice of states where polarization and OAM are correlated. This can be achieved because there is an isomorphism between the Bloch sphere representing the spin states of fermions and that of the Poincaré sphere representing the polarization states of light (see section 1.5).

It is illustrative to see the complementarity between the optical system and the neutron system. Consider the aluminum SPPs used in the neutron OAM and holography experiments (see section 3.4 and section 3.5). In those experiments the neutron passed through the aluminum SPP and acquired an azimuthal phase profile indicative of OAM. However, light would reflect from the polished aluminum SPPs instead of passing through them. Therefore in this case it is convenient to use a Michelson interferometer to image the induced phase profile. Fig. 4.14 shows the experiment with a SPP whose phase step thickness of 1.6 μm induces $\ell = 6$ onto the $\lambda = 532$ nm reflected light.

Optics also allow us to explore higher order OAM beams. Consider an aluminum SPP with thickness 112 μm which acts as a $q = 1$ SPP for $\lambda = 0.271$ nm neutrons. For $\lambda = 532$ nm light reflecting from its surface it acts as a $q = 420$ SPP. Fig. 4.15a is the resulting intensity distribution in the far-field. The intensity is ring shaped as expected. Placing this SPP into the Michelson interferometer of Fig. 4.14 produces the images shown in Fig. 4.15b. Here we see the tangential interference fringes quantifying the induced OAM.

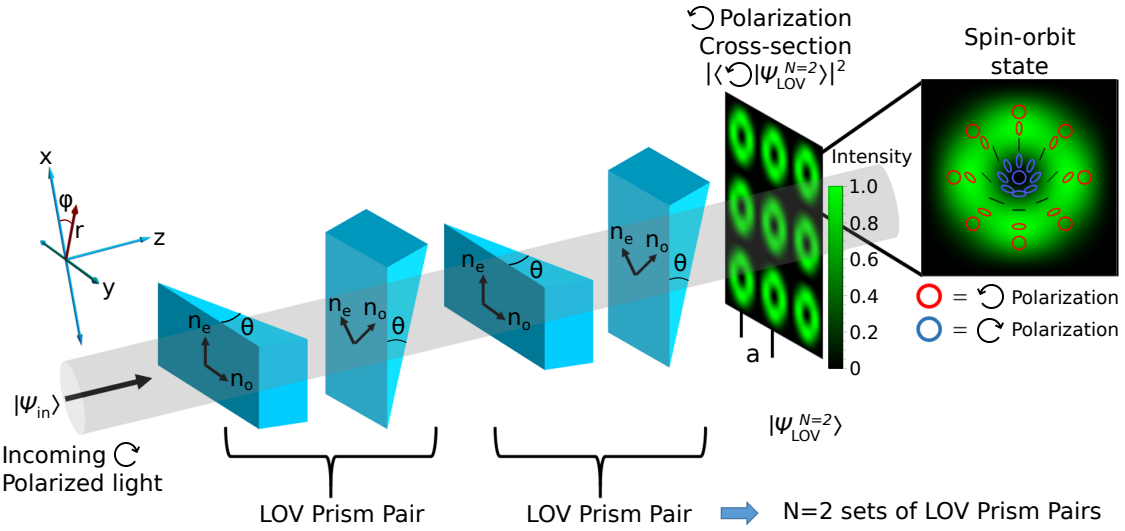

Figure 4.16: The lattices of optical spin-orbit beams are produced by passing a circularly polarized light beam through N sets of Lattice of Optical Vortices (LOV) prism pairs. A LOV prism pair consists of two perpendicular optical birefringent prisms where one prism has the optical axis along the prism incline and the second prism has the optical axis offset by 45°. The lattice constant is given by $a = \lambda/(n_e - n_o)\tan(\theta)$, where θ is the prism incline angle, n_e and n_o are the extraordinary and ordinary refractive indices, and λ is the wavelength of the incoming light. Figure taken from Ref. [19].

4.5.2 Preparation of Optical LOV Beams

Similar to Eq. 3.2 the eigenstates in cylindrical coordinates (r, ϕ) for polarized light can be expressed as

$$|n_r, \ell, p\rangle = \mathcal{N}\xi^{|\ell|}e^{-\frac{\xi^2}{2}}\mathcal{L}_{n_r}^{|\ell|}\left(\xi^2\right)e^{i\ell\phi}Z(z)\,|p\rangle\,, \tag{4.36}$$

where where $\mathcal{N} = \frac{1}{\sigma_\perp}\sqrt{\frac{n_r!}{\pi(n_r+|\ell|)!}}$ is the normalization constant, $\xi = r/\sigma_\perp$ is the dimensionless radial coordinate, ϕ is the azimuthal coordinate, $n_r \in \{0, 1, 2...\}$ is the radial quantum number, $\ell \in \{0, \pm1, \pm2...\}$ is the azimuthal quantum number, $\mathcal{L}_{n_r}^{|\ell|}\left(\xi^2\right)$ are the associated Laguerre polynomials, $Z(z)$ is the longitudinal wave function often approximated by a Gaussian wave packet, and $p \in \{\circlearrowleft, \circlearrowright\}$ is the polarization state of light.

Consider the optical spin-orbit state:

$$|\Psi_{SO}\rangle = \frac{e^{-\frac{r^2}{2}}}{\sqrt{\pi}}\left[\cos\left(\frac{\pi r}{2r_c}\right)|\circlearrowleft\rangle + ie^{i\phi}\sin\left(\frac{\pi r}{2r_c}\right)|\circlearrowright\rangle\right], \tag{4.37}$$

where we have set $\sigma_\perp = 1$. $|\Psi_{SO}\rangle$ describes a vector vortex beam where the OAM is induced via Pancharatnam-Berry geometrical phase. The intensity (post-selected on the right circularly polarized light) and the polarization distribution (before the polarization

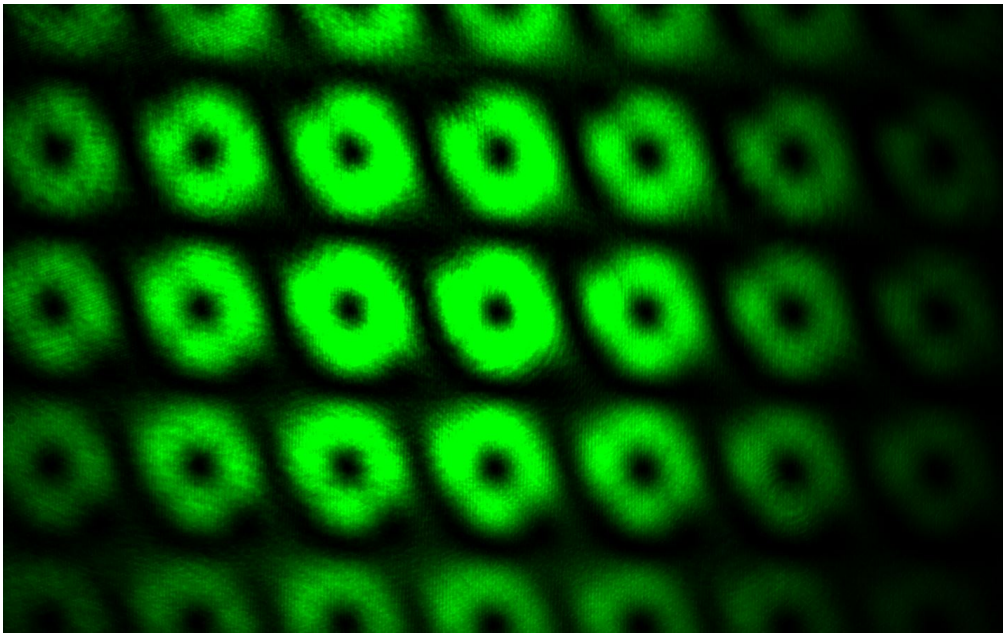

Figure 4.17: Intensity profile at the camera of $|\Psi_{\mathrm{LOV}}^{N=2}\rangle$ optical beam, where we have postselected on the polarization state which is correlated with the OAM.

post-selection) are depicted on the zoomed-in plot of Fig. 4.16.

Our proposed procedure for producing a beam with a lattice of optical spin-orbit states consists of a sequence of linear birefringent gradients that are equal in magnitude and perpendicular to each other and the polarization axis of the incoming light. Examining and truncating the right-hand side of Eq. 4.18, we see that it can be interpreted as a sequence of N perpendicular linear gradients.

In the case of photons one way to produce the linear gradients is via optical birefringent prisms as shown in Fig. 4.16. Placing one prism with an optical axis along the prism incline and a second prism with an optical axis offset by 45° results in the product operation $(\hat{U}_{0,0}\hat{U}_{\frac{\pi}{2},\frac{\pi}{2}})$. We had termed such a set a "Lattice of Optical Vortices (LOV) prism pair".

This process is shown in Fig. 4.16 for $N = 2$ sets of LOV prism pairs. The spin-orbit states in these lattices form a two-dimensional array with a lattice constant of

$$a = \frac{\lambda}{\Delta n \tan(\theta)} \tag{4.38}$$

where Δn and θ are the birefringence and the incline angle of the LOV prism pairs. As mentioned in section 4.3.5 the number of LOV prism pairs N provides control over the mean radial quantum number n_r in a lattice cell, and even expansions of Eq. 4.18 should be used. In the $N = 1$ case both polarization states are similarly coupled to the OAM forming vortex-antivortex structures, and both $\ell_z = 1$ and $\ell_z = -1$ phase structures are illuminated. Similar vortex-antivortex structures can also be obtained via Wollaston prisms [149, 150].

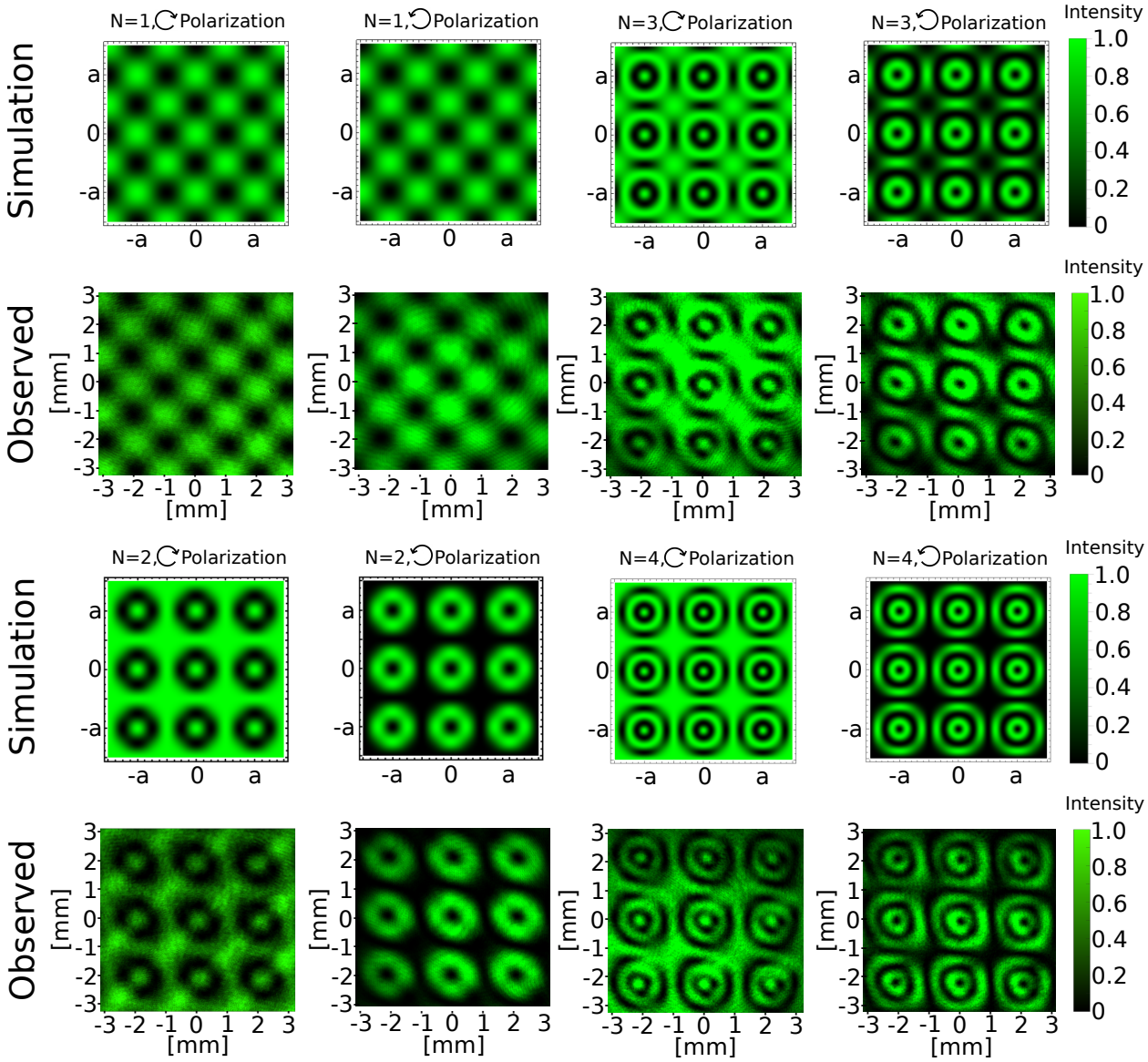

Figure 4.18: Intensity profiles post-selected on a particular polarization state of the lattices of optical spin-orbit beams. Top two rows are the simulated the observed images for odd N, while the bottom two rows are the simulated the observed images for even N. The lattice constant specified by Eq. 4.38 for $\lambda = 532$ nm light and our 2° quartz LOV prism sets is $a = 1.68$ mm; the measured lattice constant at the camera being slightly larger due to beam divergence. If desired, the lattice constant can easily be pushed into the μm-range by fabricating prisms with a larger incline angle out of a high birefringent material such as TiO_2. Figure taken from Ref. [19].

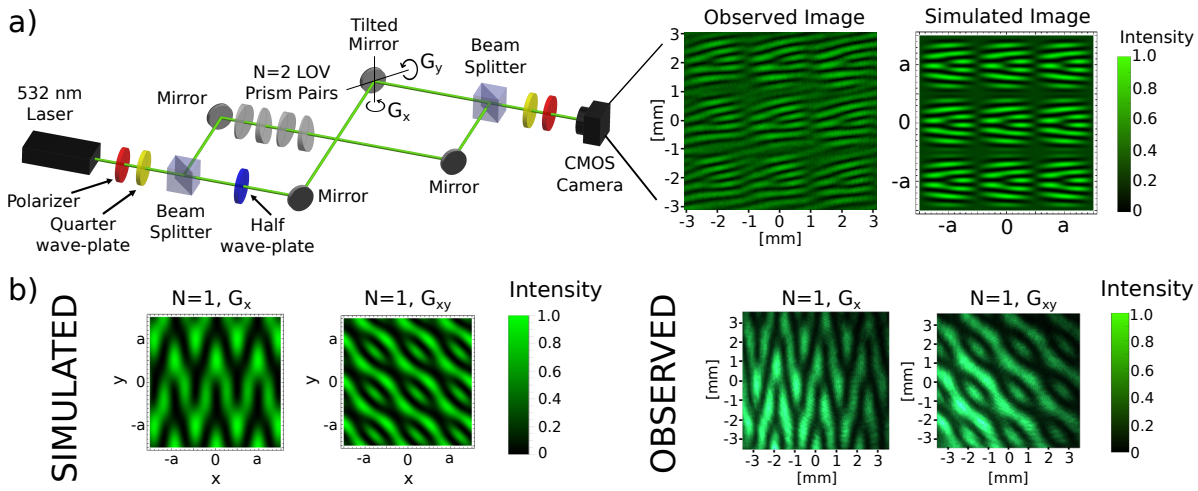

Figure 4.19: a) Phase imaging of the $N = 2$ lattice of optical spin-orbit beams where we post-select on the polarization carrying the OAM. The $N = 2$ sets of LOV prism pairs are placed in one path of the interferometer and a linear phase gradient is applied in the other path ($G_y \sim 20$ rad/mm) by tilting a mirror in order to pronounce the well known fork structure holograms in the lattice, which indicate the presence of OAM beams. Figure taken from Ref. [19]. b) Phase imaging of the $N = 1$ case in which both polarization states are similarly coupled to the OAM, and both $\ell_z = 1$ and $\ell_z = -1$ phase structures are illuminated. Furthermore, as shown the phase profile structure depends on the direction of the applied phase gradient (where $G_x \sim 5$ rad/mm and $G_{xy} \sim -6.8$ rad/mm).

4.5.3 Experimental Methods

In the following experimetns a laser of wavelength 532 nm was used, along with standard polarizers, wave-plates, and optical components. The LOV prism pairs were circular quartz wedges (birefringence of ~ 0.0091) with a wedge angle of 2° and diameter of 2.54 cm. One wedge had the optical axis aligned with wedge angle while the other wedge had the optical axis aligned 45° to wedge angle.

For images shown in Fig. 4.18 the setup consisted of a laser, a linear polarization filter, a quarter-wave plate, N LOV prism pairs, a quarter-wave plate, a linear polarization filter, and a CMOS camera. For beam phase imaging shown in Fig. 4.19, a four-mirror interferometer [151] was used because it allowed for compensation of the beam deviation due to the LOV prism pairs. An alternative method would have been to add a non-birefringent prism after each prism of the LOV prism pair in order to compensate for the beam deviation. A linear phase gradient in Fig. 4.19 was introduced to obtain the fork structure holograms by tilting the mirror of the interferometer path which did not contain the LOV prism pairs.

4.5.4 Characterization of Optical LOV Beams

Fig. 4.17 shows the typical intensity profile at the camera of the $|\Psi_{\text{LOV}}^{N=2}\rangle$ optical beam, where we have postselected on the polarization state which is correlated with the OAM. For the following analysis we will select a three by three lattice. The simulated and observed polarization profiles for $N = 1, 2, 3, 4$ are plotted in Fig. 4.18, and are in a good agreement.

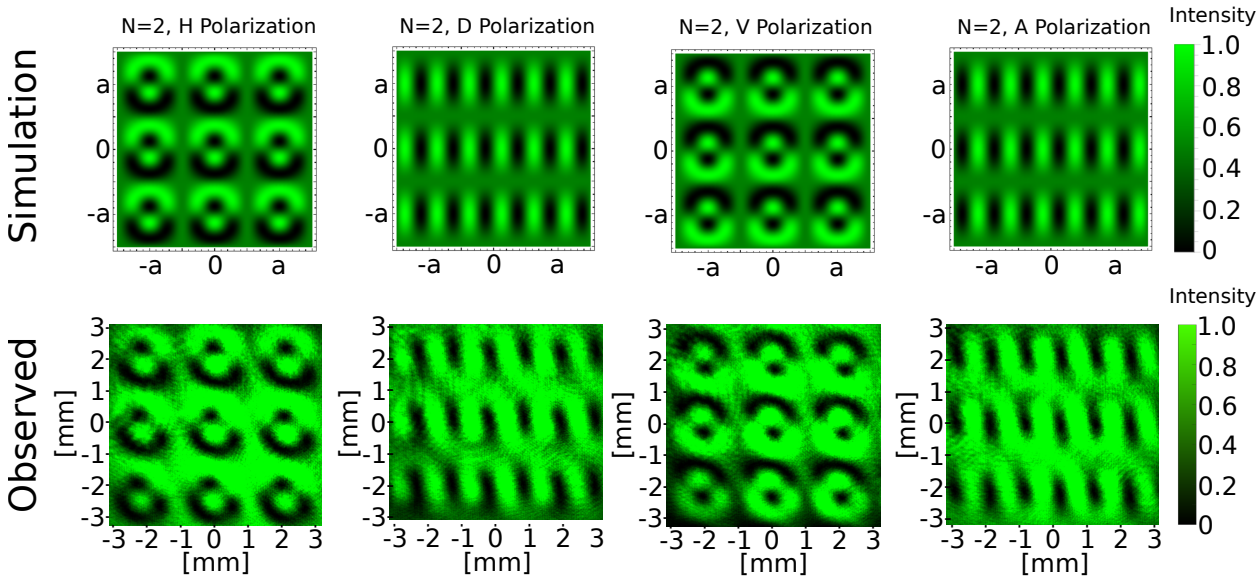

Figure 4.20: By postselecting on linear polarization the intensity profile shows an asymmetry indicative of the spin-orbit state in each lattice cell. Shown are the intensity profiles post-selected on a particular polarization state of the N=2 lattices of optical spin-orbit beams. Top row shows the simulated images the bottom row shows the observed images.

For our LOV prism pairs the lattice constant given by Eq. 4.38 comes out to be 1.68 mm, though it was measured to be slightly larger due to beam divergence.

The period of the lattice can span a large range. LOV prism pairs fabricated from TiO_2 (birefringence of ~ 0.29) with an incline angle of 60° would produce a lattice period of $a \sim 1$ μm for a light wavelength of 532 nm. Furthermore, if birefringent materials which exhibit the Pockel's effect are used then with the addition of external electric field control a variable period may be obtained via the electro-optic effect.

The ring structure intensity shown in Fig. 4.18 is indicative of the polarization profile of the spin-orbit state (Eq. 4.37) and not the OAM structure. To show that there is a lattice of OAM states we measure the phase profile of the beam using an interferometer. The schematic of the setup is shown in Fig. 4.19a where a linear phase gradient in one path has been introduced to observe the characteristic fork structure hologram indicative of OAM. A lattice of fork structures can clearly be seen, indicating an $\ell_z = 1$ at each lattice center. In the $N = 1$ case both polarization states are similarly coupled to the OAM, and both $\ell_z = 1$ and $\ell_z = -1$ phase structures are illuminated. This can be observed on Fig. 4.19b.

As described in section 4.4.3, when postselecting on perpendicular polarization eigenbasis the intensity profile shows an asymmetry indicative of the spin-orbit state in each lattice cell. Fig. 4.20 shows the intensity profiles post-selected on a particular linear polarization state of the N=2 lattices of optical spin-orbit beams.

4.5.5 Characterizing Materials with Optical LOV Beams

Sets of LOV prism pairs can be used to construct a Ramsey interferometer which is capable of measuring the 2D linear and circular birefringence of materials. This is the 2D extension

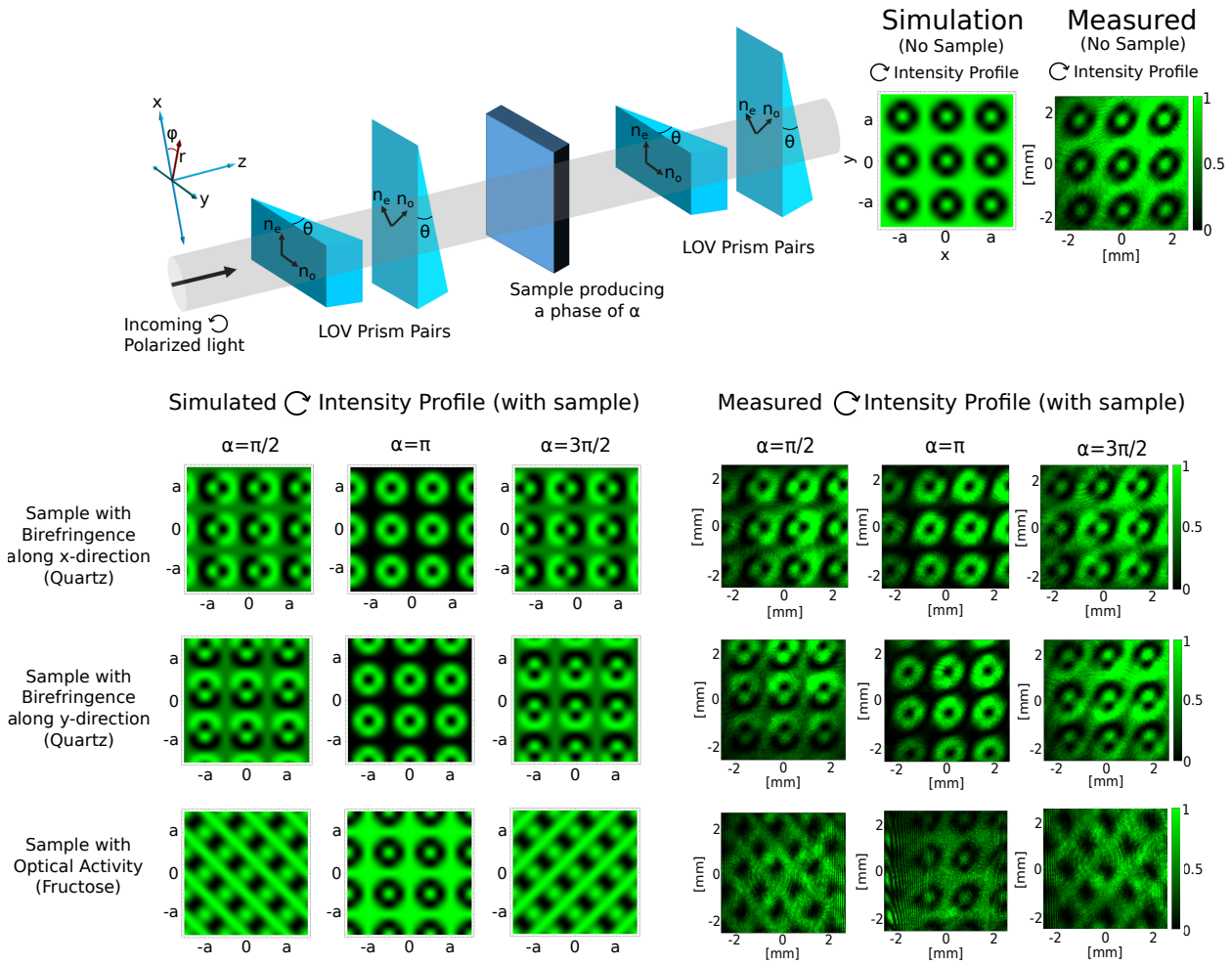

Figure 4.21: Ramsey interferometer for the mapping of the 2D linear and circular birefringence. A sample is placed between two sets of LOV prisms. The intensity pattern at the camera is modified according to the direction and magnitude of the induced phase. A slab of quartz was used the linear birefringent sample and a solution of fructose and water for the optical activity sample.

of the interferometric measurement procedure described in section 4.4.2.

Fig. 4.21 shows the simulated and observed profiles when a sample with uniform phase is placed inside the interferometer. The intensity pattern at the camera is modified according to the direction and magnitude of the induced phase. The resolution in these measurements is set by the lattice constant of the LOV beam.

A quartz sample was used for the birefringent sample and a solution of fructose and water for the optical activity sample. The quartz sample was rotated to vary the phase. For the circular birefringence measurements concentration of fructose in water was varied.

4.5.6 Conclusion

This chapter has introduced and quantified new methods of preparing neutron spin-orbit states. This is a step towards general programming of the spin and quantum phase of neutron wavefronts, which addresses the fundamental limitations of neutron scattering and imaging techniques. For example, recent interest in complex topological and quantum materials [152, 153] suggests a need for a tool with unique penetrating abilities and magnetic sensitivity. Analysis of material properties could be performed using a neutron spin-orbit lattice where the lattice constants are matched to the characteristic length scales of materials. The methods described here allow for the direct control of spin-orbit state parameters within a neutron beam. Furthermore, a method is proposed to characterize neutron spin-orbit states which overcomes the main challenges associated with low neutron flux and the neutron's small spatial coherence length.

The described protocols provide a two-dimensional control of the characteristic length scale of the single spin-orbit features. It may be possible to create a lattice of ring-shaped optical atomic traps, individual instance of which have figured prominently in recent studies of atomtronic circuits [154]. One can also envisage vortex pinning in Bose-Einstein condensates via these beams [155]. Lattices of polarization coupled optical vortices may also be fruitful in microscopy or basic studies of the interaction of structured light [100–103] with individual atoms or molecules. This is because OAM is defined with respect to a single axis perpendicular to the wavefront. Thus, in studies using a single OAM axis, only atoms or molecules in the region of a fraction of a wavelength about that axis are subject to the OAM selection rules [139, 156]. This technique extends those rules across a region proportional to the area of the fully-structured wavefront.

Chapter 5

Conclusion and Future Prospects

This thesis described several projects which are under the common theme of generating and manipulating the quantum phase structure of matter waves and electromagnetic waves. These results have contributed to the fields of: perfect crystal neutron interferometry, grating based neutron interferometry, and matter wave and optical structured waves.

Chapter one provides a theoretical framework which is required for rest of the thesis. In addition, the chapter briefly covers the construction of a new beamline at the National Institute of Standards and Technology's Center for Neutron Research dedicated to quantum information related neutron interferometry experiments. The new beamline now provides environmental and temperature isolation for the NIs, and a cryostat has been incorporated into the setup.

Chapter two described the development and characterization of far-field phase-grating moiré neutron interferometry. A two phase-grating moiré neutron interferometer has been demonstrated, and it has been employed for the measurement of the microstructure of a sample. Furthermore, a three phase-grating moiré neutron interferometer has been demonstrated. This novel technique has proven to be advantageous over the other neutron interferometry setups in terms of broader wavelength acceptance and less stringent alignment requirements.

Chapter three focused on the experiments relating to neutron orbital angular momentum (OAM). The first demonstration of the control of neutron OAM and the first use of the perfect crystal neutron interferometer to perform holography of a macroscopic sample were described. These methods provide a new tool for interferometric testing of neutron optics and the characterization of coherence of neutron beams.

Chapter four focused on the theory and experiments dealing with neutron and optical spin correlated OAM (spin-orbit) states. Methods to prepare neutron spin-orbit states via special geometries of magnetic fields were presented. The preparation, entanglement characterization, and proposed experimental verification of such states are described in detail. The chapter then introduces and describes a novel method capable of preparing lattices of optical and neutron spin-coupled OAM states. Lastly, the experimental demonstration and characterization of optical lattices of spin-orbit states is described in detail.

5.1 Future Work

- The new beamline at the National Institute of Standards and Technology's Center for Neutron Research dedicated to quantum information related neutron interferometry experiments is now operational. Spin elements were installed and optimized, and a cryostat has been incorporated into the setup. The future work on this beamline will include the characterization of magnetic phase transitions of materials which occur at low temperatures.

- The achieved contrast of 3% of the three phase-grating moiré neutron interferometer was well below the theoretical expectation of 30%, and it was determined that the phase-gratings are sub-optimal. Higher quality phase-gratings will need to be fabricated for the next set of experiments. Furthermore, to increase the expected contrast above 30% triangular sloped gratings will be used in order to reduce the intensity of the higher order diffraction peaks. Lastly, gratings fabricated from magnetic materials will be made and characterized in order to introduce a correlation between the spin degree of freedom and the diffraction orders.

- The future prospects for the three phase-grating moiré neutron interferometer are the characterization of materials with large autocorrelation lengths, and the measurements of the gravitational constants "g" and "G". The current CODATA recommended value of G consists of several discrepant experimental results, and there is a need for a high precision measurement.

- In the area of neutron spin-orbit states, the next step will be to demonstrate lattices of neutron spin-orbit states via the LOV prim pairs. The neutron LOV beams will be characterized by mapping out the spin dependent intensity correlations to avoid the need of incorporating the LOV prisms into the perfect crystal neutron interferometer.

- Neutrons are a convenient probe of materials due to their relatively large mass, electric neutrality, and sub-nanometer-sized wavelengths. Once the lattices of neutron spin-orbit states are demonstrated, it is expected that these unique beams are used as a probe of chiral and helical materials. In particular, the aim is to characterize skyrmion magnetic structures.

- In the area of optical spin-orbit states, the follow up experiment is to pass entangled photons through the LOV prism pairs and perform a quantum information protocol. This experiment is currently under way with our colleagues from the University of Waterloo.

- Another application of the optical spin-orbit states is the exploration of its use towards the imaging of chiral biological samples. This research area is currently being explored and a dedicated microscope is being built for this purpose.

Bibliography

[1] D. A. Pushin, *Coherent control of neutron interferometry*. PhD thesis, Massachusetts Institute of Technology, 2006.

[2] J. Nsofini, *Quantum Information Enabled Neutron Interferometry*. PhD thesis, University of Waterloo, 2017.

[3] C. B. Shahi, *Measurement of neutron scattering lengths using neutron interferometry*. PhD thesis, Tulane University School of Science and Engineering, 2016.

[4] C. Shahi, M. Arif, D. Cory, T. Mineeva, J. Nsofini, D. Sarenac, C. Williams, M. Huber, and D. Pushin, "A new polarized neutron interferometry facility at the ncnr," *Nuclear Instruments and Methods in Physics Research Section A: Accelerators, Spectrometers, Detectors and Associated Equipment*, vol. 813, pp. 111–122, 2016.

[5] D. Pushin, M. Huber, M. Arif, C. Shahi, J. Nsofini, C. Wood, D. Sarenac, and D. Cory, "Neutron interferometry at the national institute of standards and technology," *Advances in High Energy Physics*, vol. 2015, 2015.

[6] P. Saggu, T. Mineeva, M. Arif, D. G. Cory, R. Haun, B. Heacock, M. G. Huber, K. Li, J. Nsofini, D. Sarenac, C. B. Shahi, V. Skavysh, W. M. Snow, S. A. Werner, A. R. Young, and D. A. Pushin, "Decoupling of a neutron interferometer from temperature gradients," *Review of Scientific Instruments*, vol. 87, no. 12, p. 123507, 2016.

[7] J. Nsofini, K. Ghofrani, D. Sarenac, D. Cory, and D. Pushin, "Quantum-information approach to dynamical diffraction theory," *Physical Review A*, vol. 94, no. 6, p. 062311, 2016.

[8] J. Nsofini, D. Sarenac, K. Ghofrani, M. G. Huber, M. Arif, D. G. Cory, and D. A. Pushin, "Noise refocusing in a five-blade neutron interferometer," *Journal of Applied Physics*, vol. 122, no. 5, p. 054501, 2017.

[9] B. Heacock, M. Arif, D. G. Cory, T. Gnaeupel-Herold, R. Haun, M. G. Huber, M. E. Jamer, J. Nsofini, D. A. Pushin, D. Sarenac, I. Taminiau, and A. R. Young, "Increased interference fringe visibility from the post-fabrication heat treatment of a perfect crystal silicon neutron interferometer," *Review of Scientific Instruments*, vol. 89, no. 2, p. 023502, 2018.

[10] K. Li, M. Arif, D. G. Cory, R. Haun, B. Heacock, M. G. Huber, J. Nsofini, D. A. Pushin, P. Saggu, D. Sarenac, C. B. Shahi, V. Skavysh, W. Snow, and A. Young, "Neutron limit on the strongly-coupled chameleon field," *Physical Review D*, vol. 93, no. 6, p. 062001, 2016.

[11] B. Heacock, D. Sarenac, M. Arif, M. Huber, D. Hussey, D. Cory, H. Miao, H. Wen, and D. Pushin, "Characterization of neutron diffraction from phase-gratings via momentum projection measurements," *In Preparation*, 2018.

[12] D. A. Pushin, D. Sarenac, D. S. Hussey, H. Miao, M. Arif, D. G. Cory, M. Huber, D. L. Jacobson, J. M. LaManna, J. D. Parker, T. Shinohara, W. Ueno, and H. Wen, "Far-field interference of a neutron white beam and the applications to noninvasive phase-contrast imaging," *Physical Review A*, vol. 95, no. 4, p. 043637, 2017.

[13] D. S. Hussey, H. Miao, G. Yuan, D. Pushin, D. Sarenac, M. G. Huber, D. L. Jacobson, J. M. LaManna, and H. Wen, "Demonstration of a white beam far-field neutron interferometer for spatially resolved small angle neutron scattering," *arXiv preprint arXiv:1606.03054*, 2016.

[14] D. Sarenac, D. Pushin, M. Huber, D. Hussey, H. Miao, M. Arif, D. Cory, A. Cronin, B. Heacock, D. Jacobson, J. . LaManna, and H. Wen, "Three phase-grating moiré neutron interferometer for large interferometer area applications," *Physical Review Letters*, vol. 120, no. 11, p. 113201, 2018.

[15] C. W. Clark, R. Barankov, M. G. Huber, M. Arif, D. G. Cory, and D. A. Pushin, "Controlling neutron orbital angular momentum," *Nature*, vol. 525, no. 7570, pp. 504–506, 2015.

[16] D. Sarenac, M. G. Huber, B. Heacock, M. Arif, C. W. Clark, D. G. Cory, C. B. Shahi, and D. A. Pushin, "Holography with a neutron interferometer," *Optics Express*, vol. 24, no. 20, pp. 22528–22535, 2016.

[17] J. Nsofini, D. Sarenac, C. J. Wood, D. G. Cory, M. Arif, C. W. Clark, M. G. Huber, and D. A. Pushin, "Spin-orbit states of neutron wave packets," *Physical Review A*, vol. 94, no. 1, p. 013605, 2016.

[18] D. Sarenac, J. Nsofini, I. Hincks, M. Arif, C. W. Clark, D. Cory, M. Huber, and D. Pushin, "Methods for preparation and detection of neutron spin-orbit states," *arXiv preprint arXiv:1803.02295*, 2018.

[19] D. Sarenac, D. Cory, J. Nsofini, I. Hincks, P. Miguel, M. Arif, C. Clark, M. Huber, and D. Pushin, "Generation of a lattice of spin-orbit beams via coherent averaging," *arXiv preprint arXiv:1710.03169*, 2017.

[20] M. Planck, "Ueber das gesetz der energieverteilung im normalspectrum," *Annalen der physik*, vol. 309, no. 3, pp. 553–563, 1901.

[21] P. J. Mohr, D. B. Newell, and B. N. Taylor, "Codata recommended values of the fundamental physical constants: 2014," *Rev. Mod. Phys.*, vol. 88, p. 035009, Sep 2016.

[22] A. Einstein, "Über einen die erzeugung und verwandlung des lichtes betreffenden heuristischen gesichtspunkt," *Annalen der physik*, vol. 322, no. 6, pp. 132–148, 1905.

[23] L. De Broglie, *Recherches sur la théorie des quanta*. PhD thesis, Migration-université en cours d'affectation, 1924.

[24] E. Schrödinger, "An undulatory theory of the mechanics of atoms and molecules," *Physical Review*, vol. 28, no. 6, p. 1049, 1926.

[25] M. Born, "Quantenmechanik der stoßvorgänge," *Zeitschrift für Physik A Hadrons and Nuclei*, vol. 38, no. 11, pp. 803–827, 1926.

[26] Č. Brukner and A. Zeilinger, "Diffraction of matter waves in space and in time," *Physical Review A*, vol. 56, no. 5, p. 3804, 1997.

[27] V. F. Sears, *Neutron optics: an introduction to the theory of neutron optical phenomena and their applications*, vol. 3. Oxford University Press, USA, 1989.

[28] R. P. Feynman, R. B. Leighton, and M. Sands, "Lectures on physics, vol. iii," 1965.

[29] M. P. Silverman, *Waves and grains: reflections on light and learning*. Princeton University Press, 1998.

[30] M. S. Mahoney, *The mathematical career of Pierre de Fermat, 1601-1665*. Princeton University Press, 1994.

[31] W. Bothe and H. Becker, "Künstliche erregung von kern-γ-strahlen," *Zeitschrift für Physik A Hadrons and Nuclei*, vol. 66, no. 5, pp. 289–306, 1930.

[32] J. Chadwick, "Possible existence of a neutron," *Nature*, vol. 129, p. 312, 1932.

[33] H. Rauch and S. A. Werner, *Neutron Interferometry: Lessons in Experimental Quantum Mechanics, Wave-Particle Duality, and Entanglement*, vol. 12. Oxford University Press; 2 edition, 2015.

[34] G. L. Greene and P. Geltenbort, "The neutron enigma.," *Scientific American*, vol. 314, no. 4, pp. 36–41, 2016.

[35] O. Hahn and F. Straßmann, "Über den nachweis und das verhalten der bei der bestrahlung des urans mittels neutronen entstehenden erdalkalimetalle," *Naturwissenschaften*, vol. 27, no. 1, pp. 11–15, 1939.

[36] R. Colella, A. W. Overhauser, and S. A. Werner, "Observation of gravitationally induced quantum interference," *Physical Review Letters*, vol. 34, no. 23, p. 1472, 1975.

[37] H. Rauch, A. Zeilinger, G. Badurek, A. Wilfing, W. Bauspiess, and U. Bonse, "Verification of coherent spinor rotation of fermions," *Physics Letters A*, vol. 54, no. 6, pp. 425–427, 1975.

[38] H. Lemmel, P. Brax, A. Ivanov, T. Jenke, G. Pignol, M. Pitschmann, T. Potocar, M. Wellenzohn, M. Zawisky, and H. Abele, "Neutron interferometry constrains dark energy chameleon fields," *Physics Letters B*, vol. 743, pp. 310–314, 2015.

[39] D. A. Pushin, M. Arif, and D. Cory, "Decoherence-free neutron interferometry," *Physical Review A*, vol. 79, no. 5, p. 053635, 2009.

[40] C. J. Wood, M. O. Abutaleb, M. G. Huber, M. Arif, D. G. Cory, and D. A. Pushin, "Quantum correlations in a noisy neutron interferometer," *Physical Review A*, vol. 90, no. 3, p. 032315, 2014.

[41] T. Denkmayr, H. Geppert, S. Sponar, H. Lemmel, A. Matzkin, J. Tollaksen, and Y. Hasegawa, "Observation of a quantum Cheshire Cat in a matter-wave interferometer experiment," *Nat. Commun.*, vol. 5, pp. 1–7, jul 2014.

[42] S. Sponar, J. Klepp, R. Loidl, S. Filipp, G. Badurek, Y. Hasegawa, and H. Rauch, "Coherent energy manipulation in single-neutron interferometry," *Physical Review A*, vol. 78, no. 6, p. 061604, 2008.

[43] L. Koester, H. Rauch, and E. Seymann, "Neutron scattering lengths: a survey of experimental data and methods," *Atomic Data and Nuclear Data Tables*, vol. 49, no. 1, pp. 65–120, 1991.

[44] M. Arif, D. E. Brown, G. L. Greene, R. Clothier, and K. Littrell, "Multistage position-stabilized vibration isolation system for neutron interferometry," *Vibr. Monit. Cont.*, vol. 2264, no. 1, pp. 20–26, 1994.

[45] "Neutron scattering lengths and cross sections." https://www.ncnr.nist.gov/resources/n-lengths/. Accessed: 2018-02-01.

[46] H. Maier-Leibnitz and T. Springer, "Ein Interferometer für langsame Neutronen," *Zeitschrift für Phys.*, vol. 167, pp. 386–402, aug 1962.

[47] H. Rauch, W. Treimer, and U. Bonse, "Test of a single crystal neutron interferometer," *Physics Letters A*, vol. 47, no. 5, pp. 369–371, 1974.

[48] M. Zawisky, J. Springer, R. Farthofer, and U. Kuetgens, "A large-area perfect crystal neutron interferometer optimized for coherent beam-deflection experiments: Preparation and performance," *Nuclear Instruments and Methods in Physics Research Section A: Accelerators, Spectrometers, Detectors and Associated Equipment*, vol. 612, no. 2, pp. 338–344, 2010.

[49] A. I. Ioffe, V. S. Zabiyakin, and G. M. Drabkin, "Test of a diffraction grating neutron interferometer," *Phys. Lett.*, vol. 111, pp. 373–375, jan 1985.

[50] M. Gruber, K. Eder, A. Zeilinger, R. G$'$ahler, and W. Mampe, "A phase-grating interferometer for very cold neutrons," *Physics Letters A*, vol. 140, no. 7, pp. 363 – 367, 1989.

[51] G. van der Zouw, M. Weber, J. Felber, R. Gähler, P. Geltenbort, and A. Zeilinger, "AharonovBohm and gravity experiments with the very-cold-neutron interferometer," *Nucl. Instruments Methods Phys. Res. Sect. A Accel. Spectrometers, Detect. Assoc. Equip.*, vol. 440, pp. 568–574, feb 2000.

[52] U. Schellhorn, R. A. Rupp, S. Breer, and R. P. May, "The first neutron interferometer built of holographic gratings," *Phys. B Condens. Matter*, vol. 234-236, pp. 1068–1070, jun 1997.

[53] J. Klepp, C. Pruner, Y. Tomita, C. Plonka-Spehr, P. Geltenbort, S. Ivanov, G. Manzin, K. H. Andersen, J. Kohlbrecher, M. A. Ellabban, and M. Fally, "Diffraction of slow neutrons by holographic SiO_2 nanoparticle-polymer composite gratings," *Phys. Rev. A*, vol. 84, p. 13621, jul 2011.

[54] J. F. Clauser and S. Li, "Talbot-vonLau atom interferometry with cold slow potassium," *Phys. Rev. A*, vol. 49, pp. R2213–R2216, apr 1994.

[55] F. Pfeiffer, C. Grünzweig, O. Bunk, G. Frei, E. Lehmann, and C. David, "Neutron Phase Imaging and Tomography," *Physical Review Letters*, vol. 96, p. 215505, June 2006.

[56] H. Talbot, "Lxxvi. facts relating to optical science. no. iv," *Philosophical Magazine Series 3*, vol. 9, no. 56, pp. 401–407, 1836.

[57] B. Allman, P. McMahon, K. Nugent, D. Paganin, D. L. Jacobson, M. Arif, and S. Werner, "Imaging: phase radiography with neutrons," *nature*, vol. 408, no. 6809, p. 158, 2000.

[58] S. W. Lee, D. S. Hussey, D. L. Jacobson, C. M. Sim, and M. Arif, "Development of the grating phase neutron interferometer at a monochromatic beam line," *Nuclear Instruments and Methods in Physics Research Section A: Accelerators, Spectrometers, Detectors and Associated Equipment*, vol. 605, no. 1, pp. 16–20, 2009.

[59] M. Strobl, C. Grünzweig, A. Hilger, I. Manke, N. Kardjilov, C. David, and F. Pfeiffer, "Neutron dark-field tomography," *Physical review letters*, vol. 101, no. 12, p. 123902, 2008.

[60] A. D. Cronin and B. McMorran, "Electron interferometry with nanogratings," *Physical Review A*, vol. 74, no. 6, p. 061602, 2006.

[61] C. David, B. Nöhammer, H. Solak, and E. Ziegler, "Differential x-ray phase contrast imaging using a shearing interferometer," *Applied physics letters*, vol. 81, no. 17, pp. 3287–3289, 2002.

[62] A. D. Cronin, J. Schmiedmayer, and D. E. Pritchard, "Optics and interferometry with atoms and molecules," *Rev. Mod. Phys.*, vol. 81, pp. 1051–1129, Jul 2009.

[63] M. S. Chapman, C. R. Ekstrom, T. D. Hammond, J. Schmiedmayer, B. E. Tannian, S. Wehinger, and D. E. Pritchard, "Near-field imaging of atom diffraction gratings: The atomic talbot effect," *Physical Review A*, vol. 51, no. 1, p. R14, 1995.

[64] E. Lau, "Beugungserscheinungen an doppelrastern," *Annalen der Physik*, vol. 437, no. 7-8, pp. 417–423, 1948.

[65] H. Miao, A. Panna, A. A. Gomella, E. E. Bennett, S. Znati, L. Chen, and H. Wen, "A universal moire effect and application in x-ray phase-contrast imaging," *Nature Physics*, 2016.

[66] B. Heacock, M. Arif, R. Haun, M. Huber, D. Pushin, and A. Young, "Neutron interferometer crystallographic imperfections and gravitationally induced quantum interference measurements," *Physical Review A*, vol. 95, no. 1, p. 013840, 2017.

[67] A. Klein and S. Werner, "Neutron optics," *Reports on Progress in Physics*, vol. 46, no. 3, p. 259, 1983.

[68] K. Eder, M. Gruber, A. Zeilinger, R. Gähler, and W. Mampe, "Diffraction of very cold neutrons at phase gratings," *Physica B: Condensed Matter*, vol. 172, no. 3, pp. 329–338, 1991.

[69] M. Dietze, J. Felber, K. Raum, and C. Rausch, "Intensified ccds as position sensitive neutron detectors," *Nucl. Instr. and Meth. A*, vol. 377, pp. 320–324, 1996.

[70] D. Hussey, C. Brocker, J. Cook, D. Jacobson, T. Gentile, W. Chen, E. Baltic, D. Baxter, J. Doskow, and M. Arif, "A new cold neutron imaging instrument at nist," *Physics Procedia*, vol. 69, pp. 48–54, 2015.

[71] T. Shinohara and T. Kai, "Commissioning start of energy-resolved neutron imaging system, raden in j-parc," *Neutron News*, vol. 26, no. 2, pp. 11–14, 2015.

[72] J. Parker, K. Hattori, Fujioka, *et al.*, "Neutron imaging detector based on the μpic micro-pixel chamber," *Nuclear Instruments and Methods in Physics Research Section A: Accelerators, Spectrometers, Detectors and Associated Equipment*, vol. 697, pp. 23–31, 2013.

[73] H. Wen, E. E. Bennett, M. M. Hegedus, and S. C. Carroll, "Spatial harmonic imaging of x-ray scatteringinitial results," *Medical Imaging, IEEE Transactions on*, vol. 27, no. 8, pp. 997–1002, 2008.

[74] J. H. Bruning, D. R. Herriott, J. Gallagher, D. Rosenfeld, A. White, and D. Brangaccio, "Digital wavefront measuring interferometer for testing optical surfaces and lenses," *Applied optics*, vol. 13, no. 11, pp. 2693–2703, 1974.

[75] H. Wen, E. E. Bennett, M. M. Hegedus, and S. C. Carroll, "Spatial harmonic imaging of x-ray scatteringinitial results," *IEEE transactions on medical imaging*, vol. 27, no. 8, pp. 997–1002, 2008.

[76] F. Pfeiffer, M. Bech, O. Bunk, P. Kraft, E. F. Eikenberry, C. Brönnimann, C. Grünzweig, and C. David, "Hard-x-ray dark-field imaging using a grating interferometer," *Nature materials*, vol. 7, no. 2, pp. 134–137, 2008.

[77] S. K. Lynch, V. Pai, J. Auxier, A. F. Stein, E. E. Bennett, C. K. Kemble, X. Xiao, W.-K. Lee, N. Y. Morgan, and H. H. Wen, "Interpretation of dark-field contrast and particle-size selectivity in grating interferometers," *Applied optics*, vol. 50, no. 22, pp. 4310–4319, 2011.

[78] M. Strobl, "General solution for quantitative dark-field contrast imaging with grating interferometers," *Scientific reports*, vol. 4, 2014.

[79] M. Strobl, M. Sales, J. Plomp, W. G. Bouwman, A. S. Tremsin, A. Kaestner, C. Pappas, and K. Habicht, "Quantitative neutron dark-field imaging through spin-echo interferometry," *Scientific reports*, vol. 5, 2015.

[80] A. J. Brooks, G. L. Knapp, J. Yuan, C. G. Lowery, M. Pan, B. E. Cadigan, S. Guo, D. S. Hussey, and L. G. Butler, "Neutron imaging of laser melted ss316 test objects with spatially resolved small angle neutron scattering," *Journal of Imaging*, vol. 3, no. 4, p. 58, 2017.

[81] A. J. Brooks, D. S. Hussey, H. Yao, A. Haghshenas, J. Yuan, J. M. LaManna, D. L. Jacobson, C. G. Lowery, N. Kardjilov, S. Guo, M. M. Khonsari, and L. G. Butler, "Neutron interferometry detection of early crack formation caused by bending fatigue in additively manufactured ss316 dogbones," *Materials & Design*, vol. 140, pp. 420–430, 2018.

[82] J. Cowley and A. Moodie, "Fourier images: I-the point source," *Proceedings of the Physical Society. Section B*, vol. 70, no. 5, p. 486, 1957.

[83] J. Cowley and A. Moodie, "Fourier images iv: the phase grating," *Proceedings of the Physical Society*, vol. 76, no. 3, p. 378, 1960.

[84] V. Bushuev, A. Frank, and G. Kulin, "Dynamic theory of neutron diffraction from a moving grating," *Journal of Experimental and Theoretical Physics*, vol. 122, no. 1, pp. 32–42, 2016.

[85] D. Pushin, D. Cory, M. Arif, D. Jacobson, and M. Huber, "Reciprocal space approaches to neutron imaging," *Applied physics letters*, vol. 90, no. 22, p. 224104, 2007.

[86] S. Werner, H. Kaiser, M. Arif, and R. Clothier, "Neutron interference induced by gravity: new results and interpretations," *Physica B+ C*, vol. 151, no. 1, pp. 22–35, 1988.

[87] V.-O. de Haan, J. Plomp, A. A. van Well, M. T. Rekveldt, Y. H. Hasegawa, R. M. Dalgliesh, and N.-J. Steinke, "Measurement of gravitation-induced quantum interference for neutrons in a spin-echo spectrometer," *Physical Review A*, vol. 89, no. 6, p. 063611, 2014.

[88] G. Biedermann, X. Wu, L. Deslauriers, S. Roy, C. Mahadeswaraswamy, and M. Kasevich, "Testing gravity with cold-atom interferometers," *Physical Review A*, vol. 91, no. 3, p. 033629, 2015.

[89] G. D'Amico, F. Borselli, L. Cacciapuoti, M. Prevedelli, G. Rosi, F. Sorrentino, and G. Tino, "Bragg interferometer for gravity gradient measurements," *Physical Review A*, vol. 93, no. 6, p. 063628, 2016.

[90] V. I. Bazhenov, M. V. Vasnetsov, and M. S. Soskin, "Laser beams with wave front screw dislocations," *Pisma v Zhurnal Eksperimentalnoi i Teoreticheskoi Fiziki*, vol. 52, pp. 1037–1039, Oct. 1990.

[91] L. Allen, M. W. Beijersbergen, R. Spreeuw, and J. Woerdman, "Orbital angular momentum of light and the transformation of laguerre-gaussian laser modes," *Physical Review A*, vol. 45, no. 11, p. 8185, 1992.

[92] J. Harris, V. Grillo, E. Mafakheri, G. C. Gazzadi, S. Frabboni, R. W. Boyd, and E. Karimi, "Structured quantum waves," *Nature Physics*, vol. 11, no. 8, pp. 629–634, 2015.

[93] V. Garces-Chavez, D. McGloin, H. Melville, W. Sibbett, and K. Dholakia, "Simultaneous micromanipulation in multiple planes using a self-reconstructing light beam," *Nature*, vol. 419, no. 6903, pp. 145–147, 2002.

[94] G. Siviloglou, J. Broky, A. Dogariu, and D. Christodoulides, "Observation of accelerating airy beams," *Physical Review Letters*, vol. 99, no. 21, p. 213901, 2007.

[95] S. M. Barnett, M. Babiker, and M. J. Padgett, "Optical orbital angular momentum," *Philosophical Transactions of the Royal Society A*, vol. 375, no. 2087, 2017.

[96] G. Molina-Terriza, J. P. Torres, and L. Torner, "Twisted photons," *Nature Physics*, vol. 3, no. 5, pp. 305–310, 2007.

[97] M. Padgett and R. Bowman, "Tweezers with a twist," *Nature Photonics*, vol. 5, no. 6, pp. 343–348, 2011.

[98] A. Mair, A. Vaziri, G. Weihs, and A. Zeilinger, "Entanglement of the orbital angular momentum states of photons," *Nature*, vol. 412, no. 6844, pp. 313–316, 2001.

[99] J. Wang, J.-Y. Yang, I. M. Fazal, N. Ahmed, Y. Yan, H. Huang, Y. Ren, Y. Yue, S. Dolinar, M. Tur, and A. E. Willner, "Terabit free-space data transmission employing orbital angular momentum multiplexing," *Nature Photonics*, vol. 6, no. 7, pp. 488–496, 2012.

[100] M. F. Andersen, C. Ryu, P. Cladé, V. Natarajan, A. Vaziri, K. Helmerson, and W. D. Phillips, "Quantized Rotation of Atoms from Photons with Orbital Angular Momentum," *Physical Review Letters*, vol. 97, p. 170406, Oct. 2006.

[101] H. He, M. Friese, N. Heckenberg, and H. Rubinsztein-Dunlop, "Direct observation of transfer of angular momentum to absorptive particles from a laser beam with a phase singularity," *Physical Review Letters*, vol. 75, no. 5, p. 826, 1995.

[102] M. Friese, J. Enger, H. Rubinsztein-Dunlop, and N. R. Heckenberg, "Optical angular-momentum transfer to trapped absorbing particles," *Physical Review A*, vol. 54, no. 2, p. 1593, 1996.

[103] W. Brullot, M. K. Vanbel, T. Swusten, and T. Verbiest, "Resolving enantiomers using the optical angular momentum of twisted light," *Science advances*, vol. 2, no. 3, p. e1501349, 2016.

[104] J. Poynting, "The wave motion of a revolving shaft, and a suggestion as to the angular momentum in a beam of circularly polarised light," *Proceedings of the Royal Society of London. Series A, Containing Papers of a Mathematical and Physical Character*, vol. 82, no. 557, pp. 560–567, 1909.

[105] R. A. Beth, "Mechanical detection and measurement of the angular momentum of light," *Physical Review*, vol. 50, no. 2, p. 115, 1936.

[106] P. A. Dirac, "Quantised singularities in the electromagnetic field," in *Proceedings of the Royal Society of London A: Mathematical, Physical and Engineering Sciences*, vol. 133, pp. 60–72, The Royal Society, 1931.

[107] J. Nye and M. Berry, "Dislocations in wave trains," in *Proceedings of the Royal Society of London A: Mathematical, Physical and Engineering Sciences*, vol. 336, pp. 165–190, The Royal Society, 1974.

[108] P. Coullet, L. Gil, and F. Rocca, "Optical vortices," *Optics Communications*, vol. 73, no. 5, pp. 403–408, 1989.

[109] M. Beijersbergen, R. Coerwinkel, M. Kristensen, and J. Woerdman, "Helical-wavefront laser beams produced with a spiral phaseplate," *Optics Communications*, vol. 112, no. 5-6, pp. 321–327, 1994.

[110] M. Uchida and A. Tonomura, "Generation of electron beams carrying orbital angular momentum," *nature*, vol. 464, no. 7289, p. 737, 2010.

[111] B. J. McMorran, A. Agrawal, I. M. Anderson, A. A. Herzing, H. J. Lezec, J. J. McClelland, and J. Unguris, "Electron vortex beams with high quanta of orbital angular momentum," *science*, vol. 331, no. 6014, pp. 192–195, 2011.

[112] D. Petrascheck, "On coherence in crystal optics," *Physica B+ C*, vol. 151, no. 1-2, pp. 171–175, 1988.

[113] D. Pushin, M. Arif, M. Huber, and D. Cory, "Measurements of the vertical coherence length in neutron interferometry," *Physical review letters*, vol. 100, no. 25, p. 250404, 2008.

[114] A. O'neil, I. MacVicar, L. Allen, and M. Padgett, "Intrinsic and extrinsic nature of the orbital angular momentum of a light beam," *Physical review letters*, vol. 88, no. 5, p. 053601, 2002.

[115] K. Y. Bliokh, F. Rodríguez-Fortuño, F. Nori, and A. V. Zayats, "Spin–orbit interactions of light," *Nature Photonics*, vol. 9, no. 12, p. 796, 2015.

[116] M. V. Berry, "Paraxial beams of spinning light," in *International conference on singular optics*, vol. 3487, pp. 6–12, International Society for Optics and Photonics, 1998.

[117] S. Oemrawsingh, E. Eliel, G. Nienhuis, and J. Woerdman, "Intrinsic orbital angular momentum of paraxial beams with off-axis imprinted vortices," *JOSA A*, vol. 21, no. 11, pp. 2089–2096, 2004.

[118] D. Gabor, "A new microscopic principle," *Nature*, vol. 161, no. 4098, pp. 777–778, 1948.

[119] U. Schnars and W. P. Jüptner, "Digital recording and numerical reconstruction of holograms," *Measurement science and technology*, vol. 13, no. 9, p. R85, 2002.

[120] H. Lichte and M. Lehmann, "Electron holographybasics and applications," *Reports on Progress in Physics*, vol. 71, no. 1, p. 016102, 2007.

[121] B. Sur, R. Rogge, R. Hammond, V. Anghel, and J. Katsaras, "Atomic structure holography using thermal neutrons," *Nature*, vol. 414, no. 6863, pp. 525–527, 2001.

[122] L. Cser, G. Török, G. Krexner, I. Sharkov, and B. Faragó, "Holographic imaging of atoms using thermal neutrons," *Physical review letters*, vol. 89, no. 17, p. 175504, 2002.

[123] I. S. Anderson, R. L. McGreevy, and H. Z. Bilheux, "Neutron imaging and applications," *Springer Science+ Business Media*, vol. 200, no. 2209, pp. 987–0, 2009.

[124] E. N. Leith and J. Upatnieks, "Reconstructed wavefronts and communication theory," *JOSA*, vol. 52, no. 10, pp. 1123–1130, 1962.

[125] E. N. Leith and J. Upatnieks, "Wavefront reconstruction with continuous-tone objects," *JOSA*, vol. 53, no. 12, pp. 1377–1381, 1963.

[126] B. Javidi, *Optical and digital techniques for information security*, vol. 1. Springer Science & Business Media, 2006.

[127] S. F. Johnston, *Holograms: a cultural history*. Oxford University Press, 2016.

[128] H. He, N. Heckenberg, and H. Rubinsztein-Dunlop, "Optical particle trapping with higher-order doughnut beams produced using high efficiency computer generated holograms," *Journal of Modern Optics*, vol. 42, no. 1, pp. 217–223, 1995.

[129] A. M. Yao and M. J. Padgett, "Orbital angular momentum: origins, behavior and applications," *Advances in Optics and Photonics*, vol. 3, no. 2, pp. 161–204, 2011.

[130] N. Voloch-Bloch, Y. Lereah, Y. Lilach, A. Gover, and A. Arie, "Generation of electron airy beams," *Nature*, vol. 494, no. 7437, p. 331, 2013.

[131] V. Grillo, E. Karimi, G. C. Gazzadi, S. Frabboni, M. R. Dennis, and R. W. Boyd, "Generation of nondiffracting electron bessel beams," *Physical Review X*, vol. 4, no. 1, p. 011013, 2014.

[132] I. A. Litvin, T. Mhlanga, and A. Forbes, "Digital generation of shape-invariant bessel-like beams," *Optics express*, vol. 23, no. 6, pp. 7312–7319, 2015.

[133] H. Rubinsztein-Dunlop, A. Forbes, M. Berry, M. Dennis, D. L. Andrews, M. Mansuripur, C. Denz, C. Alpmann, P. Banzer, T. Bauer, *et al.*, "Roadmap on structured light," *Journal of Optics*, vol. 19, no. 1, p. 013001, 2016.

[134] C. Maurer, A. Jesacher, S. Fürhapter, S. Bernet, and M. Ritsch-Marte, "Tailoring of arbitrary optical vector beams," *New Journal of Physics*, vol. 9, no. 3, p. 78, 2007.

[135] L. Marrucci, C. Manzo, and D. Paparo, "Optical spin-to-orbital angular momentum conversion in inhomogeneous anisotropic media," *Phys. Rev. Lett.*, vol. 96, p. 163905, Apr 2006.

[136] E. Karimi, L. Marrucci, V. Grillo, and E. Santamato, "Spin-to-orbital angular momentum conversion and spin-polarization filtering in electron beams," *Physical review letters*, vol. 108, no. 4, p. 044801, 2012.

[137] L. Marrucci, E. Karimi, S. Slussarenko, B. Piccirillo, E. Santamato, E. Nagali, and F. Sciarrino, "Spin-to-orbital conversion of the angular momentum of light and its classical and quantum applications," *Journal of Optics*, vol. 13, no. 6, p. 064001, 2011.

[138] G. Milione, M. P. Lavery, H. Huang, Y. Ren, G. Xie, T. A. Nguyen, E. Karimi, L. Marrucci, D. A. Nolan, R. R. Alfano, and A. E. Willner, "4× 20 gbit/s mode division multiplexing over free space using vector modes and a q-plate mode (de) multiplexer," *Optics letters*, vol. 40, no. 9, pp. 1980–1983, 2015.

[139] C. T. Schmiegelow, J. Schulz, H. Kaufmann, T. Ruster, U. G. Poschinger, and F. Schmidt-Kaler, "Transfer of optical orbital angular momentum to a bound electron," *Nature communications*, vol. 7, 2016.

[140] G. Vallone, V. D'Ambrosio, A. Sponselli, S. Slussarenko, L. Marrucci, F. Sciarrino, and P. Villoresi, "Free-space quantum key distribution by rotation-invariant twisted photons," *Phys. Rev. Lett.*, vol. 113, p. 060503, Aug 2014.

[141] Y. Zhang, W. Maas, and D. Cory, "Analysis of homonuclear rf gradient nmr spectroscopy," *Molecular Physics*, vol. 86, no. 3, pp. 347–358, 1995.

[142] D. Cory, J. Miller, A. Garroway, and W. Veeman, "Chemical-shift-resolved back-projection imaging," *Journal of Magnetic Resonance (1969)*, vol. 85, no. 2, pp. 219–227, 1989.

[143] A. Sodickson and D. G. Cory, "A generalized k-space formalism for treating the spatial aspects of a variety of nmr experiments," *Progress in nuclear magnetic resonance spectroscopy*, vol. 33, no. 2, pp. 77–108, 1998.

[144] M. H. Levitt, "Composite pulses," *Progress in Nuclear Magnetic Resonance Spectroscopy*, vol. 18, pp. 61–122, Jan. 1986.

[145] S. Pancharatnam, "Generalized theory of interference, and its applications," in *Proceedings of the Indian Academy of Sciences-Section A*, vol. 44, pp. 247–262, Springer, 1956.

[146] M. V. Berry, "The adiabatic phase and pancharatnam's phase for polarized light," *Journal of Modern Optics*, vol. 34, no. 11, pp. 1401–1407, 1987.

[147] S. Wimperis, "Broadband, Narrowband, and Passband Composite Pulses for Use in Advanced NMR Experiments," *Journal of Magnetic Resonance, Series A*, vol. 109, pp. 221–231, Aug. 1994.

[148] N. B. Smith and A. Webb, *Introduction to medical imaging: physics, engineering and clinical applications*. Cambridge university press, 2010.

[149] P. Kurzynowski, W. A. Wozniak, and E. Fraczek, "Optical vortices generation using the wollaston prism," *Applied optics*, vol. 45, no. 30, pp. 7898–7903, 2006.

[150] P. Kurzynowski, W. Woźniak, and M. Borwińska, "Regular lattices of polarization singularities: their generation and properties," *Journal of Optics*, vol. 12, no. 3, p. 035406, 2010.

[151] D. Pushin, M. Huber, M. Arif, and D. Cory, "Experimental realization of decoherence-free subspace in neutron interferometry," *Physical Review Letters*, vol. 107, no. 15, p. 150401, 2011.

[152] N. Nagaosa and Y. Tokura, "Topological properties and dynamics of magnetic skyrmions," *Nature nanotechnology*, vol. 8, no. 12, pp. 899–911, 2013.

[153] T. Schulz, R. Ritz, A. Bauer, M. Halder, M. Wagner, C. Franz, C. Pfleiderer, K. Everschor, M. Garst, and A. Rosch, "Emergent electrodynamics of skyrmions in a chiral magnet," *Nature Physics*, vol. 8, no. 4, pp. 301–304, 2012.

[154] S. Eckel, J. G. Lee, F. Jendrzejewski, N. Murray, C. W. Clark, C. J. Lobb, W. D. Phillips, M. Edwards, and G. K. Campbell, "Hysteresis in a quantized superfluid 'atomtronic' circuit," *Nature*, vol. 506, no. 7487, pp. 200–203, 2014.

[155] S. Tung, V. Schweikhard, and E. A. Cornell, "Observation of vortex pinning in bose-einstein condensates," *Physical Review Letters*, vol. 97, no. 24, p. 240402, 2006.

[156] A. Afanasev, C. E. Carlson, and A. Mukherjee, "High-multipole excitations of hydrogen-like atoms by twisted photons near a phase singularity," *Journal of Optics*, vol. 18, no. 7, p. 074013, 2016.